# Understanding Failure Mechanisms in Hybrid Fiber Reinforced Laminates through the Combined usage of DIC, AE, Thermography and Optic Based Systems

By

Isa Emami Tabrizi

Submitted to the Graduate School of Engineering and Natural Sciences

in partial fulfillment of

the requirements for the degree of

Doctor of Philosophy

Sabanci University

November 2020

Understanding Failure Mechanisms in Hybrid Fiber Reinforced Laminates through the Combined Usage of DIC, AE, Thermography and Optic Based Systems

APPROVED BY:

………………

………………

………………

………………

………………

………………

DATE OF APPROVAL: 27.11.2020

# Understanding Failure Mechanisms in Hybrid Fiber Reinforced Laminates Through the Combined Usage of DIC, AE, Thermography and Optic Based Systems

Isa Emami Tabrizi

Ph.D. Dissertation, November 2020

Supervisor: Prof. Dr. Mehmet Yildiz

Co-Supervisor: Asst. Prof. Dr. Adnan Kefal

## ABSTRACT

Keywords: Fiber Hybrid Laminates, Structural Health Monitoring, Damage Accumulation, Failure Analysis

Carbon fiber reinforced polymer matrix laminates are widely used in automotive, aerospace and transportation structures due to their light weight, high specific stiffness and strength, and chemical durability. However catastrophic failure of these laminates limits their capability for critical engineering applications. Fiber hybridization is a low cost and effective way to overcome this issue and improve the reliability of Carbon fiber reinforced polymer matrix laminates by introducing *Hybrid Effect*. Nevertheless, failure analysis of hybrid fiber laminates is very difficult task due to presence of multiple constituents inside the laminated structure and spatially heterogenous damage accumulation inside the material. Therefore, this study aims to comprehensively analyze the failure mechanisms and damage development inside glass/carbon fiber hybrid laminates through simultaneous usage of structural health monitoring techniques under various loading conditions in distinct investigation given as three papers.

In the first paper, acoustic emission analysis is used to monitor the damage growth during tensile and flexural tests for hybrid and nonhybrid specimens. The acoustic emission data is clustered by using Kmeans method based on weighted peak frequency and partial power

parameters. Four different clusters are associated with four different failure types namely, Matrix cracking, fiber/matrix interface failure, fiber pull out and fiber breakage for each laminate. An finite element model based on Refined Zigzag Theory (RZT) is utilized to predict the linear behavior of composites and it is shown that onset of major damages recorded by acoustic emission sensors is corresponding to deviation of experimental stress-strain curve from model predictions.

The second paper of this thesis uses full field strain measurements to analyze damage development under in-plane shear condition where glass/carbon fiber hybrid and nonhybrid laminates sequentially show linear and nonlinear response to the applied shear stress. Comparison of strain maps obtained from three-dimensional digital image correlation (DIC) system show the effect of stacking sequence on damage development behavior. Moreover, by selecting appropriate regions of interest for full field strain measurement technique i.e. DIC it is shown that accurate monitoring of shear behavior and failure at V-notch region is possible.

The third part of this investigation shows that differences in tensile stress-strain curves obtained for hybrid and nonhybrid laminates by different strain measurement systems namely, surface mounted strain gauges, digital image correlation and two embedded FBG sensors inside the laminated composite material. The fluctuations in stress-strain curves are well-described using strain and thermal maps obtained by digital image correlation and thermal camera. It is shown that due to the nature of strain measurement techniques, global or local, some failures such as edge splitting might not affect all of strain measurement techniques and therefore cause miscalculation of initial failure point in hybrid laminates, i.e. overestimation of hybrid effect. Furthermore, DIC displacements are smoothed by Smoothing Element Analysis (SEA) and it is demonstrated that using such a mathematical modification can help to remove inherent noise of obtained data from full field measurements at low stress levels. Besides, smoothing analysis has successfully enabled early prediction of failure region in the composite material at stress levels 30% below the strength of laminate. Poisson's ratio evolution monitored through digital image correlation is used for the first time as a damage index and compared with that of biaxial strain gauges for each sample. It is shown that strain gauges indicate faster damage accumulation inside the laminates due to their direct contact with the material under loading condition.

# ÖZET

Anahtar kelimeler: Hibrit Fiber Laminatlar, Yapısal Sağlık İzleme, Hasar Birikimi, Arıza Analizi

Karbon fiber takviyeli polimer matris laminatlar, hafiflikleri, yüksek özgün tokluk ve mukavemetleri ve kimyasal dayanıklılıkları nedeniyle otomotiv, havacılık ve ulaşım yapılarında yaygın olarak kullanılmaktadır. Bununla birlikte, bu laminatların yıkıcı arızası, kritik mühendislik uygulamaları bu laminatların yeterliliğini sınırlar. Fiber hibridizasyonu, bu sorunun üstesinden gelmenin ve Hibrit Etkisi kullanılarak carbon fiber takviyeli polimer matris laminatların güvenilirliğini artırmanın düşük maliyetli ve etkili bir yoludur. Bununla birlikte, laminatlı yapının içinde çok sayıda bileşenin varlığı ve malzeme içinde mekansal olarak heterojen hasar birikimi nedeniyle hibrit fiber laminatların başarısızlık analizi çok zordur. Bu nedenle, üç farklı bölümden oluşan bu çalışma, üç makale olarak verilen farklı incelemede, çeşitli yükleme koşulları altında yapısal sağlık izleme tekniklerinin eşzamanlı kullanımı ile cam /karbon fiber hibrit laminatlar içindeki başarısızlık mekanizmalarını ve hasar gelişimini kapsamlı bir şekilde analiz etmeyi amaçlamaktadır.

Bu tezin ilk kısmında, hibrit ve hibrit olmayan numuneler için çekme ve eğilme testleri sırasında hasar artışını izlemek için akustik emisyon analizi kullanılmıştır. Akustik emisyon verileri, ağırlıklı tepe frekansı ve kısmi güç parametrelerine dayalı Kmeans yöntemi kullanılarak kümelenmiştir. Dört farklı küme, her bir laminat için Matris kırılması, fiber / matris arayüz hatası, fiber çekme ve fiber kırılması olmak üzere dört farklı hata tipiyle ilişkilidir. Kompozitlerin doğrusal davranışını tahmin etmek için Rafine Zigzag Teorisine (RZT) dayalı bir sonlu eleman modeli kullanılıdı ve akustik emisyon sensörleri tarafından kaydedilen büyük hasarların başlangıcının deneysel gerilim-gerinim eğrisinin model tahminlerinden sapmasına karşılık geldiği gösterildi.

Bu tezin ikinci bölümünde, cam/karbon fiber hibrit ve hibrit olmayan laminatların uygulanan kayma gerilimine sırayla doğrusal ve doğrusal olmayan tepki gösterdiği düzlem içi kesme koşulu altında hasar gelişimini analiz etmek için tam alan gerinim ölçümlerini kullanır. Üç boyutlu dijital görüntü korelasyon (DIC) sisteminden elde edilen gerinim haritalarının karşılaştırılması, istifleme dizisinin hasar geliştirme davranışı üzerindeki etkisini

göstermektedir. Ayrıca, tam alan gerinim ölçüm tekniği, yani DIC için uygun ilgi bölgelerinin seçilmesiyle, V-çentik bölgesindeki kayma davranışının ve bozulmanın doğru şekilde izlenmesinin mümkün olduğu gösterilmiştir.

Bu araştırmanın üçüncü bölümü, hibrit ve hibrit olmayan laminatlar için farklı gerinim ölçüm sistemleri, yani yüzeye monte gerinim ölçerleri, dijital görüntü korelasyonu ve lamine kompozit malzeme içine gömülü iki FBG sensörü ile elde edilen çekme gerilme-gerinim eğrilerindeki farklılıkları göstermektedir. Gerilim-gerinim eğrilerindeki dalgalanmalar, dijital görüntü korelasyonu ve termal kamera ile elde edilen gerinim ve termal haritalar kullanılarak iyi tanımlanmıştır. Gerinim ölçüm tekniklerinin doğası gereği, küresel veya yerel, kenar bölme gibi bazı hataların tüm gerinim ölçüm tekniklerini etkilemeyebileceği ve bu nedenle hibrit laminatlarda ilk arıza noktasının yanlış hesaplanmasına, yani hibrit etkisinin fazla tahmin edilmesine neden olduğu gösterilmiştir. Ayrıca, DIC yer değiştirmeleri, Düzleştirme Elemanı Analizi (SEA) ile yumuşatılır ve böyle bir matematiksel modifikasyonun kullanılmasının, düşük gerilim seviyelerinde tam alan ölçümlerinden elde edilen verilerin doğal gürültüsünü gidermeye yardımcı olabileceği gösterilmiştir. Ayrıca, düzeltme analizi laminatın mukavemetinin % 30 altındaki gerilme seviyelerinde kompozit malzemede kırılma bölgesinin erken tahminini başarıyla sağlamıştır. Dijital görüntü korelasyonu ile izlenilmiş Poisson oranının evrimi, ilk kez bir hasar indeksi olarak kullanılmış ve her numune için iki eksenli gerinim ölçerlerinkiyle karşılaştırılmıştır. Gerinim ölçerlerin, yükleme koşulu altındaki malzeme ile doğrudan teması nedeniyle laminatlar içinde daha hızlı hasar birikimine yol açtığı gösterilmiştir.

To my father whose determination is as strong as the mountain,

To my mother whose heart is as vast as the ocean,

To my brother whose courage is as high as the blue sky,

To my sister in-law whose support is as much as a shining sun,

, And to *Golnaz* whose dreams are as deep as life.

# ACKNOWLEDGEMENT

# Contents

# List of Figures

## List of Tables

**Part I**

# Introduction and State of Art

As the requirements for green energy and engineering systems has increased in recent years, the push for light-weight materials with high-strength has multiplied in high tech applications such as aerospace and transportation industries. Carbon fiber reinforced polymer matrix laminates are apt choice for these purposes; however, their specific strength comes at the expense of possible catastrophic failure and complicated damage in structures. Several methods have been introduced to increase failure strain of carbon fiber reinforced laminates and even increase the toughness of these materials [1, 2]. One of the cheapest methods to increase the failure strain of carbon fiber reinforced laminates is utilization of various fibers inside the same matrix system, i.e. fiber hybridization. Employing high elongation (HE) and low elongation (LE) fibers in the same hybrid composite system can help to utilize advantages of all fiber types and diminish/reduce some of their disadvantages[3]. The consequence of fiber hybridization is referred to as the *hybrid effect* which can be defined as the increase in the apparent failure strain ($\varepsilon_f$) of a LE fiber plies (i.e. first drop in stress-strain curve of the hybrid laminate) due to introduction of a high elongation HE fibers. Despite presence of several investigations on the effect of fiber hybridization on mechanical behavior of laminated composites and optimizing the various fiber combinations to achieve higher hybrid effect [4], thorough analysis of the damage accumulation inside these laminates has not been studied yet. Moreover, despite the fact that numerous studies have shown the advantage of using multi-instrument approach in characterization of failure progress inside composite materials [5-11], no simultaneous or single utilization of structural health monitoring techniques for damage characterization of glass/carbon fiber reinforced laminates has been reported yet.

Therefore, in this study the following structural health monitoring systems are used to analyze failure progress under tensile, bending and in-plane shear loading conditions.

(i)     Acoustic Emission (AE): During damage initiation and development inside loaded materials, an acoustic wave emits and propagates throughout the elastic solid medium. These acoustic waves possess specific energy and frequency characteristics which can be distinguished based on the source of failure, its location and material characteristics which the wave propagates through it. Since each acoustic wave (hit) stems from a failure incident in the material, one can monitor the micro-damage evolution inside the materials by

collecting these acoustic emissions[12]. To save these acoustic signals, wide band piezoelectric sensors are attached to the surface of the material to be tested. Since the possible frequency range of damages occurring inside the material are not known, it is logical to use a piezoelectric sensor with flat bandwidth to ensure that a full response is available throughout the frequency range. Time domain of each hit can be transformed into frequency domain after digitization in the acoustic emission data acquisition system, thereby providing several characteristics for acoustic hits in both domains. By selection of two or more of these features for pattern recognition, clustering algorithms are implemented on acquired acoustic emission data, and consequently each hit can be correlated with a specific failure type inside the material. Since several failure types, namely, Matrix Cracking, Delamination/Interface Failure, Fiber Pull Out and Fiber Breakage can occur inside fiber reinforced laminates, usage of acoustic emission analysis and pattern recognition algorithms will ensure efficient damage volution monitoring in glass/carbon fiber reinforced laminates.

(ii) Fiber Bragg Grating (FBG) Sensors: An FBG sensor is a microstructure consisting of a modulated glass fiber core with certain periods of refractive index and polymeric coating material. Presence of periodic gratings at the core of glass fiber results in selective reflection of certain wavelength(s) of continuous transmitted light spectrum. The distance between the periodic gratings can vary due to presence of mechanical or thermal stresses (induced strain) and results in a shift of reflected wavelength from FBG sensor. Moreover, this technology brings about several advantages, namely, multiplexity, electromagnetic immunity, electric isolation, and small size, thus, making them the perfect candidate for monitoring the strain variations by inside the composite structures. Due to their small size these sensors can be easily embedded inside between the plies of laminated composites and provide valuable data from strain variations inside the hybrid material[13].

(iii) Digital Image Correlation (DIC): The basic principle behind DIC technology is implementation of a computer algorithm to follow up patterns of dots in consecutive images taken from the surface of material during deformation and/or movement. The region of interest on the surface of sample is colored with white and black colors to make each pixel identifiable from the surrounding pixels due to presence of a contrast. The images taken by charge coupled device (CCD) cameras during deformation are compared

with reference image taken in undeformed state of material, thereby providing the displacement vector for each point on the surface of material. The engineering strains are readily derived from displacement values, which provides a full field strain maps of the sample. The regions on the surface of material with high strain gradients generally indicate locations susceptible for damage development [10] or regions with sudden variation in material properties as seen in composite materials [14]. Thus, usage of DIC methodology for assessment of strain maps for glass/carbon hybrid fiber laminates provides a comprehensive information about failure progress in these laminates. Moreover, it will help to determine whether full field strain measurement technique gives a different result as compared to local strain measurement methods, thereby providing a different hybrid effect value for hybrid fiber laminates.

(iv)     Infrared Thermography: There are two configurations of thermography used as non-destructive testing and evaluation (NDT & E), namely, active and passive. In active thermography a heat flow is generated and emitted on the surface of material of interest. The variations in thermo-physical properties of sample at certain locations causes differences in flow of heat through the material, thereby indicating the approximate location and size of defects inside the material [15]. On the other hand, in passive thermography the thermal radiation emitted from the surface of material under normal conditions is monitored by a thermal camera[16]. Since damage developments inside the material generate localized temperature fluctuations, therefore images taken by thermal cameras can identify the location, size and probable severity or even type of damage based on the temperature variation[11]. Usage of passive thermography method for monitoring damage evolution under loading conditions for glass/carbon hybrid fiber laminates will provide valuable data about damage types occurring inside these laminates and can have a complementary application besides strain maps obtained from DIC system.

Hypothesize

Selection of appropriate "*Material Allowable*" is a key step in material selection for engineering applications. A design engineer will be ensured that the engineering structure will withstand service loads under environmental conditions only if reliable and conservative characteristics of the material are provided in advance. Despite presence of numerous failure criteria available for prediction of the failure in fiber reinforced polymeric composites, their capabilities is affected significantly by heterogenous damage development and unprecedented statistical factors. As a consequence, certification process in various engineering applications for composite materials is based on experimental tests and analysis. To broaden the certification process for composite materials a detailed understanding of damage accumulation under various loading condition is necessary. Moreover, it seems that measurement uncertainties during mechanical characterization of composite materials can cause ambiguities in proper determination of material allowable. Therefore, presence of a complex failure besides measurement issues can have a synergic effect on reliability of the material. These issues indicate the necessity for a quest about damage evolution inside composite materials and resolving measurement problems related to their characterization. Hence, this research is an attempt to shed a light into these fields and obtain a reliable damage analysis method for laminated materials. It is believed that the information acquired at different stages of this investigation will provide systematic and valuable procedure for appropriate establishment of material allowable in composite structures.

Overview of Part II

Part II of this thesis comprises three papers each corresponding to a chapter where the structural health monitoring systems mentioned earlier are deployed systematically in different stages of this study as follows. In chapter (paper) 1 of this thesis acoustic emission analysis is used under flexural and tensile loading conditions to monitor the overall damage accumulation up to failure point. This analysis is accompanied by FEM model using refined zigzag theory (RZT) in elastic region to verify the deviation point of model from experimental data. The acoustic emission activity is successfully correlated with experimental and numerical results in stress-strain curves for each sample. The acoustic emission data is classified using Kmeans clustering algorithm and various damage types are associated with each cluster of acoustic hits.

In chapter 2, in-plane shear behavior of glass/carbon hybrid fiber laminates is analyzed using DIC system and compared to strain gauge data both in linear and nonlinear response regions of the material. For the first time it has been shown how the size of the region of interest can influence the strain behavior in nonlinear region. Moreover, strain maps obtained by DIC are compared for different laminates at certain strain level and the effect of tacking sequence on observed strain maps is vividly demonstrated.

In chapter 3, simultaneous usage of digital image correlation, thermal camera and embedded FBG sensors is demonstrated. It is shown that strain values obtained from different methods under tensile loading condition start to deviate and thereby demonstrate different failure strains. This variation in failure strain results in different hybrid effect values for hybrid fiber glass/carbon laminates. the reasons behind this strain inconsistencies are successfully determined by comparison of strain and thermal maps obtained through DIC and thermography. It is demonstrated that not all damage developments inside UD laminates influence strain measurement systems and thermal maps can be used as a complementary method to verify this fact. For the first time reduction in Poisson's ratio for fiber reinforced laminates is obtained using DIC strain maps and it is compared with biaxial strain gauge results.

**Part II**

# Paper 1. Experimental and Numerical Investigation on Fracture Behavior of Glass/Carbon Fiber Hybrid Composites Using Acoustic Emission Method and Refined Zigzag Theory

In this study, damage evolution in glass/carbon fiber hybrid composites with various stacking sequences is investigated under pure bending and tensile loading conditions. Based on the experimental tests results, the hybrid effect and ratio is calculated for all laminates. Damage occurrence is recorded using acoustic emission method and then damage types are classified by means of K-means algorithm. Results show four clusters of acoustic data corresponding to four failure types, i.e., matrix cracking, interface failure, fiber pullout, and fiber breakage. Microscopic images together with the results of acoustic emission data point out that the stacking sequence of hybrid composites becomes a dominant factor for hybrid effect in comparison to volume fraction of carbon or glass fibers under flexural loading. Moreover, the presence of glass layers beneath surface carbon layers causes a level off in acoustic emission activity which is associated with a drop and increase in stress of the stress-strain curve of the flexural test. The experimental tests are numerically simulated through finite element method (FEM) based on refined zigzag theory (RZT). Deformation results of RZT-FEM analysis demonstrate the presence of considerable amount of out-of-plane displacements in the hybrid fiber laminates. This important fact is readily captured during the RZT-FEM simulation, which leads to the interlaminar delamination observed in the samples under tensile loading. The RZT-FEM results are also validated against the experimental strain-stress results within the linear-elastic region. Finally, the comparison of experimentally and numerically calculated strain-stress curves shows that the onset of the damage inside the material is demarcated as the deviation of experiment results from numerical ones. Remarkably, at this deviation instant, the acoustic emission activity also initiates for both tensile and bending specimens, hence confirming major damage evolution inside the laminates.

Keywords: Hybrid Structures; Acoustic Emission; Damage Accumulation, Refined Zigzag Theory; Finite Element Method; Laminated Composite Plates.

1.1 Introduction

Fiber reinforced composites (FRPs) are used in various engineering application throughout the world. Specifically, polymer matrix composites are utilized for structural purposes due to their high specific strength and lightweight. Nevertheless, specific strength comes at the expense of possible catastrophic failure and complicated damage in structures. Low fracture toughness of commercially available fiber reinforced polymer matrix composites has always been a challenge for scientists and engineers. This challenge is due to the gradual accumulation of micro-cracks and damages inside FRPs. Thus, preventing crack initiation and growth in FRPs are very important to stop catastrophic failure. Different solutions have been introduced in literature to inhibit the crack growth. An example would be the application of self-healing agents or Nano-materials. In a study by Zanjani et al, multiwalled healing fibers are used to alleviate cracks in micro and nanoscale and in turn restore mechanical capabilities of composites [1]. The main shortcoming of this new method is that it is still in laboratory scale and requires further studies before being applicable at industrial scale since the cost of implementing such methods is rather high with the current technologies. The low fracture toughness of FRPs becomes even more significant when the fiber material itself has high elastic modulus such as carbon fibers. Despite the higher strength of carbon fiber reinforced polymer matrix (CFRP) composites compared to glass fiber reinforced polymer matrix (GFRP) composites, they have very low toughness. A clever way of using this difference is to design composite structures through fiber hybridization. Employing high elongation (HE) and low elongation (LE) fibers in the same hybrid composite system can help to utilize advantages of all fiber types and diminish their disadvantages. The consequence of fiber hybridization is referred to as the *hybrid effect* which can be defined as the increase in the apparent failure strain ($\varepsilon_f$) of a LE fiber plies (i.e. first drop in stress-strain curve of the hybrid laminate) due to introduction of a high elongation HE fibers [17] and can be calculated as Eq. (1):

$$\% \text{Hybrid Effect} = 100 \times \left( \varepsilon_{f-HC} - \varepsilon_{f-LEL} \right) / \varepsilon_{f-LEL} \tag{1}$$

where $\varepsilon_{f-HC}$ is the strain corresponding to the first stress drop in the stress-strain curve of hybrid composite and $\varepsilon_{f-LEL}$ is the ultimate failure strain of low elongation laminate, respectively.

Most common hybrid fiber composites are glass/carbon fiber hybrid composites and extensive research has been conducted to find hybrid effect value for this type of hybrid composites. Below are some case studies and investigations on the hybrid composites under tensile loading. Kretsis, and Swolfs *et al.* in their review papers reported hybrid effect values up to 116 % for carbon/glass fiber hybrid composites subjected to tensile tests [4, 18]. It is known that several factors influence hybrid effect such as failure strain ratio of LE and HE fiber laminates ($\varepsilon_{f-LEL} / \varepsilon_{f-HEL}$), the amount of LE fibers compared to HE ones, the degree of dispersion and the strength distribution of fiber [18-21]. In a recent study, the authors present an analytical model and show that up to 32 % hybrid effect for 10/90 ratio of carbon/glass fibers is achievable if the dispersion is random. Their results demonstrate that significant hybrid effects can be obtained if thinner plies of LE fibers are used in hybrid composites [22]. Petrucci et al. carried out an investigation on tensile behavior of ternary hybrid laminates with basalt fiber core at various configurations. Although the authors didn't mention hybrid effect, hybrid effect of -1% is seen for one of the configurations while the other two configurations showed minor values of 5 % and 1 % for hybrid effect [23]. Despite presence of quite extensive studies about tensile behavior of hybrid composites, the hybrid effect in hybrid composites under the flexural loading conditions has been understudied. This can be related to the absence of a vivid description of hybrid effect under flexural conditions and more complex stress states during bending tests. In a recent work, Dong et al confirmed the existence of hybrid effect under flexural loading condition and their results show that flexural modulus of glass/carbon hybrid composites increases with a change of span-to-depth ratio from 16 to 32 and then stabilizes for further ratio increase. The same investigation has also proposed that hybrid effect becomes more significant if the carbon layers at top surface of bending specimen are replaced with glass plies due to non-linearity of stress distribution during bending tests, however they have been using unsymmetrical configurations [24]. Another study on flexural behavior of hybrid

carbon/glass fiber composites showed that failure strain of hybrid composites was higher if carbon layers were placed at tension side of test coupon since the global failure during flexural loading starts with buckling of upper plies [25]. In a different study, optimal design for flexural behavior of carbon/glass fiber hybrid composites was investigated through introducing a parameter called *hybrid ratio* which is related to total thickness of glass and carbon plies in hybrid laminate and their fiber volume fraction. The results show that maximum hybrid effect occurs when hybrid ratio is 0.125 and volume fraction of fibers for both laminate types is 50%. Yet, the authors use only three levels of fiber volume fraction in this study [12]. To recapitulate, the flexural behavior of hybrid composites is dependent on span to depth ratio, volume fraction of LE fiber in cross section and relative strength of fibers used in specimen and stacking sequence of LE and HE plies. Very little is known for hybrid laminates with symmetrical stacking sequence.

Albeit several published works to find out failure mechanism for hybrid composites under tensile and flexural loading[26, 27], there is no specific study devoted to scrutinizing damage accumulation in hybrid composites. Since HE fibers in hybrid composites increase the strain necessary for global failure [21], determining the types of failures that grow with faster becomes very intriguing to define fiber hybrid composites behavior. Moreover, using an acquisition system that can record damage evolution inside composites other than simple stress and strain would give us valuable data about damage accumulation. Damage initiation and development inside material is accompanied by release of energy emitted as an elastic acoustic wave. Each of these propagating acoustic waves inside material have their specific features associated with the wave source and failure characteristics which enables monitoring the initiation and evolution of damages inside composites[6, 28]. To collect these acoustic signals, referred to as hits, piezoelectric sensors are attached on the surface of the structure. These acoustic hits can be categorized into various groups corresponding to different damage type and failure mechanism. Therefore, pattern recognition algorithms that can distinguish between thousands of hits, cluster data meaningfully and correlate them with various failure modes of materials are desirable. This can help to monitor the remaining useful life of composite materials and improve their structural performance [29]. In fiber reinforced composites, clustering based on frequency of acoustic waves typically leads to three distinct clusters which are in general associated with matrix cracking, matrix-fiber interface failure and fiber breakage [30, 31]. Research by Fotouhi

et al. through acoustic data monitoring of GFRP under mode I delamination test revealed that the dominant frequencies for matrix cracking, debonding, and fiber breakages are between 140-250kHz, 250-350 kHz and 350-450 kHz, respectively [32]. An elaborative study by Gutkin et al. employed peak frequency analysis to cluster damages inside CFRP composites and the results show that matrix cracking, delamination, debonding, fiber failure and fiber pull out possessed peak frequencies at ranges 0-50kHz, 50-150kHz, 200-300kHz, 400-500kHz and 500-600kHz respectively [33].

The improvements in clustering of acoustic data have led to acceptance of K-means algorithm as the regular method of pattern recognition. K-means clustering method based on Euclidean distance between signal data points is accepted as an appropriate method for clustering of the acoustic waves for damage assessment purposes [34]. Kempf et al. used K-means clustering on unidirectional GFRPs and indicated that off axis static loading of more than $20^o$ would change fiber dominated failure to matrix/interphase failure [35]. Cagatay et al. clustered acoustic data gathered during micro damage accumulation in GFRPs through a modified K-means method and revealed that Poisson's ratio decreases notably due to synergic effect of matrix cracking and delaminations [31]. Despite many investigations of acoustic emission assessment in non-hybrid composites, there are very few studies about hybrid fiber composites. Since hybrid composites have various reinforcements, they might reveal new clusters corresponding to failure of these reinforcements and their interface. Saidane et al. used statistical multi variable analysis and showed 4 distinct clusters in hybrid flax/glass fiber composites under tension, corresponding to matrix cracking, interface failure, fiber breakage and delamination between flax and glass plies. They also indicated that interphase weakness would lead to increase of fiber breakages during loading [36]. An investigation by Fotouhi et al. on thin ply UD glass/carbon hybrid laminates under tension showed that the dominant damage mode identified by acoustic emission hits in these composite materials was related to fragmentation in the thin middle carbon ply and delamination between glass/carbon layers. [37].

In addition to acoustic emission, which is a good experimental approach to identify damage evolution in laminated composite structures, the theoretical and/or numerical modeling through finite element method (FEM) is a complementary approach to identify the damage occurrences in composite materials. Since material complexity becomes very important in designing the

fiber hybrid laminates, the stress-strain states must be investigated rigorously within the full-field laminate. Therefore, predicting the in-plane and transverse-shear stress components is vital for avoiding interlaminar failures and full through-the-thickness damages in these laminates [38]. Hence, an efficient and powerful model to perform a comprehensive deformation and stress analysis is necessary. Refined zigzag theory (RZT) is one of these most recent theories developed by Tessler et al. for this purpose [39, 40]. The RZT has a better potential than those offered by the classical zigzag theories in terms of predicting true strain and stress results of laminated beams and plates subjected to general boundary conditions and/or having highly anisotropic material behavior [41-44]. This theory uses the basis of first-order shear deformation theory and introduces piecewise linear zigzag functions having constant derivatives defined by shear coefficients of each ply [39, 40, 45]. These functions have equally zero values at the bounding surfaces of laminate to achieve a physically sensible in-plane displacement and stress fields at these surfaces. Despite discontinuity of transverse-shear stresses at interfaces of each lamina, the RZT transverse-shear stresses calculated from Hooke's law represent true shear stress values in average sense for each lamina. Thus, the true prediction of transverse-shear stresses enables to attain a better structural response of moderately thick structures. The RZT governing equations allow $C^0$-continuous shape functions for the development of various beam- and plate-type finite elements [45-47]. Since the development of the RZT theory, various researchers have investigated wide range of RZT applications to analyze flexural performance of thick laminated structures based analytical models [48-51]. Moreover, various beam, plate, and shell finite element types have been proposed by using RZT and/or in combination with other plate theories [52-57] Moreover, the RZT has been also used successfully to analyze dynamic problems such as modeling damping in a laminated structure [58, 59]. Besides, some studies have conducted experimental validations for RZT under various loading conditions [60, 61]. Furthermore, recent advances in application of RZT included inverse approaches to analyze structural health monitoring of composite structures [62-64]. Herein it is important to note that, although the research regarding RZT application is rising in recent years, there has been no investigation of its application in fiber hybrid laminates.

To the best of authors' knowledge, there is no study on damage evolution and accumulation in glass/carbon fiber hybrid composites under flexural and tensile loading using acoustic emission including RZT as a complementary approach to predicting the damage initiation in

hybrid fiber composites. In this study, acoustic emission with K-means algorithm as well as RZT-FEM analysis are utilized together to assess the damage accumulation during flexural and tensile loading of glass/carbon fiber hybrid composites for the first time in the literature. The proposed novel procedure is as follows. First, the mechanical tests of hybrid composites with different stacking sequences are numerically performed based on the RZT formulation. Then, the mechanical tests are experimentally conducted to validate the linear-elastic response obtained from the RZT analysis. Finally, these results are rigorously compared with those of acoustic emission analysis to successfully predict damage initiation in different hybrid layups. Acoustic emission results show that a new cluster is seen after pattern recognition for tensile specimens which appears only in some of bending specimens. To compare RZT-FEM model predictions with experiments and study the damage evolution in hybrid composites, the number of counts is used as an acoustic emission feature. The count is defined as the number of pulses in an acoustic emission signal or hit that crosses the predefined threshold level. Moreover, microscopic study on damage areas of bending specimens is performed to provide more details about failure types of hybrid composite materials. In the remainder of paper, the experimental procedure and basics of acoustic emission analysis is discussed in Section 3.2. Section 3.3 briefly introduces fundamental equations of the RZT plate theory, its finite element discretization, and modeling details. In Section 3-4, the results of experiments and models are presented and compared in detail. Section 3-5 eventually presents several important conclusions obtained through combined usage of acoustic emission analysis and RZT-FEM modeling in defining the behavior of hybrid fiber laminates.

## 1.2 Experimental Procedure

### 1.2.1   Materials

Unidirectional glass fabrics with areal weight of 330g/cm$^2$ (283 g/m$^2$-1200 Tex along the 0° direction, 37 g/m$^2$-68 Tex E-Glass stitching fibers along the 90° direction and stitch with 10g/m$^2$ -76Dtex) and a tensile elastic modulus of 80GPa is used, which is purchased from Metyx (Turkey) with a trade name of L300 E10B-0. Uniaxial carbon fabrics (from Kordsa Company) with the average areal weight of 300 g/m$^2$ density of 1.78g/cm3 and tensile modulus of 240GPa are used. Araldite LY 564 resin, and Hardener XB 3403 are used for creating matrix material which has a glass transition temperature of 70℃ purchased from Hunstman (USA).

1.2.2    Fabrication of Unidirectional Composite Laminates

All fibers are cut with the size of 60×30 cm and 6 layers of fibers are stacked upon each other in unidirectional configuration [0/0/0]$_s$. The hybrid specimen with configuration of [C/G/G]$_s$ is designated as 1C and [G/C/G]$_s$, [G/G/C]$_s$, [C/G/C]$_s$ configurations are designated as 2C, 3C and 13C respectively for easier reference as seen in Fig. 1-1. The epoxy and hardener are mixed, degassed and impregnated into stacked fabrics through vacuum assisted resin transfer molding (VARTM) method. The curing of impregnated fabrics is performed at 80℃ for 48 hours. Density of each laminate is measured using a home-made system operating on the Archimedes' Principle following the procedure described in ASTM D792 standard. Thermal gravimetric analysis (TGA) is conducted to find the weight fraction of fibers in all specimens using NETZSCH STA 449 C instrument.
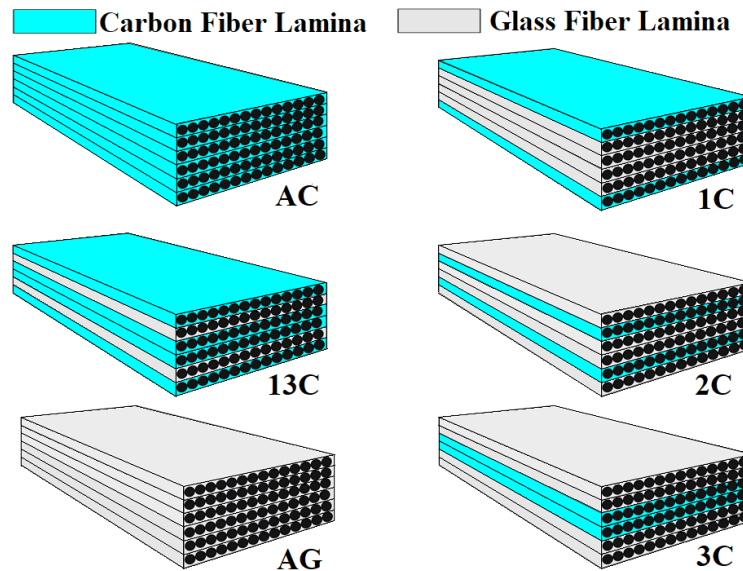


Fig. 1-1. Stacking sequence of produced composite plates and their nomenclature

1.2.3    Mechanical Tests and Through Thickness Micro Analysis

Five tensile samples with the dimensions of 250×20×1.7 mm are cut from manufactured laminates, and the edges of specimens are polished smoothly by 800-grit sand paper to remove any extrusions on peripheral. Aluminum tabs with size of 50×20×1.5 mm are adhered onto the grip locations of tensile specimens using araldite glue in accordance to ASTM D3039. Tests

15

are conducted by 100kN load cell of Instron 5982 universal testing machine. Test speed is set to be 2mm/min and strain values are obtained from a strain gauge attached to the surface of specimen purchased from Vishay PG with gauge factor 2.16±1%. Strain gauges are mounted at the centroid of each sample's top surface, i.e., 75 mm away from edge of the end tabs as seen in Fig. 1-2. Tensile tests continue until global failure of materials based on the mentioned standard. Fiber bundles are also tested by Instron 5982 model universal test machine with the help of special yarn and cord grips. The test speed was set to be 0.5 mm/min. No mechanical data was acquired for these bundle tensile tests since the aim for this setup is to just obtain AE signal of fiber breakages. For bending tests, 5 samples with the size of $80 \times 15$ mm$\times$1.7mm are cut from the manufactured laminates, and then their edges are polished and prepared. The bending tests are performed according to ASTM D790 standard procedure "A". The test speed is also 2mm/min and test end criteria is set to 5000με at outer surface of specimen. The flexural tests are carried out using with same universal testing machine with 10kN load cell.

To analyze the through thickness failure types of the bending specimens, a specific apparatus already used by authors in their previous study is utilized to fix the displacement of failed bending samples [65]. Fixed samples are immersed in a fast curing resin-hardener mixture up to their half width. After curing, the specimens are demolded and dissected to be able to obtain failed region in through thickness direction. Optical micrographs of cut specimen are obtained at through thickness section by Nikon-LV100ND optical microscope. Scanning electron microscope, JEOL JSM 6010, is used to get more detailed images from failure regions. The aim of microscopic investigations is to determine the modes of failure at each ply and correlate them with stress states (i.e., tensile, compression and shear) referring to damage types occurring during flexural test.

### 1.2.4    Acoustic Emission Data Acquisition and Pattern Recognition

To record the acoustic emission (AE) hits throughout the test, Mistras PCI 2 acoustic emission apparatus with AEwin PCI2-4 software is used. Two sensors are connected on the surface of bending and tensile test specimen as shown in the Fig. 1-2. Two 0/2/4 type preamplifiers are used to increase the quality of signals emitted inside the material. The preamplifiers are set to 20dB gain value and single mode input. Pencil lead break test is conducted to make sure that both attached sensors can obtain 100dB signals before the test and

are working properly. Data acquisition parameters based on AE hardware manual are set to 45dB for threshold, 50 $\mu s$ for peak definition time (PDT), 100 $\mu s$ as hit definition time (HDT) and 300 $\mu s$ for hit lockout time (HLT). The sampling rate during data acquisition is 2MHz for each sensor. Necessary features (i.e. Amplitude, Counts, Rise time, etc.) are extracted from recorded hits in time domain simultaneously as the tests proceeded. Acquired AE signals are converted to digital signals. Noesis 7 software is used to get frequency domain of acoustic signals and a *Bessel* band-pass filter (20kHz-800kHz) is applied to remove noise from the dataset [31].

Features of prepared data are imported to MATLAB environment for unsupervised pattern recognition. K-means function is implemented, and silhouette criterion is used to find the optimum number of clusters. This criterion gives a visual understanding of separation distance between clusters. It has a range between [-1 1]. Closer values to unity mean better separation of a cluster from the others and more efficient clustering method. In this study, we have investigated silhouette criterion for various cluster numbers ranging from 2 to 10 clusters and observed that the best division of AE data sets is achieved for four clusters. The parameters used for clustering are weighted peak frequency and partial power 1, lending themselves to well defined clustering results [30, 35, 66]. Weighted Peak frequency is a function of peak frequency and frequency centroid. The peak frequency is obtained after Fast Fourier Transformation of time domain signal and the frequency centroid can be considered as the center of mass for spectral range of recorded AE signal in frequency domain. Partial Powers defines the percentage of signal power located at a predefined frequency ranges of frequency spectral of signal. Table 1-1 shows the method to calculate weighted peak frequency and indicates the partial power frequency ranges.

To be able to distinguish various clusters from one another, first, we have tested bundles of carbon and glass fibers which are carefully separated from dry fabrics and their acoustic data are recorded throughout tensile test. Special yarn and cord grips provided by Instron 5982 universal tensile machine for bundle tests are used to accomplish tests on these fibers. Bundles of 60 cm long are fixed to cord grips while AE sensors are attached to fibers by silicon adhesive. The distance between two sensors is 60 mm located in equidistance position from the center point of the gage length of the bundle.

Table 1-1.  Acoustic Emission Parameters used for clustering

| Feature | Definition |
|---|---|
| Peak Frequency [kHz] | Maximum of frequency spectrum ($f_{peak}$) |
| Weighted Peak Frequency [kHz] | $f_{WPF} = \sqrt{f_{peak} \cdot f_{centroid}}$ |
| Partial Power 1 [%] | 0-200 [kHz] |
| Partial Power 2 [%] | 200-400 [kHz] |
| Partial Power 3 [%] | 400-600 [kHz] |
| Partial Power 4 [%] | 600-800 [kHz] |
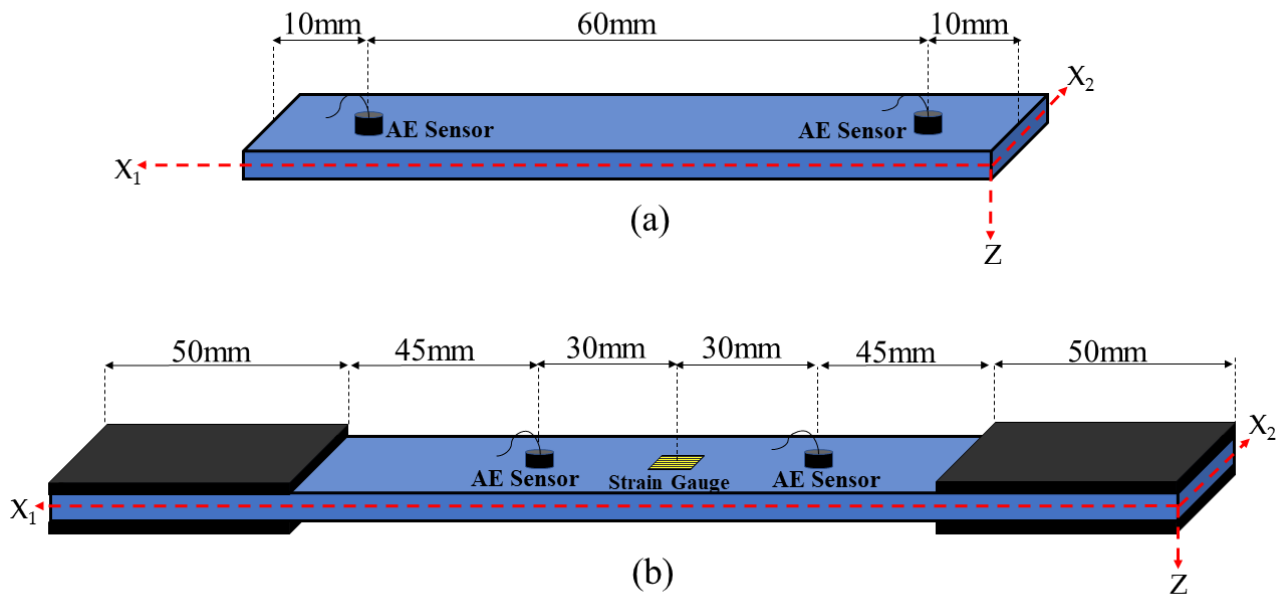


Fig. 1-2. Schematic of (a) Bending and (b) Tensile specimens

## 1.3 Theoretical Basis and Finite Element Modeling

### 1.3.1 Refined Zigzag Theory

Consider a rectangle plate (laminate) with the mid-surface area of $A = a \times b$, where the dimensions $a$ and $b$ are length and width of the plate, respectively. An ORTHOGONAL Cartesian coordinate system $(x_1, x_2, z)$ with the origin $(0,0,0)$ is located on corner of the plate as depicted in Fig. 1-3a Herein, the in-plane coordinates are described by the vector $\mathbf{x} = \{x_1, x_2\}$ with $x_1 \in [0, a]$ and $x_2 \in [0, b]$. The plate has the thickness of $2h$ and the thickness coordinate is defined as $z \in [-h, +h]$ with $z = 0$ defining the reference surface (mid-plane) of the laminate (Fig. 1-3). The plate is subjected to top and bottom normal pressures, $q^+$ and $q^-$, which are aligned with positive and negative $z$-axis, respectively. Note that the plate is assumed to be traction-fee, therefore no edge surface tractions are considered. For clarity, the notation used to describe the geometry and boundary conditions of the plate is clearly shown in Fig. 1-3a. Based on the kinematic relations of the RZT, the displacement field of any material point within the laminate can be expressed as [40]:

$$u_1^{(k)}(\mathbf{x}, z) \equiv u_1^{(k)} = u + z\theta_1 + \phi_1^{(k)} \psi_1 \tag{2a}$$

$$u_2^{(k)}(\mathbf{x}, z) \equiv u_2^{(k)} = v + z\theta_2 + \phi_2^{(k)} \psi_2 \tag{2b}$$

$$u_z(\mathbf{x}, z) \equiv u_z = w \tag{2c}$$

where the symbols $u_1^{(k)}$, $u_2^{(k)}$, and $u_z$ represent the total displacement of the material point along positive $x_1$-, $x_2$-, and $z$-axes, respectively. The $u_z$ displacement is directly represented by the average deflection of the laminate, $w$, i.e., constant through the thickness of the laminate. On the other hand, total displacements $u_i^{(k)} (i = 1, 2)$ model physical in-plane deformation in a layer-by-layer fashion, as they constitute the constant, linear, and zigzag translations of the individual layers. In Eqs. (2a-b), the displacements $u$ and $v$ represent uniform translations, which are constant through the thickness of the laminate, along the

19

positive $x_1$- and $x_2$-axes, respectively (Fig. 1-3a). In addition, the bending rotations $\theta_i$ $(i=1,2)$ are positive and negative counter-clockwise rotations around the positive $x_2$- and $x_1$-axes, respectively (Fig. 1-3a). Their contribution to the total displacement is changing linearly for different $z$ coordinates as expressed in Eqs. (2a-b). Moreover, the rotations $\psi_i$ $(i=1,2)$ are zigzag amplitudes and have the same directions as the bending rotations (Fig. 1-3a). Although these zigzag amplitudes are constant through the thickness, their contribution to the total displacement follow a zigzag pattern as they are multiplied with piecewise-linear zigzag functions of $\phi_i^{(k)}$ $(i=1,2)$ presented in Fig. 1-3b. These zigzag functions change for each individual layer as [39]:

$$\phi_i^{(k)} = z\beta_i^{(k)} + \alpha_i^{(k)} \quad (i=1,2) \tag{3a}$$

$$\beta_i^{(k)} = G_i / Q_{ii}^{(k)} - 1 \quad (i=1,2; \; k=1,2,...,N) \tag{3b}$$

$$\alpha_i^{(k)} = \beta_i^{(k)}h + \sum_{j=2}^{k} 2h^{(j-1)}\left(\frac{G_i}{Q_{ii}^{(k)}} - \frac{G_i}{Q_{ii}^{(j-1)}}\right) \quad (i=1,2) \tag{3c}$$

with

$$G_i = \left(\frac{1}{h}\sum_{j=1}^{N}\frac{h^{(j)}}{Q_{ii}^{(j)}}\right)^{-1} \quad (i=1,2) \tag{3d}$$

where $N$ is the total number of laminae, $\beta_i^{(k)}$ are the layer wise slopes of the zigzag functions, and $\alpha_i^{(k)}$ are the lamina-level constants that satisfy the equilibrium of the piecewise zigzag functions at the interface of the adjacent layers. Inserting the Eq. (3b-d) into Eq. (3a), the original form of the zigzag function, given by Eq. (13c) in the reference [27], can be readily obtained. In Eq. (3d), the symbol $G_i$ denotes the weighted-average transverse-shear stiffness of whole laminate. As introduced by Tessler et al. [40], zigzag functions $\phi_i^{(k)}$ $(i=1,2)$ can be constructed for any laminate using the individual thickness values of the plies, $2h^{(k)}$, and the transformed transverse-shear moduli of each ply, $Q_{ii}^{(k)}$.

(a)



(b)
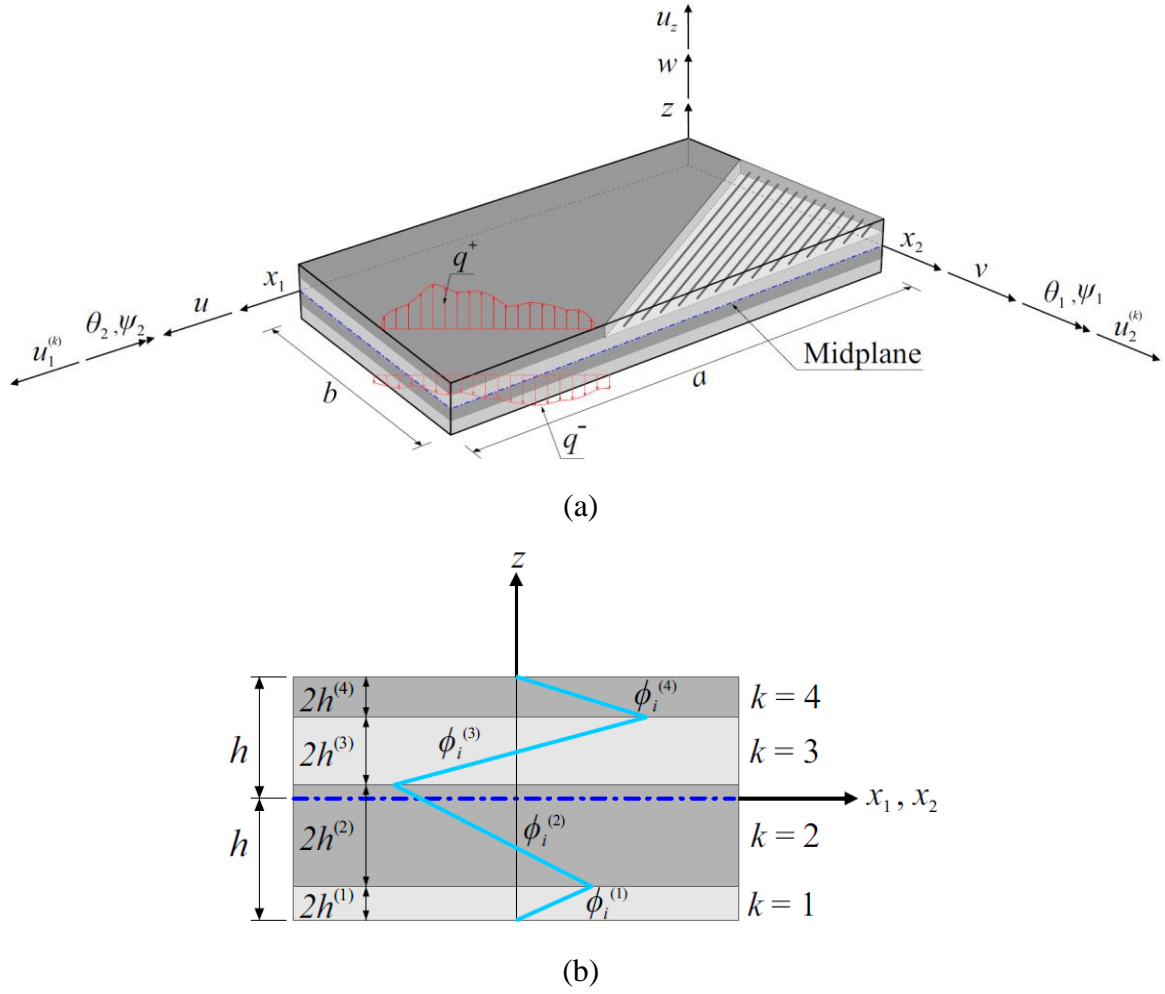
Fig. 1-3. (a) Schematic of geometry and boundary conditions (b) Zigzag functions

After taking the relevant derivatives of the displacement field with respect to the spatial coordinates, the linear in-plane strain field can be expressed as:

$$\boldsymbol{\varepsilon}^{(k)} \equiv \begin{Bmatrix} \varepsilon_{11}^{(k)} \\ \varepsilon_{22}^{(k)} \\ \gamma_{12}^{(k)} \end{Bmatrix} = \begin{Bmatrix} u_{1,1}^{(k)} \\ u_{2,2}^{(k)} \\ u_{1,2}^{(k)} + u_{2,1}^{(k)} \end{Bmatrix} \equiv \mathbf{e} + z\boldsymbol{\kappa} + \mathbf{H}_{\phi}^{(k)}\boldsymbol{\mu} \tag{4a}$$

$$\mathbf{e} = \begin{bmatrix} u_{,1} & v_{,2} & u_{,2} + v_{,1} \end{bmatrix}^T \tag{4b}$$

$$\boldsymbol{\kappa} = \begin{bmatrix} \theta_{1,1} & \theta_{2,2} & \theta_{1,2} + \theta_{2,1} \end{bmatrix}^T \tag{4c}$$

$$\boldsymbol{\mu} = \begin{bmatrix} \psi_{1,1} & \psi_{2,2} & \psi_{1,2} & \psi_{2,1} \end{bmatrix}^T \tag{4d}$$

with

$$\mathbf{H}_\phi^{(k)} = \begin{bmatrix} \phi_1^{(k)} & 0 & 0 & 0 \\ 0 & \phi_2^{(k)} & 0 & 0 \\ 0 & 0 & \phi_1^{(k)} & \phi_2^{(k)} \end{bmatrix} \tag{4e}$$

where the vectors $\mathbf{e}$, $\boldsymbol{\kappa}$, and $\boldsymbol{\mu}$ contain the membrane, bending, and zigzag section strains of the RZT. Besides, the transverse-shear strain field can be expressed by taking first-order derivatives of the relevant displacements as:

$$\boldsymbol{\gamma}^{(k)} = \begin{Bmatrix} \gamma_{1z}^{(k)} \\ \gamma_{2z}^{(k)} \end{Bmatrix} \equiv \begin{Bmatrix} u_{1,z}^{(k)} + u_{z,1} \\ u_{2,z}^{(k)} + u_{z,2} \end{Bmatrix} = \mathbf{H}_\gamma^{(k)} \boldsymbol{\gamma} + \mathbf{H}_\eta^{(k)} \boldsymbol{\eta} \tag{5a}$$

$$\boldsymbol{\gamma} \equiv \begin{bmatrix} \gamma_1 & \gamma_2 \end{bmatrix}^T \equiv \begin{bmatrix} w_{,1} + \theta_1 & w_{,2} + \theta_2 \end{bmatrix}^T \tag{5b}$$

$$\boldsymbol{\eta} \equiv \begin{bmatrix} \gamma_1 - \psi_1 & \gamma_2 - \psi_2 \end{bmatrix}^T \tag{5c}$$

with

$$\mathbf{H}_\gamma^{(k)} = \begin{bmatrix} 1 + \beta_1^{(k)} & 0 \\ 0 & 1 + \beta_2^{(k)} \end{bmatrix}, \quad \mathbf{H}_\eta^{(k)} = \begin{bmatrix} -\beta_1^{(k)} & 0 \\ 0 & -\beta_2^{(k)} \end{bmatrix} \tag{5d}$$

where the vectors $\boldsymbol{\gamma}$ and $\boldsymbol{\eta}$ contain the first and second transverse-shear section strains of RZT. Utilizing the Hooke's law, the stress field of each material point in the laminate can be express as:

$$\begin{bmatrix} \boldsymbol{\sigma}^{(k)} \\ \boldsymbol{\tau}^{(k)} \end{bmatrix} = \begin{bmatrix} \mathbf{C}^{(k)} & \mathbf{0} \\ \mathbf{0} & \mathbf{Q}^{(k)} \end{bmatrix} \begin{bmatrix} \boldsymbol{\varepsilon}^{(k)} \\ \boldsymbol{\gamma}^{(k)} \end{bmatrix} \tag{6a}$$

22

$$\boldsymbol{\sigma}^{(k)} = \left[ \sigma_{11}^{(k)} \quad \sigma_{22}^{(k)} \quad \tau_{12}^{(k)} \right]^T, \ \boldsymbol{\tau}^{(k)} \equiv \left[ \tau_{1z}^{(k)} \quad \tau_{2z}^{(k)} \right]^T \tag{6b}$$

$$\mathbf{C}^{(k)} = \begin{bmatrix} C_{11} & C_{12} & C_{16} \\ C_{12} & C_{22} & C_{26} \\ C_{16} & C_{26} & C_{66} \end{bmatrix}^{(k)}, \ \mathbf{Q}^{(k)} = \begin{bmatrix} Q_{11} & Q_{12} \\ Q_{12} & Q_{22} \end{bmatrix}^{(k)} \tag{6c}$$

where vectors $\boldsymbol{\sigma}^{(k)}$ and $\boldsymbol{\tau}^{(k)}$ are the in-plane and transverse-shear stresses, respectively. The matrices $\mathbf{C}^{(k)}$ and $\mathbf{Q}^{(k)}$ contain the transformed lamina-level orthotropic material properties for either plane strain or plane stress conditions according to the $x_1 x_2$-plane.

Accounting for the variation of internal and external forces within the entire layup, the principle of virtual work can be stated as:

$$\delta W_i - \delta W_e = 0 \tag{7a}$$

$$\delta W_i = \int_V (\delta(\boldsymbol{\varepsilon}^{(k)})^T \boldsymbol{\sigma}^{(k)} + \delta(\boldsymbol{\gamma}^{(k)})^T \boldsymbol{\tau}^{(k)}) dV \tag{7b}$$

$$\delta W_e = \int_A \delta w (q^+ - q^-) dA = \int_A \delta w q_0 dA \tag{7c}$$

where $\delta$ denotes the variation operator, $W_i$ and $W_e$ are energies caused by the internal and external forces acting on the laminate, respectively. Substituting Eq. (4a) and (5a) into Eq. (7) and subsequently integrating individual terms in Eq. (7b) through the thickness of the laminate, the virtual work principle yields to:

$$0 = \int_A (\delta \mathbf{e}^T \mathbf{N} + \delta \boldsymbol{\kappa}^T \mathbf{M} + \delta \boldsymbol{\mu}^T \mathbf{M}^\phi + \delta \boldsymbol{\gamma}^T \mathbf{Q}_z + \delta \boldsymbol{\eta}^T \mathbf{Q}_z^\phi - \delta w q_0) dA \tag{8}$$

where $\mathbf{N}$, $\mathbf{M}$, $\mathbf{M}^\phi$, $\mathbf{Q}_z$, and $\mathbf{Q}_z^\phi$ are the stress resultants, i.e., in-plane forces, bending moments, zigzag moments, first and second transverse-shear forces of the RZT, respectively. These forces and moments can be explicitly stated as [40]:

$$\mathbf{N} \equiv \left[ N_{11} \quad N_{22} \quad N_{12} \right]^T = \int_{-h}^{+h} \boldsymbol{\sigma}^{(k)} dz \tag{9a}$$

23

$$\mathbf{M} \equiv \begin{bmatrix} M_{11} & M_{22} & M_{12} \end{bmatrix}^T = \int_{-h}^{+h} z\boldsymbol{\sigma}^{(k)} dz \qquad (9\text{b})$$

$$\mathbf{M}^{\phi} \equiv \begin{bmatrix} M_{11}^{\phi} & M_{22}^{\phi} & M_{12}^{\phi} & M_{21}^{\phi} \end{bmatrix}^T = \int_{-h}^{+h} (\mathbf{H}_{\phi}^{(k)})^T \boldsymbol{\sigma}^{(k)} dz \qquad (9\text{c})$$

$$\mathbf{Q}_z = \begin{bmatrix} Q_{1z} & Q_{2z} \end{bmatrix}^T = \int_{-h}^{+h} (\mathbf{H}_{\gamma}^{(k)})^T \boldsymbol{\tau}^{(k)} dz \qquad (9\text{d})$$

$$\mathbf{Q}_z^{\phi} = \begin{bmatrix} Q_{1z}^{\phi} & Q_{2z}^{\phi} \end{bmatrix}^T = \int_{-h}^{+h} (\mathbf{H}_{\eta}^{(k)})^T \boldsymbol{\tau}^{(k)} dz \qquad (9\text{e})$$

Expanding the in-plane and transverse-shear stresses in Eq. (9) with the aid of Eq. (6a), the constitutive relations of the RZT can be written in a compact vector-matrix form as:

$$\begin{Bmatrix} \mathbf{N} \\ \mathbf{M} \\ \mathbf{M}^{\phi} \\ \mathbf{Q}_z \\ \mathbf{Q}_z^{\phi} \end{Bmatrix} = \begin{bmatrix} \mathbf{A} & \mathbf{B} & \mathbf{B}_{\phi} & 0 & 0 \\ \mathbf{B}^T & \mathbf{D}_{\kappa} & \mathbf{D}_{\kappa\mu} & 0 & 0 \\ \mathbf{B}_{\phi}^T & \mathbf{D}_{\kappa\mu}^T & \mathbf{D}_{\mu} & 0 & 0 \\ 0 & 0 & 0 & \mathbf{G}_{\gamma} & \mathbf{G}_{\gamma\eta} \\ 0 & 0 & 0 & \mathbf{G}_{\gamma\eta}^T & \mathbf{G}_{\eta} \end{bmatrix} \begin{Bmatrix} \mathbf{e} \\ \boldsymbol{\kappa} \\ \boldsymbol{\mu} \\ \boldsymbol{\gamma} \\ \boldsymbol{\eta} \end{Bmatrix} = \mathbf{D}\boldsymbol{\omega} \qquad (10)$$

with

$$\mathbf{A} = \int_{-h}^{+h} \mathbf{C}^{(k)} dz; \quad \mathbf{B} = \int_{-h}^{+h} z\mathbf{C}^{(k)} dz; \quad \mathbf{B}_{\phi} = \int_{-h}^{+h} \mathbf{C}^{(k)} \mathbf{H}_{\phi}^{(k)} dz; \qquad (11\text{a})$$

$$\mathbf{D}_{\kappa} = \int_{-h}^{+h} z^2 \mathbf{C}^{(k)} dz; \quad \mathbf{D}_{\kappa\mu} = \int_{-h}^{+h} z\mathbf{C}^{(k)} \mathbf{H}_{\phi}^{(k)} dz; \quad \mathbf{D}_{\mu} = \int_{-h}^{+h} (\mathbf{H}_{\phi}^{(k)})^T \mathbf{C} \mathbf{H}_{\phi}^{(k)} dz; \qquad (11\text{b})$$

$$\mathbf{G}_{\gamma} = \int_{-h}^{+h} (\mathbf{H}_{\gamma}^{(k)})^T \mathbf{Q}^{(k)} \mathbf{H}_{\gamma}^{(k)} dz; \quad \mathbf{G}_{\gamma\eta} = \int_{-h}^{+h} (\mathbf{H}_{\gamma}^{(k)})^T \mathbf{Q}^{(k)} \mathbf{H}_{\eta}^{(k)} dz; \quad \mathbf{G}_{\eta} = \int_{-h}^{+h} (\mathbf{H}_{\eta}^{(k)})^T \mathbf{Q}^{(k)} \mathbf{H}_{\eta}^{(k)} dz; \qquad (11\text{c})$$

where the $\mathbf{D}$ is a symmetric matrix that contains the individual stiffness coefficients for different loading directions of the entire layup. Moreover, in Eq. (10), the vector $\boldsymbol{\omega}$ is the conjugate strain measures of the RZT theory. Integrating the principle of virtual work by parts, the Euler-Lagrange equilibrium equations can be obtained for the variation of each translation and rotation term as:

$$\delta u : N_{11,1} + N_{12,2} = 0$$
$$\delta v : N_{12,1} + N_{22,2} = 0$$
$$\delta w : Q_{1z,1} + Q_{2z,2} + q_0 = 0$$
$$\delta \theta_1 : M_{11,1} + M_{12,2} - Q_{1z} = 0 \tag{12}$$
$$\delta \theta_2 : M_{12,1} + M_{22,2} - Q_{2z} = 0$$
$$\delta \psi_1 : M_{11,1}^\phi + M_{11,2}^\phi - Q_{1z}^\phi = 0$$
$$\delta \psi_2 : M_{12,1}^\phi + M_{22,2}^\phi - Q_{2z}^\phi = 0$$

To solve the Eq. (12), the consistent set of kinematic and kinetic boundary conditions can be defined as:

$$\chi = \bar{\chi} \ (\chi = u, v, w, \theta_1, \theta_2, \psi_1, \psi_2) \tag{13a}$$

and

$$\begin{bmatrix} N_{11} & N_{12} \\ N_{12} & N_{22} \\ Q_{1z} & Q_{2z} \end{bmatrix} \begin{Bmatrix} n_1 \\ n_2 \end{Bmatrix} = \begin{Bmatrix} N_{1z} \\ N_{2z} \\ Q_{zn} \end{Bmatrix} \tag{13b}$$

$$\begin{bmatrix} M_{11} & M_{12} \\ M_{12} & M_{22} \\ M_{11}^\phi & M_{12}^\phi \\ M_{21}^\phi & M_{22}^\phi \end{bmatrix} \begin{Bmatrix} n_1 \\ n_2 \end{Bmatrix} = \begin{Bmatrix} M_{1n} \\ M_{2n} \\ M_{1n}^\phi \\ M_{2n}^\phi \end{Bmatrix} \tag{13c}$$

where $\bar{\chi}$ represents the applied displacement and rotation constraints, and the vectors, $[N_{1z} \quad N_{2z} \quad Q_{zn}]^T$ and $[M_{1n} \quad M_{2n} \quad M_{1n}^\phi \quad M_{2n}^\phi]^T$ are the applied forces and moments on the laminate, respectively. Note that the symbols $n_i \ (i = 1,2)$ signify the direction of cosines at the perimeter of the reference surface.

### 1.3.2 Finite element discretization of RZT

The fundamental equations of the RZT theory provided in the previous section can be discretized by following the usual FEM procedures. For this purpose, we use a three-node plate element having seven degrees-of-freedom (DOF) per node developed by Versino et al. [57]. For this plate element, the kinematic variables of RZT are approximated as:

$$
\begin{Bmatrix} u \\ v \\ w \\ \theta_1 \\ \theta_2 \\ \psi_1 \\ \psi_2 \end{Bmatrix} = \begin{bmatrix} \mathbf{N}_1^e & \mathbf{N}_2^e & \mathbf{N}_3^e \end{bmatrix} \begin{Bmatrix} \mathbf{u}_1^e \\ \mathbf{u}_2^e \\ \mathbf{u}_3^e \end{Bmatrix} \equiv \mathbf{N}^e \mathbf{u}^e
$$
(14a)

$$
\mathbf{u}_i^e = \begin{bmatrix} u_i & v_i & w_i & \theta_{1i} & \theta_{2i} & \psi_{1i} & \psi_{2i} \end{bmatrix}^T \quad (i = 1, 2, 3)
$$
(14b)

where $\mathbf{u}^e$ is nodal displacement DOF of the triangular element, and $\mathbf{N}^e$ is the shape function matrix that contains area-parametric coordinates of the triangle and anisoparametric shape functions developed based on the Tessler-Dong constant-shear edge constraints [67]. Substituting Eq. (14a) into Eqs. (4b-d) and (5b-c), the strain measures of the RZT can be defined in terms of $\mathbf{u}^e$ as:

$$
\boldsymbol{\omega} = \begin{bmatrix} \mathbf{B}_1^e & \mathbf{B}_2^e & \mathbf{B}_3^e \end{bmatrix} \begin{Bmatrix} \mathbf{u}_1^e \\ \mathbf{u}_2^e \\ \mathbf{u}_3^e \end{Bmatrix} \equiv \mathbf{B}^e \mathbf{u}^e
$$
(15)

where the matrix $\mathbf{B}^e$ contains the derivate of the shape functions. The explicit forms of $\mathbf{N}^e$ and $\mathbf{B}^e$ matrices can be found in the reference [57]. Rewriting the principle of virtual work and solving it for the variation of $\mathbf{u}^e$, the element equations can be obtained in the following form:

$$
\mathbf{k}^e \mathbf{u}^e = \mathbf{f}^e
$$
(16)

where the stiffness matrix $\mathbf{k}^e$ and force vector $\mathbf{f}^e$ of the element can be calculated as:

$$
\mathbf{k}^e = \int_A (\mathbf{B}^e)^T \mathbf{D} \mathbf{B}^e dA
$$
(17a)

and

$$
\mathbf{f}^e = \int_A (\bar{\mathbf{N}}^e)^T q_0 dA
$$
(17b)

Note that the vector $\bar{\mathbf{N}}^e$ in Eq. (17b) corresponds to the third row of the shape function matrix $\mathbf{N}^e$. Following the conventional FEM assembly procedure, the global system of equation can be obtained as:

$$\mathbf{K}\mathbf{U} = \mathbf{F} \tag{18a}$$

$$X = \overset{nel}{\underset{e=1}{\Omega}} \; \chi^e \quad (X = \mathbf{K}, \mathbf{U}, \mathbf{F}; \; \chi = \mathbf{k}, \mathbf{u}, \mathbf{f}) \tag{18b}$$

where *nel* denotes the total number of triangular element available in the FEM discretization. The Eq. (18a) can be readily solved after prescribing problem-specific boundary conditions.

### 1.3.3 Finite element models of the experiments

The finite element models corresponding to the tensile and bending test specimens, presented in Fig. 1-4, are generated by using high-fidelity discretization. Specifically, for the tensile specimen, the area between the tab surfaces, i.e., gauge length times width ( $a \times b = 150 \times 20 \text{ mm}^2$ ), is discretized using 3000 triangular elements with 11,102 DOF. Similarly, for the bending specimen, the area between the supports, i.e., span times width ( $a \times b = 40 \times 15 \text{ mm}^2$ ), is meshed using 2400 triangular element with 8792 DOF. As shown in Fig. 1-4a and Fig. 1-4b, a cross-diagonal mesh pattern is utilized to generate both meshes. The orthotropic material properties of the carbon-epoxy and glass-epoxy are given in Table 1-2. Young's moduli $E_i^{(k)}$ $(i = 1, 2, 3)$, in-plane shear modulus $G_{12}^{(k)}$, and Poisson's ratio $v_{12}^{(k)}$ of both materials are obtained by performing experimental tests based on the guidelines of ASTM D3039 (tensile test) and ASTM D5379 (v-notched shear test) standards. Moreover, as it is experienced in mechanical behavior of various carbon or glass fibers, the transverse-shear modulus $G_{13}^{(k)}$ and Poisson's ratio $v_{13}^{(k)}$ are assumed to be equal to the corresponding values of $G_{12}^{(k)}$ and $v_{12}^{(k)}$, respectively. Furthermore, the transverse-shear modulus $G_{23}^{(k)}$ and Poisson's ratio $v_{23}^{(k)}$ are calculated based on semi-empirical Halpin-Tsai equations by using elastic properties of the matrix (epoxy) and reinforcement (fibers) materials [68]. The stacking sequences of all six laminates discussed in Section 3.2 are listed in Table 1-3. Note that the lamina thicknesses of each lamina, $2h^{(k)}$, are measured by using a microscope to increase the precision of the RZT-

27

FEM analysis. To simulate the tensile test like in the physical environment for all six laminates, the kinematic boundary conditions along $x_1 = 0$ and $x_1 = 150\,\text{mm}$ are set to $w = 0$. In addition, the symmetry boundary conditions along $x_1 = 75\,\text{mm}$ are

$$u = \theta_1 = \psi_1 = 0 \tag{19a}$$

and along $x_2 = 10\,\text{mm}$ are

$$v = \theta_2 = \psi_2 = 0 \tag{19b}$$

Likewise, the boundary conditions for the bending specimen utilizes the symmetry planes as well as the simply supported edges in the three-point bending experiments. These kinematic boundary conditions along $x_1 = 0$ and $x_1 = 40\,\text{mm}$ (simply supported edges) are

$$w = v = \theta_2 = \psi_2 = 0 \tag{20a}$$

along $x_1 = 20\,\text{mm}$ ($x_2 z$-plane symmetry) are

$$u = \theta_1 = \psi_1 = 0 \tag{20b}$$

and along $x_2 = 7.5\,\text{mm}$ ($x_1 z$-plane symmetry) are

$$v = \theta_2 = \psi_2 = 0 \tag{20c}$$

As depicted in Fig. 1-5a for tensile test case, the uniformly distributed loads of $P_0 = 50$ N/mm along the negative and positive $x_1$-axes are applied at plate edges, $x_1 = 0$ and $x_1 = 150\,\text{mm}$, respectively. Moreover, the uniformly distributed load of $\bar{q}_0 = 10$ N/mm along the negative $z$-axis is applied at mid-span of the plate ($x_1 = 20\,\text{mm}$) for the bending test case (see Fig. 1-5b). To obtain the stress-strain comparisons between the six laminates, without changing the direction of the loads, the magnitude of these loads can be altered for tensile and bending cases.

(a)



(b)
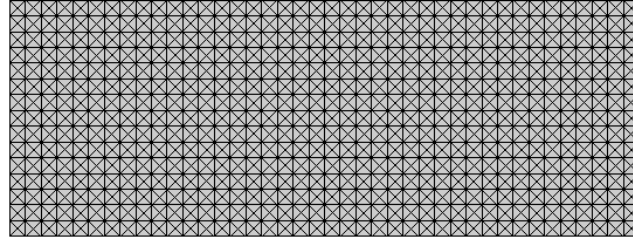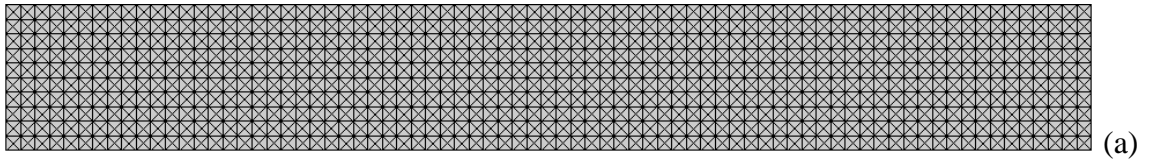
Fig. 1-4. Mesh used for (a) Tensile specimen (b) Bending specimen



$P_0$                                       $P_0$

(a)

$\bar{q}_0$

(b)
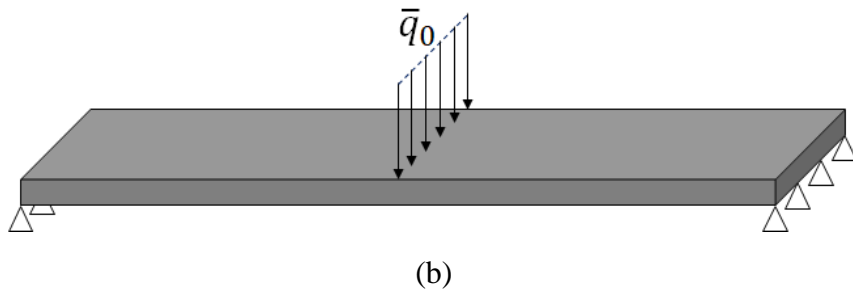
Fig. 1-5. Schematic of load distribution (a) Tensile Specimen (b) Bending specimen

Table 1-2. Mechanical properties of unidirectional carbon epoxy and glass epoxy laminas.

| | Lamina material | Young's modulus [GPa] | Poisson's ratio | Shear modulus [GPa] |
|---|---|---|---|---|
| C | Carbon-epoxy unidirectional composite | $E_1^{(k)} = 137.5$ <br> $E_2^{(k)} = 9.97$ <br> $E_3^{(k)} = 9.97$ | $\upsilon_{12}^{(k)} = 0.27$ <br> $\upsilon_{13}^{(k)} = 0.27$ <br> $\upsilon_{23}^{(k)} = 0.362$ | $G_{12}^{(k)} = 3.57$ <br> $G_{13}^{(k)} = 3.57$ <br> $G_{23}^{(k)} = 3.65$ |
| G | Glass-epoxy unidirectional composite | $E_1^{(k)} = 31.7$ <br> $E_2^{(k)} = 12.54$ <br> $E_3^{(k)} = 12.54$ | $\upsilon_{12}^{(k)} = 0.22$ <br> $\upsilon_{13}^{(k)} = 0.22$ <br> $\upsilon_{23}^{(k)} = 0.26$ | $G_{12}^{(k)} = 3.21$ <br> $G_{13}^{(k)} = 3.21$ <br> $G_{23}^{(k)} = 4.98$ |

Table 1-3. Laminate stacking sequences (lamina sequence is in the positive z-direction).

| Laminate | Lamina thickness, $2h^{(k)}$ [$\mu m$] | Total Thickness, $2h$ [$\mu m$] | Lamina materials | Lamina orientation [$°$] |
|---|---|---|---|---|
| AC | (280/295/292/293/284/293) | 1737 | [C/C/C/C/C/C] | $[0/0/0]_s$ |
| 13C | (300/180/330/332/190/280) | 1612 | [C/G/C/C/G/C] | $[0/0/0]_s$ |
| 1C | (302/305/290/210/290/302) | 1699 | [C/G/G/G/G/C] | $[0/0/0]_s$ |
| 2C | (278/350/225/240/390/210) | 1693 | [G/C/G/G/C/G] | $[0/0/0]_s$ |
| 3C | (234/290/310/280/290/270) | 1674 | [G/G/C/C/G/G] | $[0/0/0]_s$ |
| AG | (280/275/286/290/270/275) | 1676 | [G/G/G/G/G/G] | $[0/0/0]_s$ |

## 1.4 Results and Discussion

### 1.4.1 Effect of Stacking Sequence on Flexural Behavior

All values of flexural stress and flexural strain are calculated according to ASTM D790 standard from maximum load and deflection of center of samples respectively. The value of flexural strength is the maximum stress obtained at maximum load during bending test. Flexural modulus is calculated as chord modulus between 1000με and 3000με in stress-strain curve according to ASTM D790 standard. Since all samples of the same laminates show similar stress-

strain behavior under flexural loading, specimen with an average strength is selected from each composite type and presented in Fig. 1-6a. An apparent trend of reduction in flexural modulus is observed starting from AC laminate to AG as seen in Fig. 1-6b. This is expected since carbon fibers have higher elastic modulus compared to glass fibers. The higher the volume fraction of glass fiber plies, the smaller the flexural modulus of hybrid laminate. This trend can be clearly observed from the stress-strain curve of 13C hybrid specimen since the replacement of glass layers by carbon plies increases flexural modulus. However, the decrease in flexural modulus of 1C, 2C, and 3C specimens with respect to AC is not only related to volume fraction but also associated with the stacking sequences of carbon and glass plies given that the volume fraction of glass fiber for these samples is nearly the same as listed in Table 1-4. These results reveal the importance of stacking sequence in hybrid composites under flexural loading conditions. It is also interesting to note that although 1C, 2C and 3C specimens have somewhat similar strength values, their failure strains are notably different from each other. The percentage of hybrid effect for each laminate is calculated using Eq. 1 given at introduction section and results are presented in Fig. 1-7. Hybrid effects for 13C, 1C, 2C, and 3C laminates are calculated to be about 18%, 21%, 98% and 196%, respectively. This result, particularly considering 1C configuration, indicates that increasing volume fraction of glass fibers will not guarantee to achieve higher hybrid effect under flexural loading conditions. To support this conclusion further, hybrid ratio proposed by Dong et al [69] is calculated to compare degree of hybridization in hybrid composite as given in Eq. (21):

$$r_h = h_g V_{fg} / \left( h_g V_{fg} + h_c V_{fc} \right) \tag{21}$$

in which $h_g$ and $h_c$ in the given order represent the total thickness of glass epoxy and carbon epoxy plies in cured hybrid composite, measured through microscopic examination, $V_{fg}$ and $V_{fc}$ are volume fraction of glass and carbon fibers in hybrid composite laminate. Inferred from Eq. (19), the higher volume fraction of glass fiber, the higher the degree of hybridization is. As seen in Fig. 1-7, hybrid ratio for 1C, 2C and 3C specimen are close to each other but not identical as it should be due to the inherent experimental variation during the manufacturing, while their

31

hybrid effect value is different. Also, the comparison of 13C specimen with 1C laminate reveals that higher level of hybridization does not necessarily ensure greater hybrid effect.

As seen in Fig. 1-6a, non-hybrid laminates, AC and AG laminates, show an abrupt stress drops without any significant sequential step wise decrease in stress. Either compressive stresses at upper half or tensile loads at lower half of specimen result in damage initiation and trigger further failure development. These non-hybrid composites are not able to withstand too much strain after maximum stress and reaches previously stated criteria of failure (5000 $\mu\varepsilon$) in Section 3.2 very soon. Fig. 1-8a presents optical micrographs for upper half of AC laminate. No sign of damage is observed at lower half of specimen indicating that initial drop of stress for this sample is due to compressive failure. Alike AC specimen, Fig. 1-8b shows damage area located only at the upper half of AG specimen. So, buckling is the only evident damage at the top ply of both AC and AG specimens, which indicates that failure development has stopped when reached to the next ply beneath.

The behavior of hybrid composite samples was more complicated. Since the presence of various layers with different stiffness causes more complex failure mechanisms. Because failure either starts from top or bottom plies due to the presence of higher stress states, therein the stiffness of the ply at surface of these hybrid laminates becomes very important. Given that both 13C and 1C configurations have carbon layers at their most outer surfaces, their flexural behavior at initial stages is expected to be similar. To find out whether failure at top or bottom surface is correlated with the first drop at stress in the stress-strain curve, optical micrographs and SEM images of these laminates are analyzed. Fig. 1-8c and Fig. 1-8d show optical and SEM images for failure region of 1C specimen. This laminate shows a kink band formed at the top carbon surface indicated by yellow dashed lines which develops towards lower glass ply as indicated by black dotted lines as shown in Fig. 1-8c. Failure does not advance below specimen midplane as indicated by arrow in Fig. 1-8d, it can be concluded that first drop at the stress in the stress-strain curve is related to buckling of top surface through formation of kink band. So, the further step wise drop at stress for 1C laminate can be related to growth and propagation of kink band damage towards middle layer. As seen in Fig. 1-8e, the same type of failure initiation occurs for 13C specimen as several kink bands at top surface carbon layer indicated by arrows. However, the values of stress for the initiation of failure is higher as shown in Fig. 1-6a. The

reason behind this is the presence of a carbon layer in the middle of laminate which introduces extra stiffness against flexural loads. Failure development into middle plies for 13C specimen is different from kink band growth in the case of 1C laminate such that the kink band already created due to buckling is transformed into the shear driven failure at middle layers as shown by an dashed oval in Fig. 1-8f [70], which can be attributed to the higher stiffness of carbon fibers therein. Otherwise stated, it is obvious that the initiation of failure under flexural loading for hybrid composites is dependent on fiber stiffness, but stress value for failure initiation is related to middle plies stiffness.

As shown in Fig. 1-7. Plot of hybrid effect and hybrid ratio for each bending specimenFig. 1-7, 2C and 3C specimens show higher hybrid effects compared to 13C and 1C composites. Due to the presence of glass plies towards outer surfaces of these laminates, their failure initiation should happen at lower stress and higher strain values. Middle carbon layers of 2C and 3C laminates experience lower tensile and compressive stresses during initial stages of loading due to their closer location with respect to neutral axis of laminate. After complete failure of surface plies, middle carbon layers are subjected to higher strain values, which correspond to maximum stress value at the flexural curve. Thus, no step wise drop at stress in the stress-strain curve is observed. The 3C specimen laminate experiences different failure modes thorough thickness. As shown in Fig. 1-8g kink bands at middle carbon layer are seen while Fig. 1-8h shows that buckling and fiber rupture of glass plies at the top and bottom surfaces happen respectively. Although the stress-strain behavior of 2C and 3C specimens is similar, their failure development is somewhat different. The failure for 2C has not developed through thickness as observed in Fig. 1-8i, which can be associated with the placement of carbon layer sandwiched between less stiff glass layers. As seen in Fig. 1-8i, the failure starts from top glass surface and develops as a shear driven failure indicated by yellow dotted line at the upper carbon ply, resulting in the global failure of laminate. The propagated shear driven failure is transformed into the delamination at interface between glass and carbon layers, which is indicated by an arrow in Fig. 1-8j since the delamination acts as an energy release path for crack growth and developing damage [71]. This observation indicates that interlaminar delamination between glass and carbon laminas is a favorable method of energy release. There is always a competition between kink bands and shear driven failures under flexural loading. The placement of stiffer fibers near neutral axis of bending specimen could result in a higher

hybrid effect without much decrease in strength of material compared to high stiffness non-hybrid laminate, AC. Overall, it can be said that hybrid laminates are very sensitive to stacking sequence and the conventional definition of hybrid effect under flexural loading is not sufficient to predict the behavior of hybrid composites.



(a)                                                      (b)
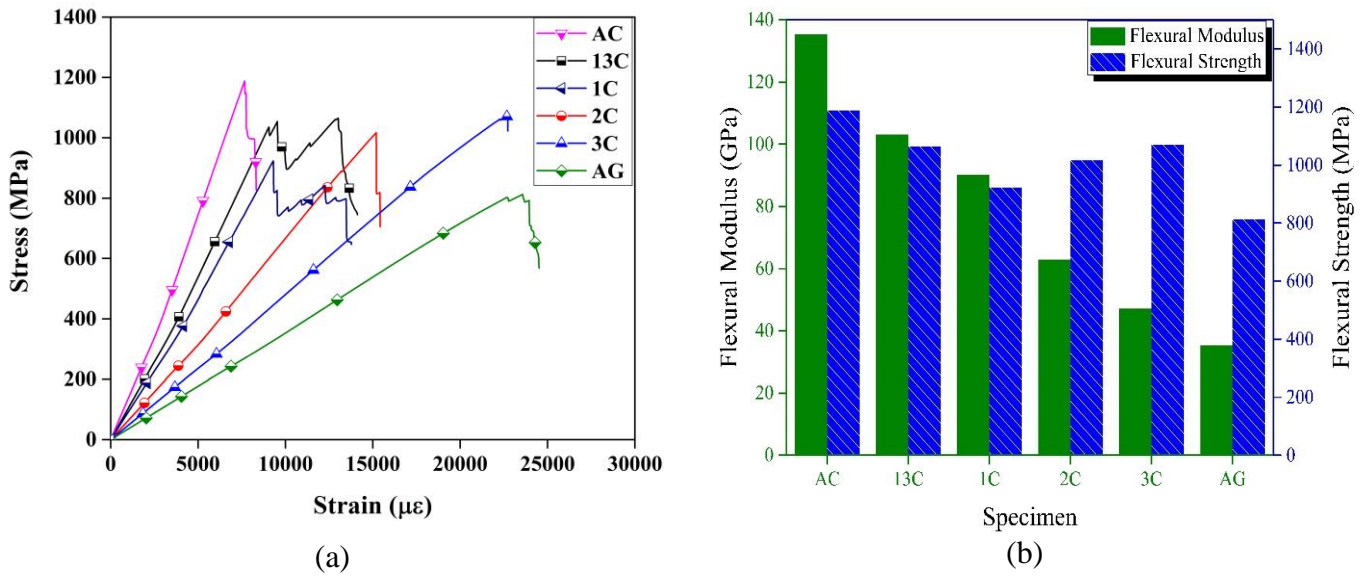
Fig. 1-6. (a) Flexural strain-stress curves (b) Flexural properties chart
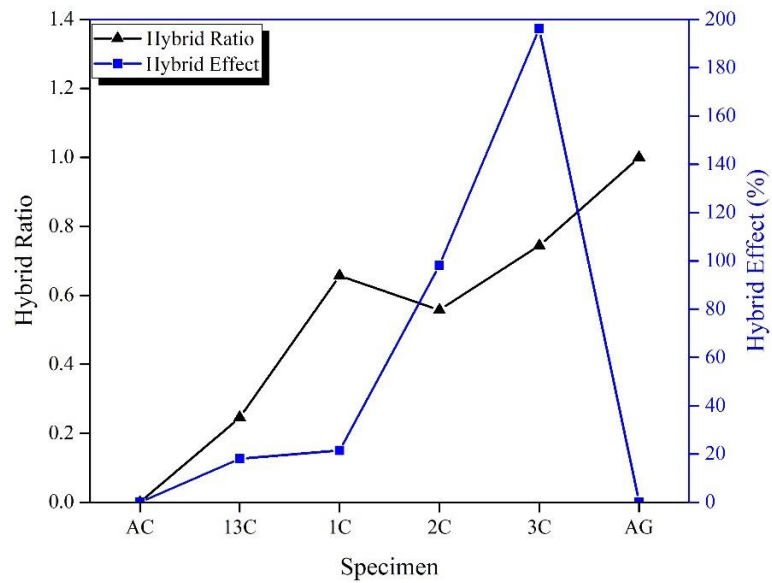


Fig. 1-7. Plot of hybrid effect and hybrid ratio for each bending specimen

Table 1-4. Flexural properties and composite constituent volumes fractions

| Specimen | Flexural Modulus $E_f$ [GPa] | Stress at Break $\sigma_{fB}$[MPa] | Strain at Break $\varepsilon_{fB}$[%] | Volume Fraction of Carbon Fiber ($V_{fC}$) [%] | Volume Fraction of Glass Fiber ($V_{fg}$) [%] | $V_{fg}/V_{fc}$ |
|---|---|---|---|---|---|---|
| AC | 135.5 | 1188.23 | 0.84 | 63 | 0 | 0 |
| 13C | 103.2 | 1065.32 | 0.99 | 42 | 13 | 0.59 |
| 1C | 90.4 | 923.57 | 1.03 | 21 | 25 | 1.19 |
| 2C | 63 | 1016.99 | 1.64 | 23 | 28 | 1.22 |
| 3C | 47.2 | 1071.79 | 2.39 | 22 | 27 | 1.23 |
| AG | 35.3 | 812.44 | 2.46 | 0 | 41 | --- |

(c) 10kV WD12mm SS54 x220 100µm

(d) Carbon Layer / Glass Layer / Carbon Layer — 5kV WD16mm SS54 x23 500µm

(e) Carbon Layer / Glass Layer / Carbon Layer — 200 µm

(f) Shear Driven Failure — Carbon Layer / Glass Layer / Carbon Layer / Glass Layer / Carbon Layer — 10kV WD18mm SS54 x23 500µm

(g) Kink Bands — 200 µm

(h) Buckling / Glass Layer / Carbon Layer / Glass Layer / Fiber Rupture — 10kV WD13mm SS50 x30 500µm
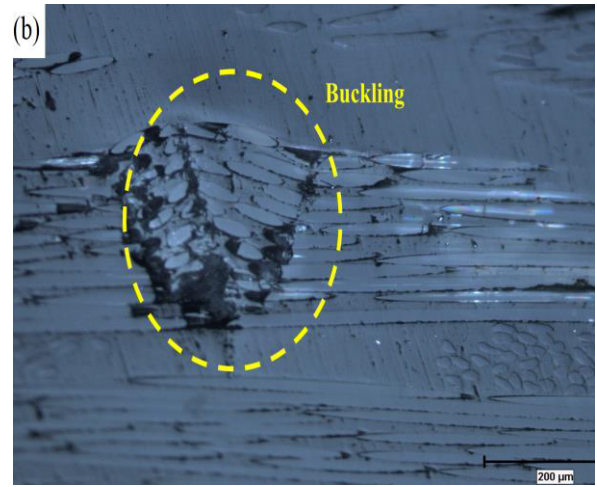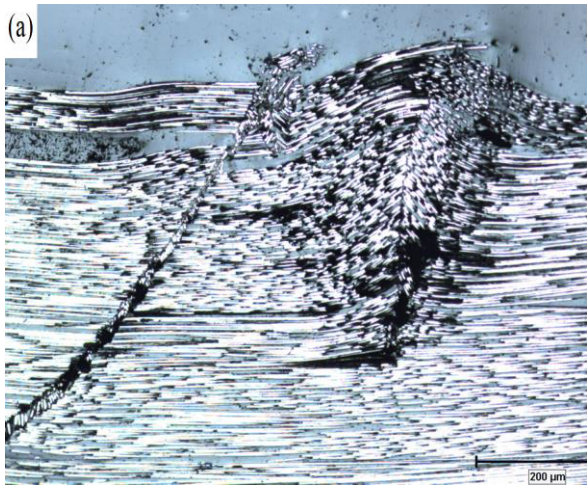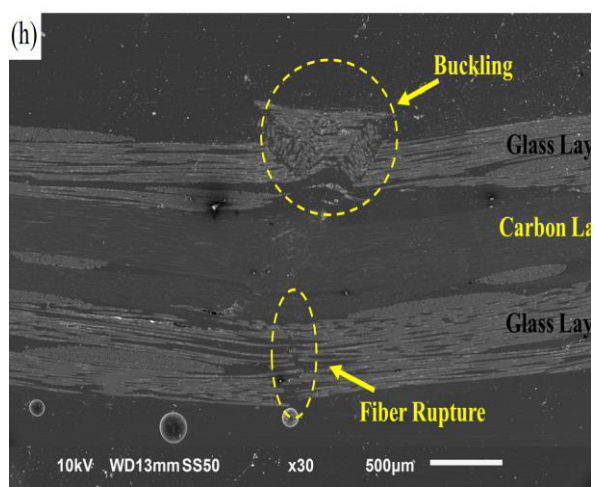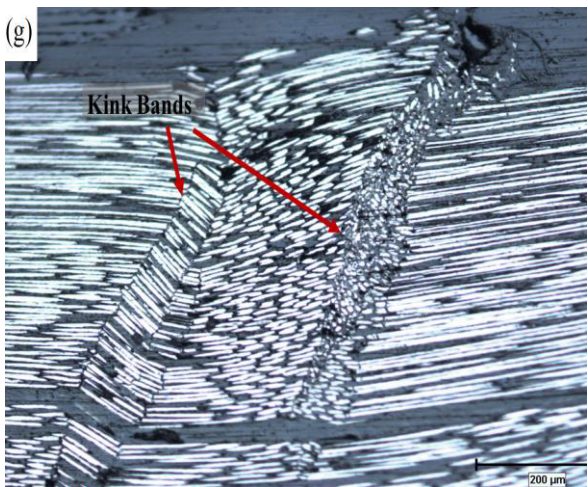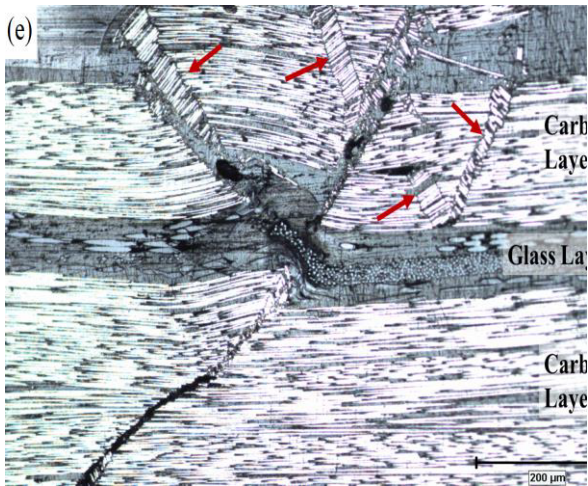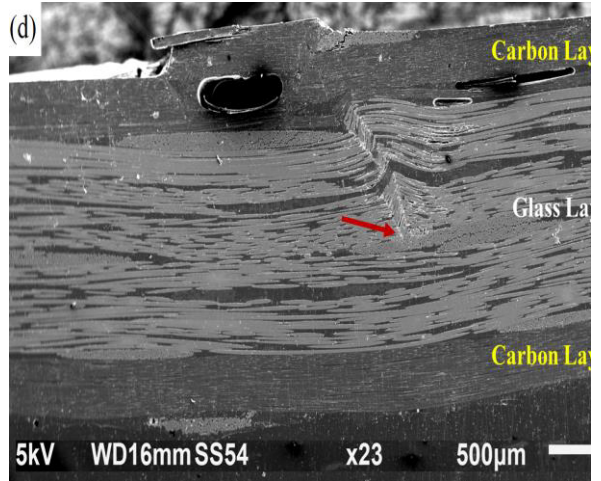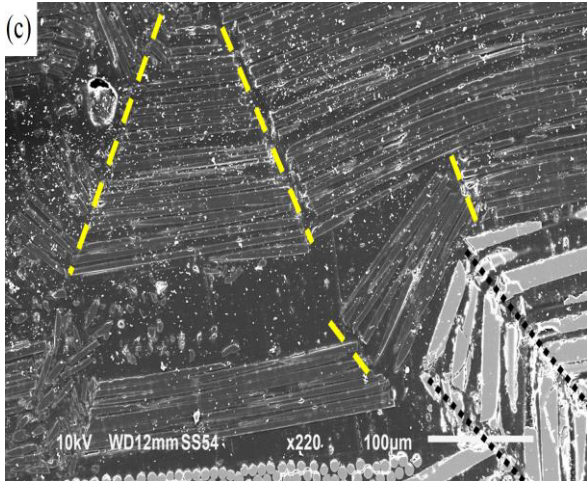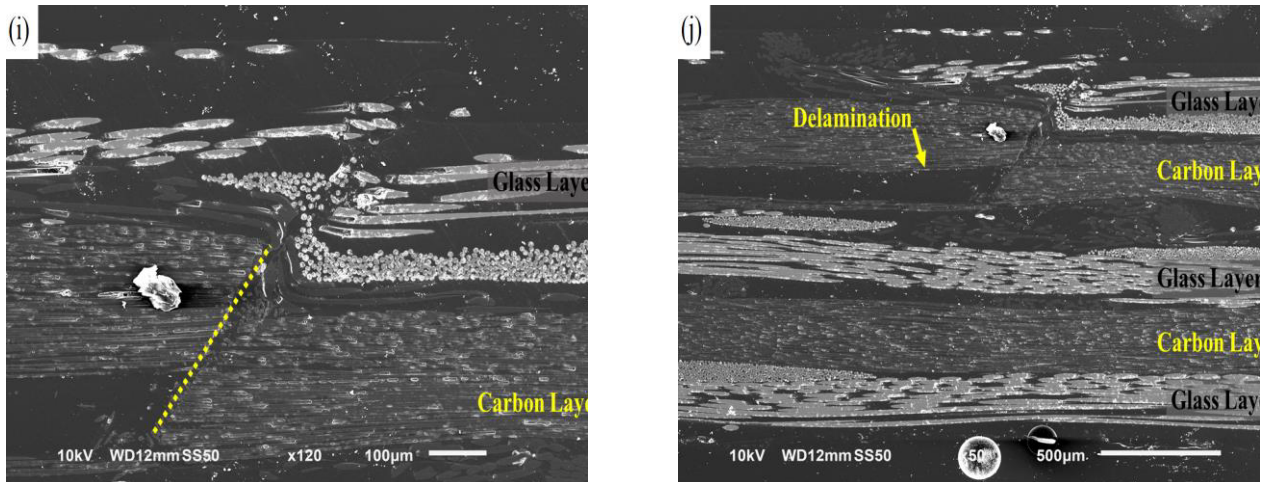
Fig. 1-8. (a) Optical micrograph of failed region for AC specimen, (b) Optical micrograph of failed region for AG specimen, (c) Optical micrograph of 1C showing advance of kink bands from surface carbon layer to glass layers, (d) SEM image of 1C specimen indicating damage development stopped at midplane, (e) Optical micrograph of 13C laminate with several  Kink bands at top layer, (f) SEM image of 13C specimen  showing growth of shear driven failure through middle layers, (g) Optical image of 3C sample with kink bands in middle layers, (h) SEM image for 3C laminate indicate buckling at top surface  and fiber rupture at bottom layers, (i) Shear driven failure of 2C specimen at top carbon ply, (j) Delamination of 2C laminate above middle glass layers

### 1.4.2    Hybrid effect under in plane tensile loading

Given that all samples with the same stacking sequence type demonstrate similar tensile stress-strain behavior, in Fig. 1-9a, only the representative stress-strain curves with average strength are presented for each stacking sequence. Stress values are calculated through division of force value (i.e., obtained from the load cell with a predefined sampling rate, 10 Hz) by initial cross section area of samples while strain values are obtained through strain gauge data at each stress level. This Figure plainly shows the trend of the tensile properties from AC laminate to AG laminate. It is clear to note that as the glass fiber content of a specimen increases, its modulus decreases and strain at failure increases accordingly. This trend is expected since glass fiber plies have lower strength value with more ductility compared to carbon fiber laminas. Values of chord modulus and tensile strength are calculated according to ASTM D3039 standard. The AC sample yields the highest chord modulus as seen in Fig. 1-9b while the AG laminate demonstrates the lowest chord modulus. Hybrid specimens follow the elasticity reduction trend mentioned above but exhibit different behavior when compared to flexural

loading conditions. As seen in Fig. 1-9b, the first difference is that unlike their flexural stress strain behavior, 1C, 2C and 3C hybrid specimens indicate similar elasticity and strength. They even show similar strain at failure as can be seen from Fig. 1-9a. These results reveal that for unidirectional fiber hybrid laminates, volume fraction of carbon and glass fibers is the determinant factor for the overall tensile behavior. However, if these laminates were stacked asymmetrically, extensional-bending coupling matrix would have nonzero values, leading to complex stress fields as in the case of flexural loading and the volume fraction of LE and HE plies would be a less important factor. As seen in Fig. 1-10, hybrid effect values for 1C, 2C and 3C hybrid composites decreases in the range of 65 to 45 percent respectively and their hybrid ratio does not present the same reduction pattern, clearly implying that higher hybrid ratio does not necessarily avail higher hybrid effect.

Another important point obtained from Fig. 1-10 is high hybrid effect for 13C laminate, which is almost equal to that for 2C sample. Previously stated, the volume content of glass and carbon fiber laminas are the critical factors for stress-strain behavior under tensile loading. Despite its lower glass fiber content, 13C specimen has similar strain at failure as the other hybrid composites. To answer to this unintuitive observation, stress at failure for 13C specimen should also be considered. As seen in Fig. 1-9b, this laminate shows higher strength compared to AC sample, which is not expected. Since all experimental conditions are controlled and fixed, Laminate's inherent properties are likely to cause this difference. Zanjani et al. have mentioned in their research that difference of thermal expansion coefficient between carbon and glass laminas can be very important to induce residual stresses during manufacturing steps of hybrid laminates [72]. During cooling period of cured 13C laminate, higher thermal expansion coefficient of glass fibers compared to carbon fibers put glass and carbon fiber plies under tension and compression, respectively. Since the volume fraction of carbon layers is more than glass plies, overall residual stress for 13C sample is of a compressive nature. Thus, the tensile strength of this laminate is higher compared to AC non-hybrid specimen. 1C, 2C and 3C laminates present inverse behavior to 13C sample such that overall residual thermal stress is in tension due to higher volume faction of glass plies compared to carbon layers. Hence, their strength is akin to AG specimen despite similar hybrid effect levels as 13C laminate.

Since carbon plies have lower ductility than glass layers, they fail at lower strain level and typical fiber hybrid composites might show a step-wise drop and increase in stress strain behavior during tensile loading. A stress drop will accompany this primary failure and load will be transferred to glass plies if the stress level drops down below glass laminates ultimate strength. In this case, failure of glass layers would define global breakage of hybrid laminate [4]. Otherwise, global failure of the laminate occurs due to the breakage of carbon layers. None of the hybrid laminates in this study shows stepwise failure as presented in Fig. 1-9a, which can be attributed to two possible reasons, namely, the absence of load transfer and/or stress intensification due to breakage of carbon layers. A study accomplished by Czél et al. has also showed similar results [73]. In another investigation by Czél et al., they have mentioned that this abrupt failure of ply by ply hybrid composites is in direct relationship with energy release through mode II failure of laminate after failure of LE plies [74]. So, the absence of load transfer in our case is probably due to disability of matrix/glass fiber interface to transfer load onto glass fibers, which can also be attributed to ductile and low $T_g$ matrix material used. Moreover, as will be illustrated in RZT-FEM results, after the breakage of carbon layers, the shear stress between glass fibers and matrix result in fast propagation of delamination at glass fiber/matrix interface. Since glass fibers are subjected to extreme loading beyond their strength, they do not carry load and experience abrupt failure immediately after the breakage of carbon plies. Fig. 1-11shows the presence of severe delamination between the interface of glass and carbon layers for 2C specimen, which can be given as an evidence for stress intensification at interlaminar interface and fast energy release path. According to Hedgepeth et al., during failure of a fiber in composites, a dynamic stress is introduced to the laminate, which can cause stress concentrations up to 1.27 times the nominal stress [75]. In the current study, similar dynamic stresses owing to the breakage of carbon fibers could intensify the stress level transferred to glass plies and add up to transverse shear stresses such that its value exceeds the ultimate strength of glass plies. Consequently, glass plies cannot carry this level of stress and fail immediately after interlaminar delamination.

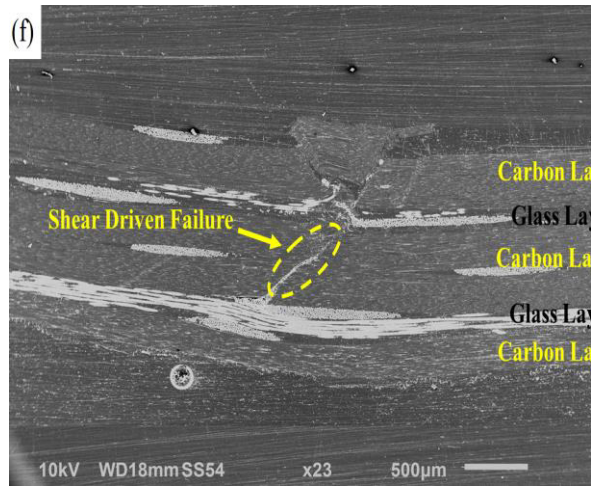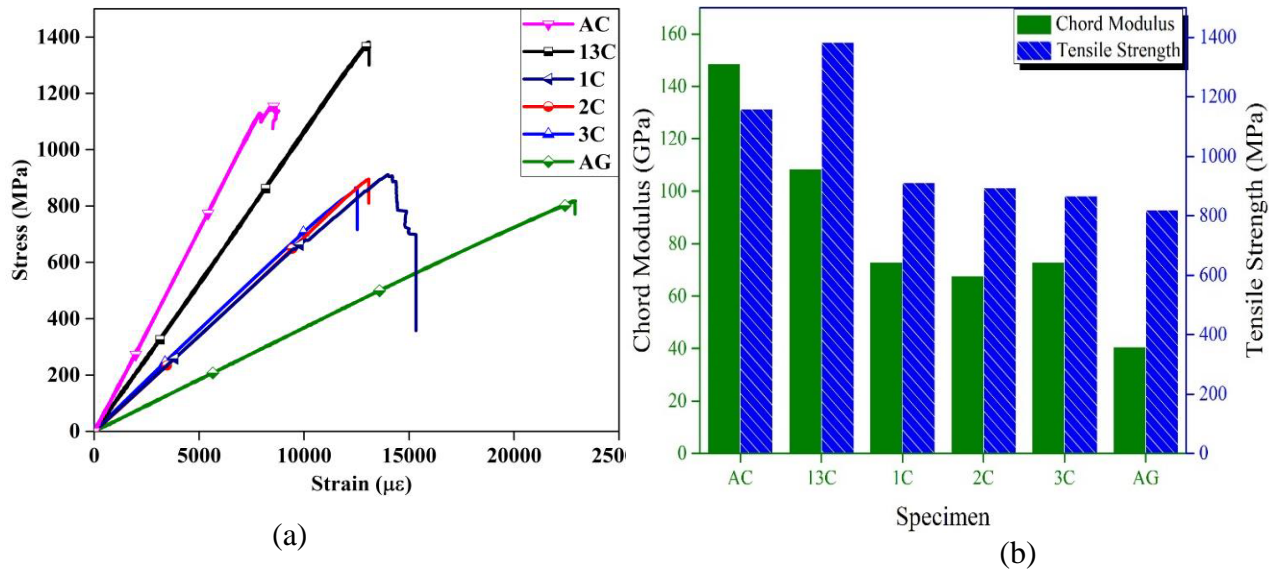Fig. 1-9. (a) Tensile stress- strain curve of each laminates (b) strength and modulus of respective laminates
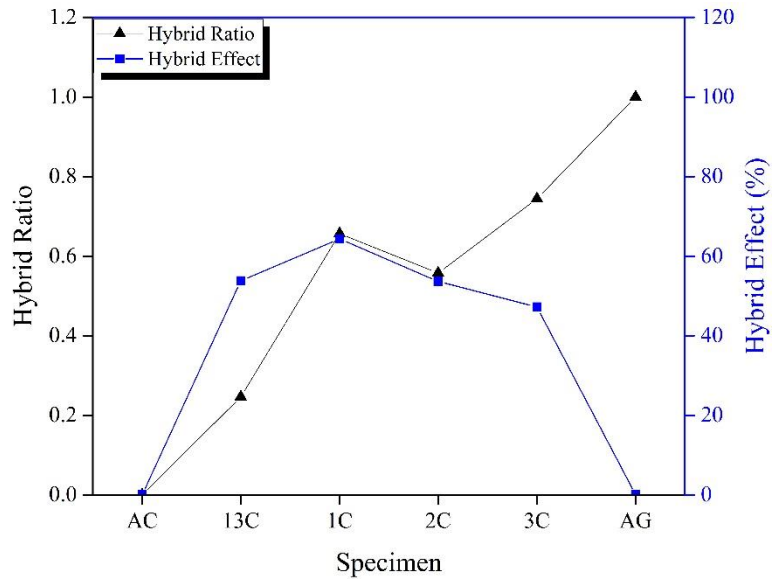


Fig. 1-10. Plot of Hybrid effect and hybrid ratio for each tensile specimen
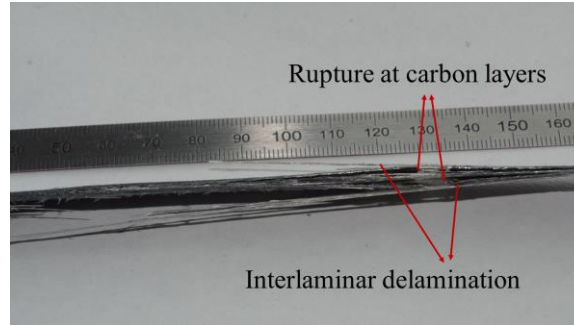
Fig. 1-11. Failure region of 2C specimen indicating fiber rupture in carbon plies and delamination of glass layers

### 1.4.3 FEM results

In this section, we will present the deformation, strain, and stress results of RZT-FEM model presented in Section 3.3 for both tensile and bending tests and compare these numerical results with their experimental counterparts given in the Sections 3.4.1 and 3.4.2. However, before presenting these results, it is worth to structurally classify each specific lamination stacking sequence investigated in this study. This classification can be made through comparing the zigzag function variations of laminate configurations. As a result, a relative analogy between these laminates and three different layups, i.e., (1) a single-layer lamina, (2) a five-layer hybrid laminate, and (3) a three-layer sandwich-like laminate, can be established. The laminates 2C and 3C have glass fiber laminae in the external (top and bottom) layers, whereas carbon fiber laminae are located internally such that the carbon fibers are embedded between the bounding glass fibers. This particular layup configurations give rise to the so-called *"externally weak layers"* problem originally investigated by Gherlone [76]. Therefore, the zigzag functions corresponding to the external weak layers require a correction for complying with the actual physical behavior of 2C and 3C laminates. Since the external glass fibers has a smaller transverse-shear modulus than those of internal carbon fibers (e.g., 2C laminate has $G_{13}^{(1)} \leq G_{13}^{(2)}$ and $G_{13}^{(6)} \leq G_{13}^{(5)}$), the external glass laminae should be driven by the internal carbon layers. As a consequence, during bending in $x_1 z$-plane, the axial displacement at the interface between the external-glass and internal-carbon laminae will be continues without any drastic slope change. Equating the external weak layers transverse-shear moduli to the internal stiff ones will make a correction to the zigzag function, which will represent the expected physical behavior.

For example, the correction of $G_{13}^{(1)} = G_{13}^{(2)}$ and $G_{13}^{(6)} = G_{13}^{(5)}$ should be applied to 2C laminate to obtain a realistic zigzag function.

The zigzag functions corresponding to the AC and AG laminate vanish as at every interface of the laminate, as they are made of a single material along the thickness coordinate. Hence, both these laminates can be analogically referred to as a single-layer lamina. Moreover, once the corrections of externally weak layer are made for the 3C specimen, the whole layup will have the same transverse-shear modulus of carbon fibers, hence the 3C specimen can be also classified as a single-layer lamina (having hybrid effects). On the other hand, the zigzag function for the laminate configuration of 13C is plotted versus the thickness coordinate in Fig. 1-12a. This figure illustrates that the 13C laminate behaves like a five-layer hybrid laminate since the slope of the zigzag function alters dramatically only five times as depicted in Fig. 1-12a. The variation of zigzag functions for the 1C and 2C laminates are plotted in Fig. 1-12b, where the zigzag functions has mainly three different piecewise linear form in different thickness ranges. Hence, the 1C and 2C laminates can be considered as sandwich-like laminate made of three different laminae. In particular, the 1C laminate behaves like a three-layer laminate with a thick core and thin face sheets, whereas the 2C laminate is a three-layer sandwich having thicker face sheets and thinner core as compared to the 1C specimen.



(a)

(b)
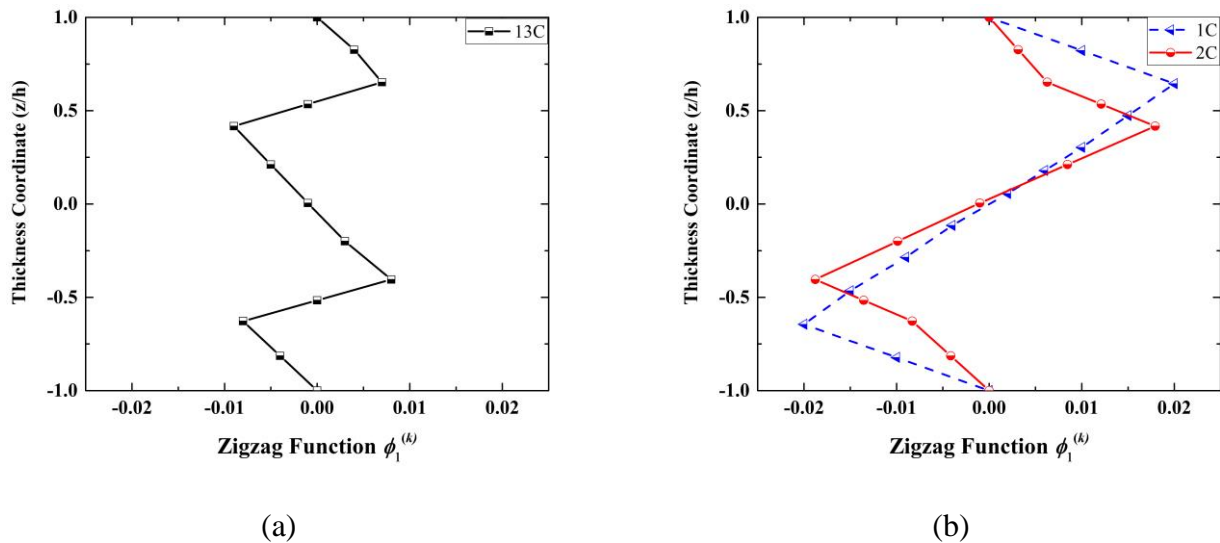
Fig. 1-12. Zigzag function values through the thickness for hybrid fiber samples (a) 13C (b) 1C and 2C

Table 1-5. FEM results for the maximum displacements in tensile conditions

| Laminate | $u_{max}$ [mm] | $v_{max}$ [mm] | $w_{max}$ [mm] |
|---|---|---|---|
| AC | $1.570 \times 10^{-2}$ | $5.652 \times 10^{-4}$ | 0 |
| 13C | $2.055 \times 10^{-2}$ | $7.020 \times 10^{-4}$ | $1.400 \times 10^{-2}$ |
| 1C | $3.184 \times 10^{-2}$ | $9.981 \times 10^{-4}$ | 0 |
| 2C | $2.852 \times 10^{-2}$ | $9.084 \times 10^{-4}$ | $-1.422 \times 10^{-1}$ |
| 3C | $3.249 \times 10^{-2}$ | $1.018 \times 10^{-3}$ | $9.647 \times 10^{-2}$ |
| AG | $7.058 \times 10^{-2}$ | $2.070 \times 10^{-3}$ | 0 |

The maximum values of the $u$, $v$, $w$ displacements obtained from the RZT-FEM analysis of the tensile test are listed in Table 1-5for each laminate. These displacement results correspond to the tensile loading condition of $P_0$ described in Section 3.3. It can be inferred from the Table 5 that the trend of the $u_{max}$ displacements between laminates are consistent with those of experimental results. For instance, the AG laminate shows the highest displacement in loading direction, whereas the AC laminate presents lowest displacement under the same loading condition. The hybrid specimens show values in between non-hybrid composites and give similar trend as seen in experiments. Expectedly, the contraction ($v$ displacement) along $x_2$ direction is about two orders of magnitude smaller than the axial displacement as shown in Table 1-5. To make a convenient comparison between all laminates under same loading condition, the maximum values for $u, v, w$ displacements over each laminate are utilized to obtain normalized displacements as:

$$\bar{\chi} = \frac{\chi}{|\chi_{max}|} \quad (\chi = u, v, w) \tag{22}$$

According to the RZT-FEM analysis, the variations of the average in-plane displacements $u$ and $v$ are linear along the length and width of the specimens, respectively. This behavior is same for all the laminates as can be seen from the contours of the $\bar{u}$ and $\bar{v}$ displacements in Fig. 1-13.



(a)



(b)
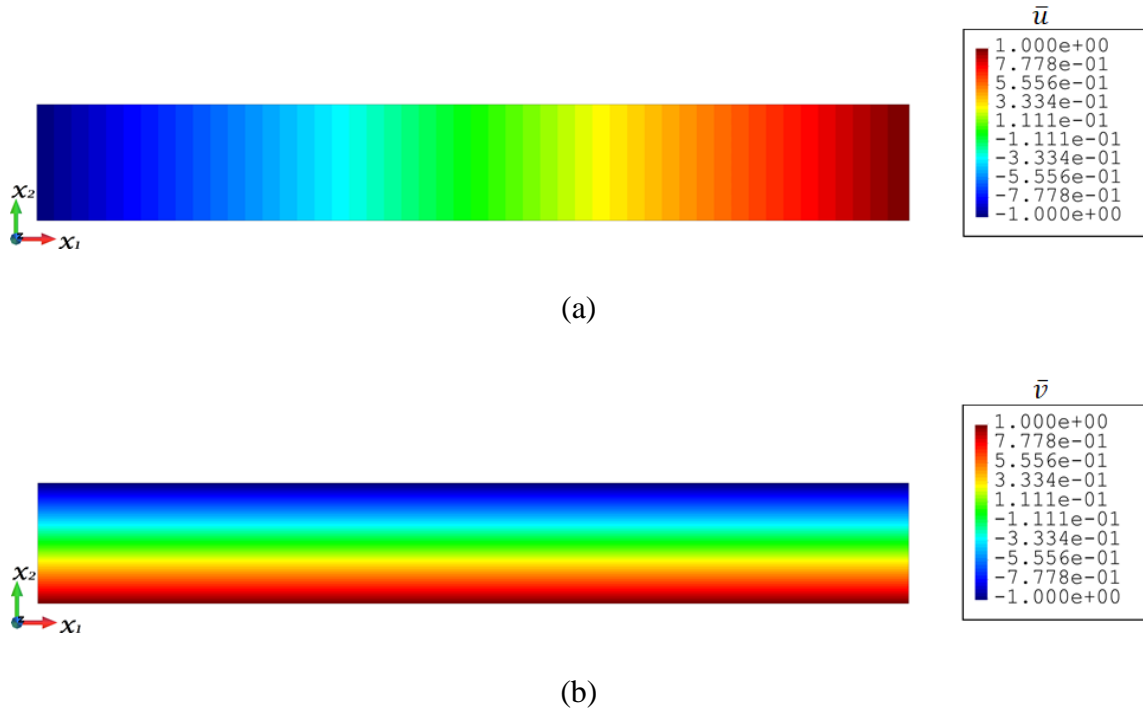
Fig. 1-13. Displacement results for tensile tests: In-plane displacements along (a) $x_1$ axis and (b) $x_2$ axis

Furthermore, there is no out of plane displacements produced by the single layer laminates (AC and AG) and sandwich hybrid laminate 1C. However, the hybrid laminate (13C), sandwich hybrid laminate (2C), and single layer laminate (3C) produced a significant amount of transverse displacement as compared to the $u_{max}$ displacements. Since the magnitude of all the displacement are considerably small in the linear-elastic region, this morphing behavior cannot be easily captured during the experimental tests. Nevertheless, the present RZT-FEM analysis exceptionally sheds a light to this important morphing phenomena of hybrid composites in the context of the current laminates investigated in this study. In fact, this morphing behavior is theoretically expected due to the antisymmetric distribution of the carbon-layers' thicknesses

44

with respect to the mid-planes of these laminates owing to the experimental variation. Note that although the glass-layers' thickness are antisymmetric for the 13C laminate, it has a negligibly low effect on the morphing shape of the 13C laminate due to the inherent low stiffness of the glass material as compared to the those of carbon materials. For the single layer laminates (AC and AG), the material properties are same through the thickness, thus the applied tensile force cannot produce any bending moments around $x_2$ direction of the structure. As a result, the transverse displacement becomes zero for these single layer laminates (AC and AG). In addition, 1C laminate also produces no out-of-plane deflection since the external carbon-fiber layers have the same thickness and the laminate is therefore symmetric. For the laminates producing non-zero transverse displacements, the contours of the normalized out of plane displacements are depicted in Fig. 1-14. These contours demonstrate that the amount of carbon available on the upper/lower side of the mid-plane has a significant effect on the direction of the morphing shape. For the 13C and 3C laminates, the total thickness of the carbon layer on the lower half of the laminate is higher than the upper one, hence the $\overline{w}$ displacement becomes positive at the half of the length. On the other hand, a vice-versa behavior is observed for the 2C specimen since the amount of the carbon available on the upper half of the laminate is higher than those of lower half.



(a)



(b)
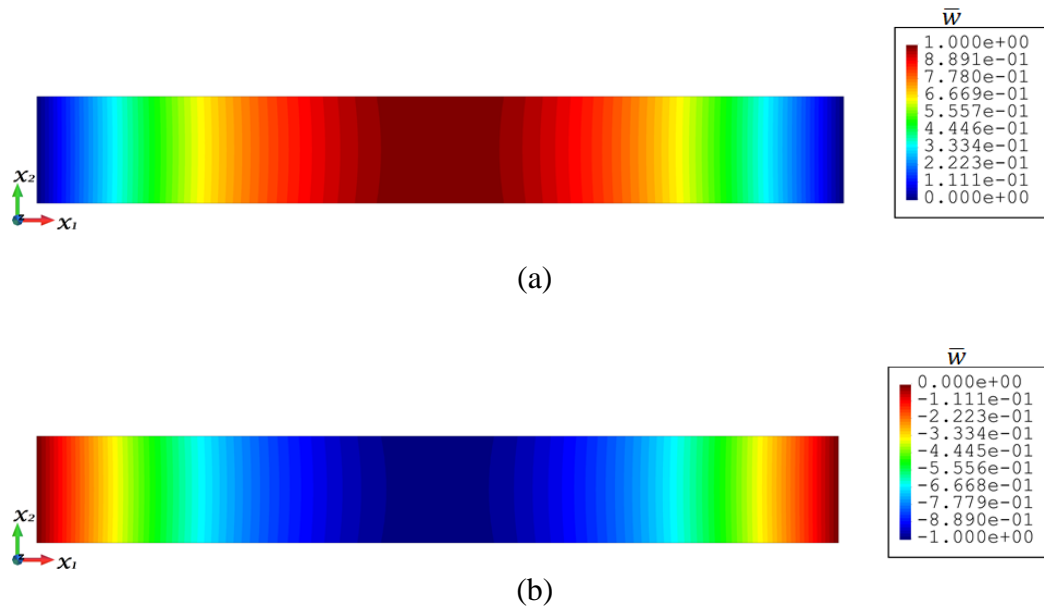
Fig. 1-14. Out of plane displacement for (a) 13C and 3C (b) 2C specimens

Finally, the deformed shapes of the laminates obtained from RZT-FEM analyses are presented in Fig. 1-15, where the total deformations are multiplied with different magnification factors (mf) to clearly visualize the morphing behavior of the laminates. Overall, these numerical results justify the importance and effect of through-the-thickness location of the high stiffness materials on morphing behavior of hybrid and/or sandwich-like laminates.
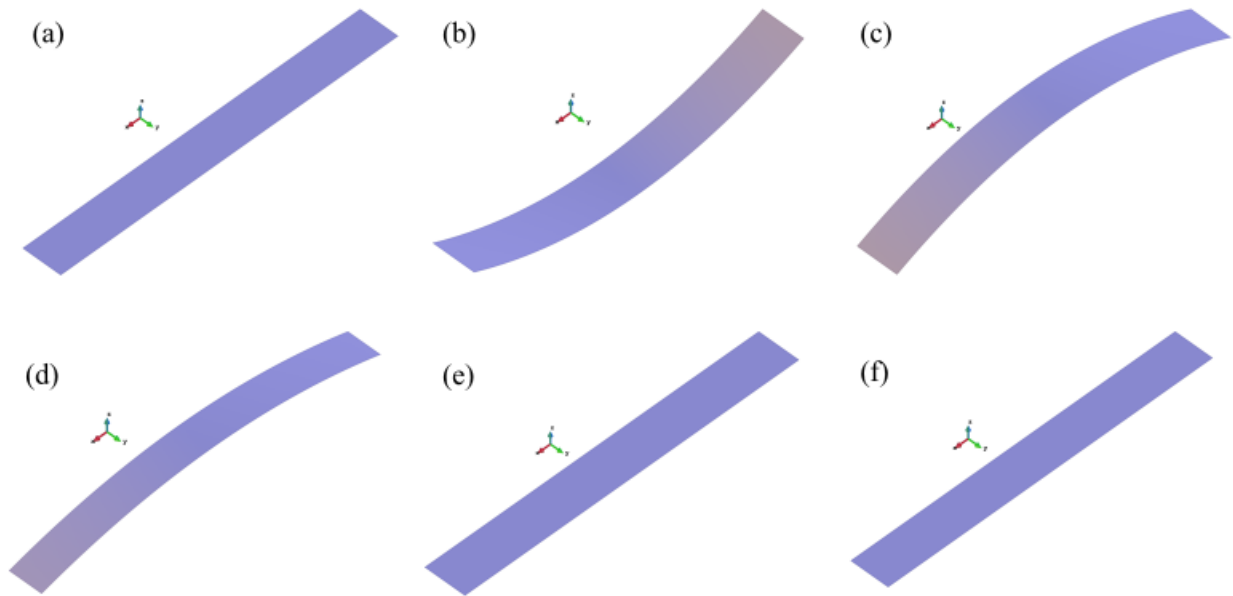


Fig. 1-15. Deformation results for tensile specimens (a) 1C [mf: 333], (b) 2C [mf:128], (c)3C [mf:204], (d)13C [mf:1030], (e) AC [mf:385], and (f) AG [mf:129]

In case of zero tensile load, no displacement occurs in the RZT-FEM model of the laminates. Therefore, once the displacement and/or strain results at any point are obtained from RZT-FEM analysis for a specific loading condition, the displacements/strains for other tensile loading conditions can be predicted based on the linear-elastic behavior of the laminates. In case of tensile samples, the loads are readily converted to stresses by dividing the applied tensile load over initial cross section area. Moreover, the stains of each tensile specimen are numerically evaluated based on RZT-FEM analysis at the exact position of the mounted strain gauge (bottom surface of specimens as shown in Fig. 1-2). To confirm the accuracy of the RZT-FEM models of tensile specimens, we compare the numerically obtained strain-stress relation of each

46

laminate with the experimental test results in Fig. 1-16. For this comparison, the linear region of strains given in the ASTM D3039 standard's guide, i.e., 1000με – 3000με, is selected. Note that this strain range is generally used to calculate the chord modulus of composite laminates under the tensile loading conditions. In Fig. 1-16, all the numerical results are in well agreement with those of experimental results such that the numerical and experimental results are almost indistinguishable from each other. This high precision and correlation between the results confirms the accuracy of the present RZT-FEM models experimentally.
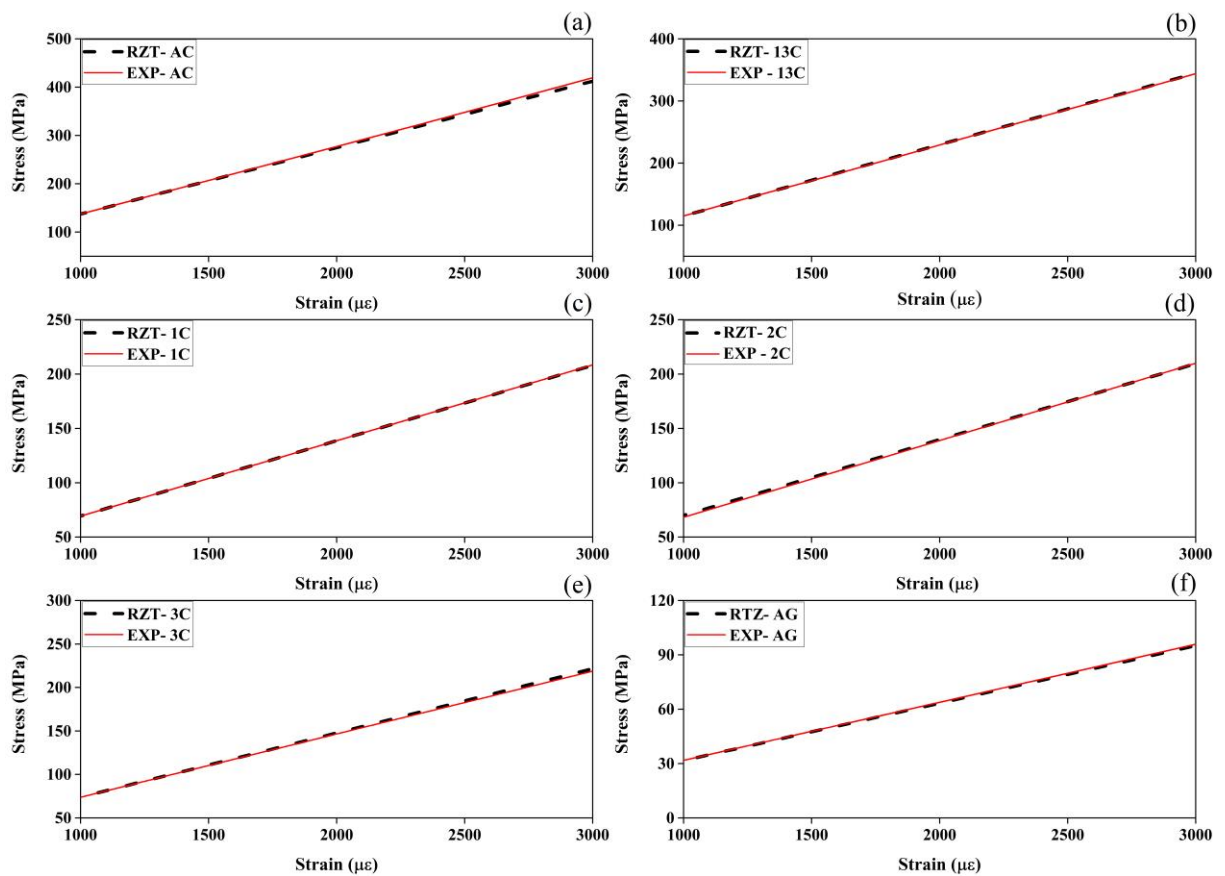


Fig. 1-16. Comparison of stress strain behavior tensile specimens between 1000 με and 3000 με. (a) AC (b) 13C (c) 1C (d) 2C (e) 3C (f) AG

In addition to the numerical results of tensile test, the maximum displacements along $x_1$, $x_2$, and $z$ axes, i.e., $u$, $v$, $w$, are attained from RZT-FEM analysis for the flexural load of $\bar{q}_0$

(given in Section 3.3) and listed in Table 6 for each laminate. In Section 3.4.1, the experimental results indicated that maximum amounts of deflection are obtained for the sequential order of AG, 3C, 2C, 1C, 13C, and AC respectively. As can be observed from Table 1-6, the same order for maximum deflections are obtained through the RZT-FEM analysis. Expectedly, the in-plane displacements corresponding to the non-hybrid single laminates (AC and AG) and sandwich like hybrid laminate, 1C, are zero (Table 1-6). On the other hand, 2C, 3C and 13C hybrid composites produced very small amount of transverse and axial (in-plane) displacements that are about three orders of magnitude less than maximum deflection amount which can be considered negligible in practice. Maximum values of deflections listed in Table 1-6 are used to get normalized deflection for each bending specimen. As can be seen from contour plots in Fig. 1-17, the $\bar{w}$ deflection for all the cases has the same quadratic variation along the span length and present maximum displacement at the mid-span. Besides, to better illustrate the final shapes of each laminate in the bending test simulation, the deformed shapes obtained through RZT-FEM model are presented in Fig. 1-18. For a clear comparison of the mechanical response of the laminates, the same magnification factor of 10 is used to enlarge the total deformations of the laminates in Fig. 1-18. This figure indicates that maximum deformation in hybrid laminates is related to 3C specimen, therefore it will show highest hybrid effect. Comparing the deformed shape of 1C, 2C and 3C laminates, it becomes very clear that placement of HE layers at middle plies would help for more deformation under same load value.

Table 1-6.  FEM results for the maximum displacements in flexural conditions

| Laminate | $u_{max}$ [mm] | $v_{max}$ [mm] | $w_{max}$ [mm] |
|:---:|:---:|:---:|:---:|
| AC | 0 | 0 | $-2.446 \times 10^{-1}$ |
| 13C | $9.88 \times 10^{-5}$ | $1.821 \times 10^{-5}$ | $-3.530 \times 10^{-1}$ |
| 1C | 0 | 0 | $-3.259 \times 10^{-1}$ |
| 2C | $1.016 \times 10^{-3}$ | $1.576 \times 10^{-4}$ | $-5.185 \times 10^{-1}$ |
| 3C | $6.85 \times 10^{-4}$ | $1.048 \times 10^{-4}$ | $-9.760 \times 10^{-1}$ |
| AG | 0 | 0 | $-1.115 \times 10^{0}$ |
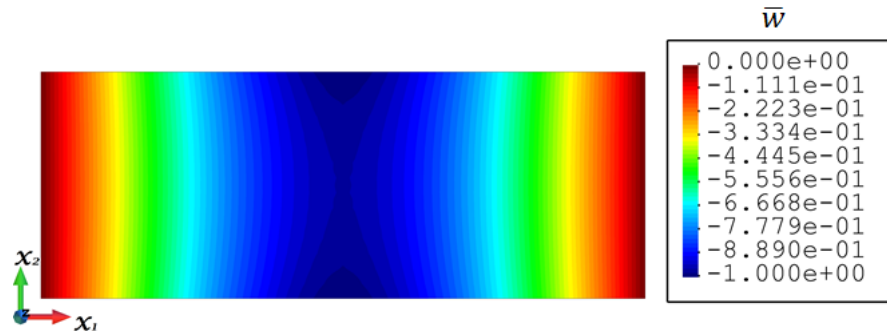
Fig. 1-17. Deflection results for bending test
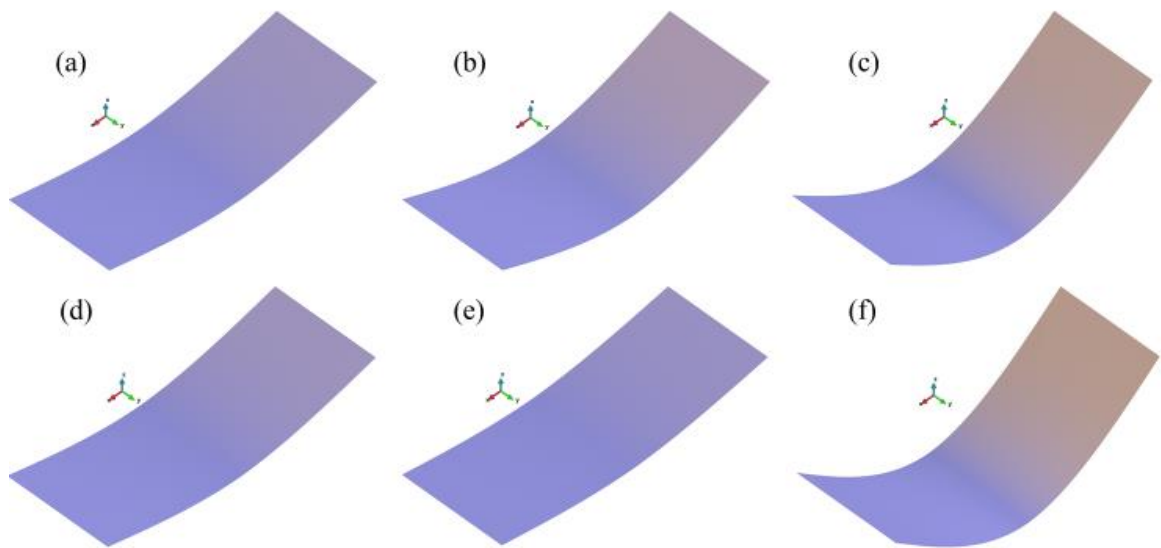


Fig. 1-18. Deformation results under flexural load [mf:10] (a) 1C, (b) 2C, (c)3C, (d) 13C, (e) AC, (f) AG

Analogous to tensile specimens, under zero load condition displacement quantities for flexural tests will be zero. Hence, obtaining one specific displacement from RZT-FEM analysis for a certain load can be used to get displacements in other load values based on linear-elastic behavior of laminates. One can easily convert these displacement and load data to strain and

stress values. For flexural loading condition, i.e., provided in three-point bending test guide of ASTM D790 standard, the following relationships are used to get flexural stress ($\sigma_f$) and strain ($\varepsilon_f$) at outer surface of specimen using load and displacement obtained from model:

$$\sigma_f = \frac{3\bar{q}_0 a}{8h^2} \tag{23}$$

$$\varepsilon_f = \frac{12h|w_{\max}|}{a^2} \tag{24}$$

Like the tensile test models, the strain-stress values obtained from bending models are plotted at linear-elastic strain range of 1000με – 3000με. Subsequently, these values are compared with corresponding bending tests' experimental data in the same strain region as shown in Fig. 1-19. Remarkably, RZT-FEM results are almost in perfect agreement with the experimental ones as depicted in Fig. 1-19. Hence, this high accuracy of the correlation between experimental and numerical results confirms the reliability of both experiments and RZT-FEM models for the linear-strain values.
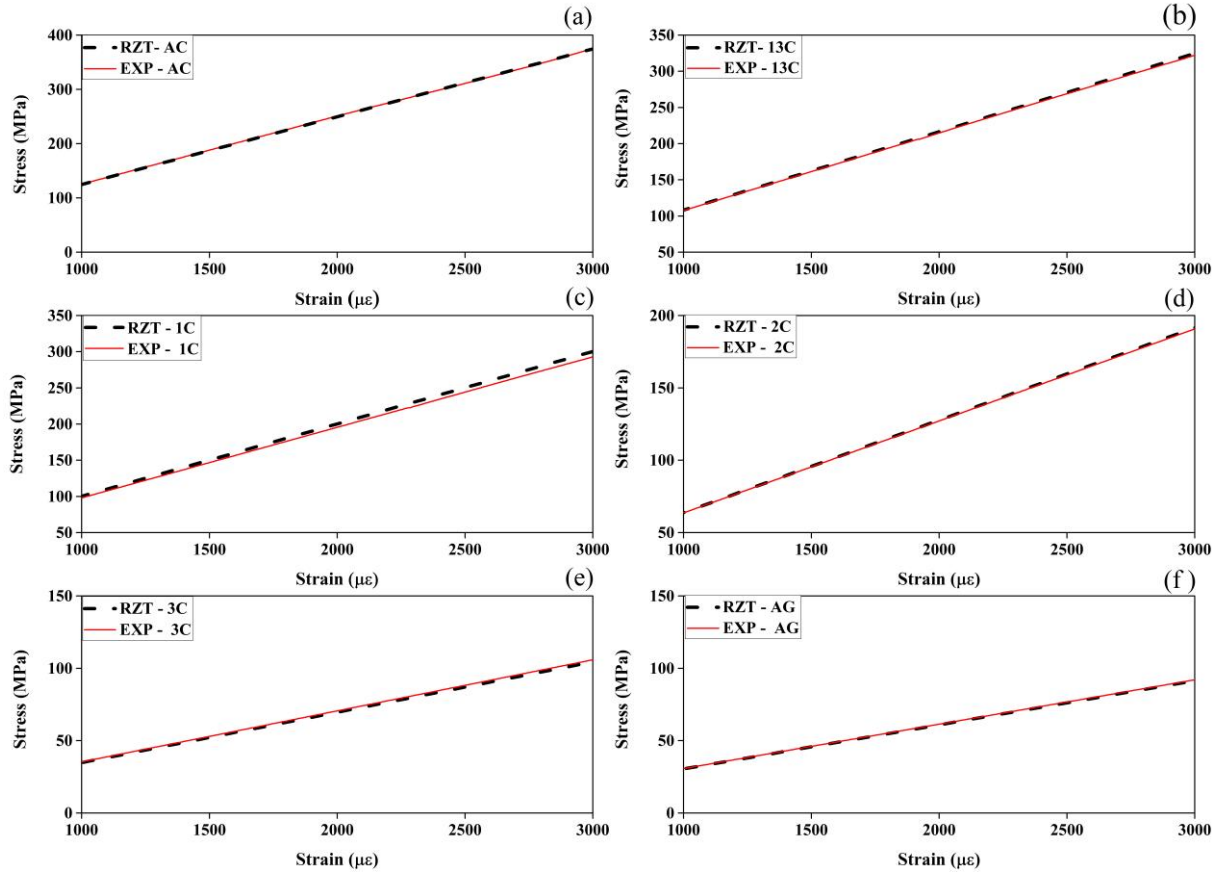
Fig. 1-19. Comparison of stress strain behavior of bending specimens between 1000-3000με. (a) AC, (b) 13C, (c) 1C, (d) 2C, (e) 3C, (f) AG

### 1.4.4 Clustering and Pattern Recognition of AE Data

The Fig. 1-20a and Fig. 1-20b represent the clustering results for acoustic data of tensile and bending tests of 2C specimens where in the legend as an inset, the percent of total acoustic emission hits for each cluster is also provided. Obviously, the total number of hits in bending specimen is less compared to that in tensile one due to the smaller volume of material involved in intense deformation. All hybrid specimen and non-hybrid composites reveal similar results, indicating four distinct clusters in partial power 1 versus weighted peak frequency (WPF) with the ranges of 50-160 kHz, 150-300 kHz, 300-400 kHz and 400-600 kHz. These ranges of frequencies will be referred to as $f_I$, $f_{II}$, $f_{III}$, and $f_{IV}$, respectively for convenience. According to a previous investigation by authors [31], the $f_I$ range corresponds only to transverse cracks in resin epoxy samples. So, in all recorded data for bending and tensile specimens, lowest

51

frequency range of WPF is due to crack initiation or propagation in matrix material. Consequently, $f_{II}$, $f_{III}$, and $f_{IV}$ ranges can be correlated with other damage types in current composite material systems such as matrix/fiber interface failures and fiber damages. Based on other results in literature, the interface failures would appear at lower frequencies compared to fiber breakage [30, 66]. Thus, $f_{II}$ and $f_{III}$ are most probably related to interface damages. To ensure that the highest frequency ranges are for fiber breakage, we have performed tensile test on bundles of carbon and glass fibers and the results are presented in Fig. 1-20c and Fig. 1-20d, respectively. These experimental results reveal that both fiber types fail at the same frequency range of $f_{IV}$ and no hits were obtained at lower ranges of WPF.



(a)                                                (b)
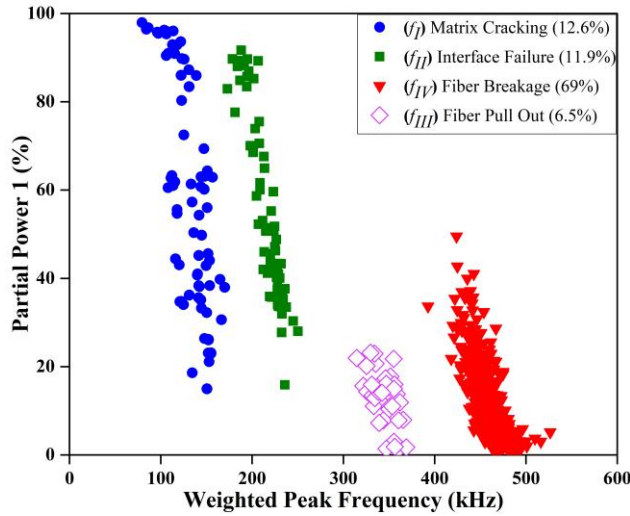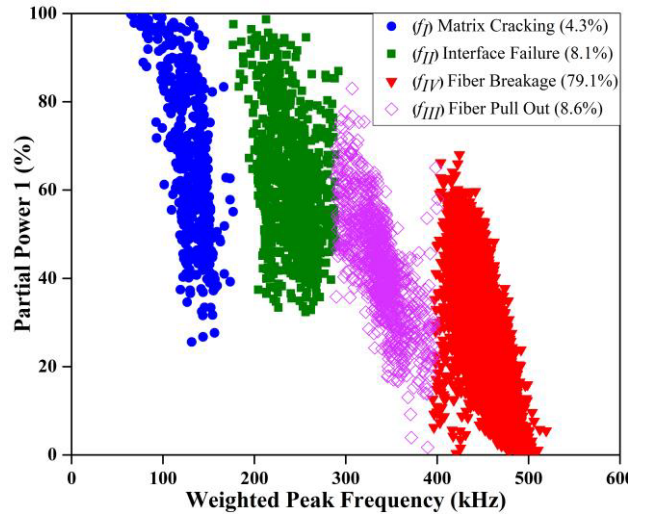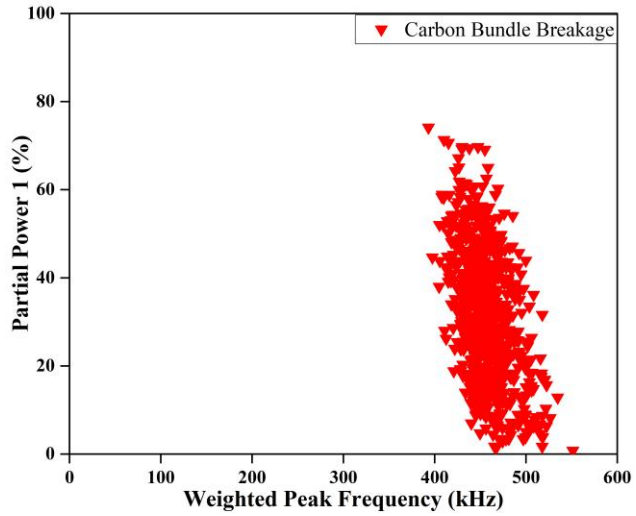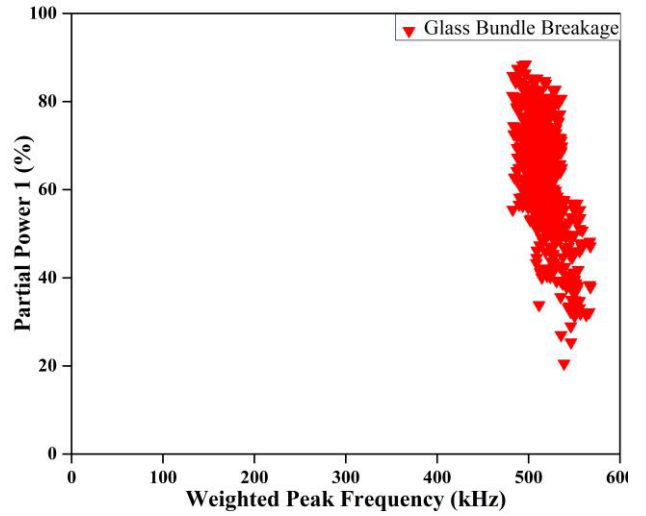
Fig. 1-20. (a) Clustering result of 2C bending hybrid sample, (b) clustering result of 2C tensile hybrid specimen, (c) AE results of carbon bundle, and (d) AE results of glass bundle

The remaining clusters of weighted peak frequencies, namely, $f_{II}$ and $f_{III}$, can be attributed to interface failures in between matrix and fibers since clusters of matrix and fiber failures have already been identified. Possible damage types include fiber pull out and interface failure. These two failure modes are the main determinants of fracture toughness in fiber reinforced polymer composites. Fiber pull out happens after debonding under tensile stresses in a cracked material. Thus, fiber pull out is common failure mode in tensile tests since whole specimen is ideally under monotonic tension. Moreover, in bending specimens, fiber pull out will take place only if specimen has high enough thickness to induce large tensile stresses at the lower half of the specimen. So, the probability of such a failure will be small and most probably will occur at the final stages of bending test when the tensile stress rises to a specific value above the strength of fibers.

To further elaborate on the characteristics of different signals for various clusters, the frequency domain magnitudes of sample waveforms from each cluster are obtained and presented in Fig. 1-21. As can be seen in Fig. 1-21a, matrix cracking corresponds to an abrupt increase at lowest frequency domain and gradual decrease in magnitude. This low frequency range is expected due to the lower density of resin epoxy as matrix material. Interface failure shows a peak at higher frequency range compared to matrix material with smaller magnitude

as seen in Fig. 1-21b, and this type of failure reveals several peaks from 150 kHz to 500 kHz with the peak frequency at about 200 kHz. Acoustic emission hit related to fiber pull out demonstrates frequency spectral with a higher peak frequency compared to interface failure as seen in Fig. 1-21c. The common points between Fig. 1-21b and Fig. 1-21c is that both damage types provide a wider frequency range near peak. Since these failure types are the result of interaction between two materials such as friction between fibers and matrix, their frequency spectral demonstrate multiple high peaks at various frequencies. Fig. 1-21d presents the frequency spectrum for fiber breakage. Since fibers have the higher elastic modulus compared to matrix, they show a peak frequency at a higher range of spectral. So, interface failures and fiber pull outs result in peak frequencies between ranges of peaks for constituents of composite materials.
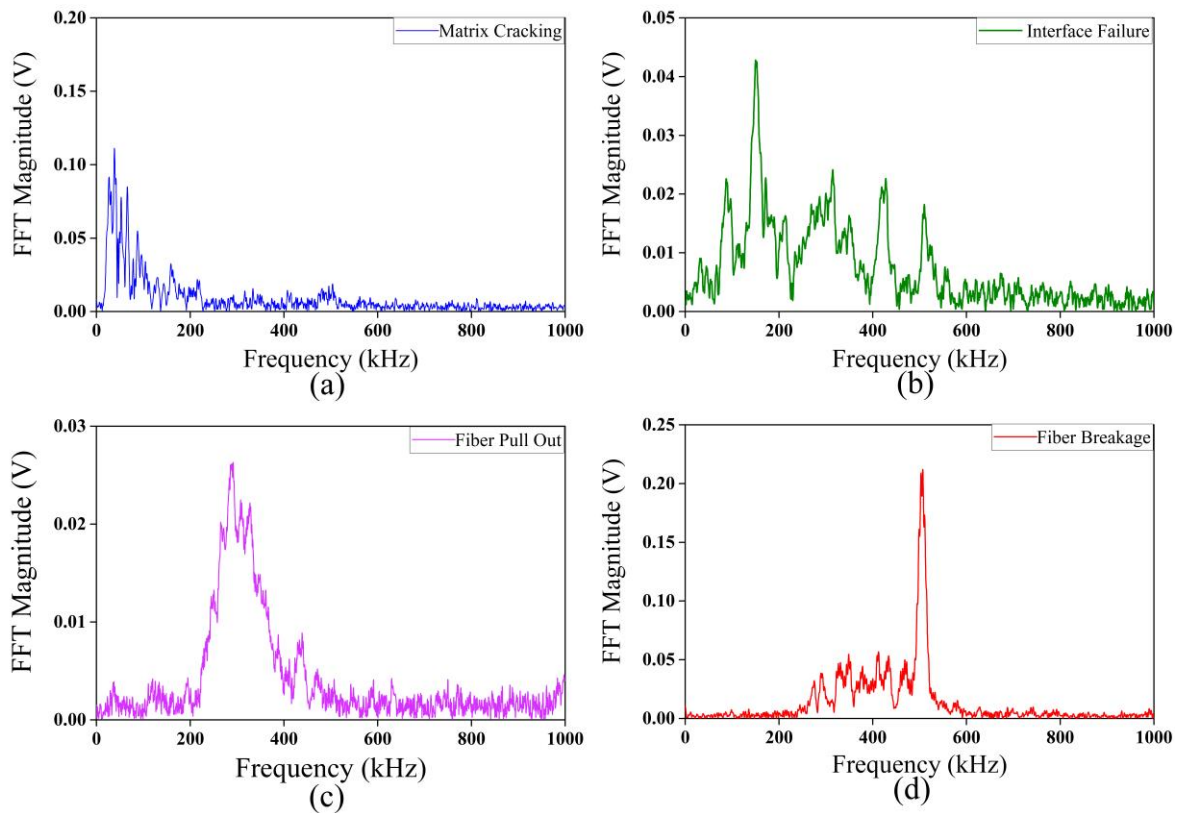


Fig. 1-21. Sample frequency domain magnitudes for each damage type (a) Matrix cracking, (b) Interface failure, (c) Fiber pull out, and (d) Fiber breakage

54

1.4.5    Damage Accumulation Analysis During Mechanical Tests

Fig. 1-22shows the results of stress-strain curves with cumulative counts of acoustic emission amplitudes passing the defined threshold during the test.  Fig. 1-22b to Fig. 1-22f reveal that initial damages in bending specimens are related to high frequency damages, i.e. fiber breakage. Therefore, buckling of fibers at upper surface of bending specimens is the major damage type in bending tests, which conforms with the results that can be inferred from Fig. 1-8. The acoustic emission activity for AC, 13C and 1C laminates started at strain levels less than 6000$\mu\varepsilon$, while for 2C, 3C and AG it initiates at flexural strains above 10000$\mu\varepsilon$. In Fig. 1-22a as soon as the experimental data deviates from RZT model, represented as dashed line, acoustic emission activity starts, which can be inferred as initiation of major damages inside AC laminates which causes change in material stiffness. In Fig. 1-22b the start of acoustic emission activity and deviation point of model from experiment match very perfectly at about 5500$\mu\varepsilon$. Various damage types accumulate inside laminates afterwards just before the point of catastrophic failure, the amount of acoustic emission counts soars for all failure types and the specimen breaks down spontaneously. An interesting observation can be made as to nearly concurrent start of matrix cracking, interface failure and fiber breakage for 1C specimen in Fig. 1-22c. Given that this laminate is very similar to composite sandwich panel with a stiff surface plates and softer core material, RZT model has been able to accurately predict the damage accumulation point for this hybrid laminate. Fig. 1-22d and Fig. 1-22e also indicate start point of damage initiation just after the deviation of experimental results from RZT model, the damage accumulation is proportional to the increase of difference between model and experiment. These results show that despite almost linear behavior of material, various damage type grow and increase in number inside the material. As seen in Fig. 1-22e deviation point of experiment from model appears somehow before the acoustic emission recording initiation, this small difference is attributed to possible attenuation of acoustic emission waves  due to minor damages at the beginning which is not recorded by piezoelectric sensors [68].

As seen in Fig. 1-22a to Fig. 1-22f, fiber pull-outs occur at final stage of bending tests. Acoustic emission counts related to this damage type are very small compared to other failure types. This observation is consistent with what has been discussed in previous sections regarding the rareness of fiber pull out under flexural loading. As seen in Fig. 1-22c, 1C

laminate does not show any acoustic emission activity associated with the fiber pull-out. If one carefully analyses the Fig. 1-22b and Fig. 1-22c, it can be observed that acoustic emission activity levels off after a steep increase, which corresponds to earliest step wise drops in the stress-strain curve due to the initial failure at top surface plies. Since the initial failures are associated with the buckling of carbon fibers, their further development into middle plies is inhibited by the presence of lower stiffness glass fibers therein. Effectively, glass plies act as crack or damage arrester and enable the laminate to carry the applied load despite the loss of integrity in the hybrid composite system. As in the case of 2C and 3C specimens given in Fig. 1-22d and Fig. 1-22e, acoustic emission activities constantly increase until the final stages of failure indicating that carbon plies cannot hinder the propagation of damages initiated from the surfaces. The reason for this behavior at 2C and 3C hybrid samples is higher stiffness of carbon layers. The damage accumulation for these laminates is like non-hybrid specimens even though they can bear higher strains.

The comparison of Fig. 1-22e and Fig. 1-22f reveals the similarity between acoustic emission activity of 3C and AG laminates, which indicates their analogous failure development. The strain level for failure initiation demarcated by the starting of acoustic emission activities is smaller for 3C laminate compared to AG sample, which indicates that the presence of carbon plies at middle layers of 3C bending specimen leads to an increase in stiffness of the composite. The analysis of acoustic emission activity reveals that the presence of LE carbon layers stiffens HE glass plies adjacent to them in flexural loading condition and can change damage initiation and development accordingly.

Fig. 1-22g shows the acoustic emission behavior for non-hybrid AC laminate in which the counts of acoustic emission set off with the same slope for almost all damage types but then increases suddenly at final stage of loading around 8000με. This sudden upsurge of acoustic emission counts characterizes catastrophic cracks growth and global failure of carbon laminate. The observation of acoustic emission counts for AG specimen in Fig. 1-22*l* shows similar trend albeit with a smaller slope at final stage. This behavior can be associated with higher strain energy required to propagate cracks in glass laminates due to the more ductile nature of glass plies. As seen in Fig. 1-22g, the damage accumulation starts at very law strain values of less

than 1000με, while RZT model deviates from experiments at about 2000με, deviation point however coincides with a sudden increase in acoustic activity related to Fiber breakage. This concurrency indicates that model is successfully able to predict major damage occurrence in this composite laminate. The same observation is seen in Fig. 1-22h to Fig. 1-22*l*, for these laminates deviation of experiment from model corresponds to fiber breakages in the material. This observation clearly shows that high frequency emissions, i.e. fiber breakage, inside the hybrid composites corresponds to major change in material stiffness and thus loss of integrity.

The strain level in hybrid composites, corresponding to catastrophic failure of AC laminate (i.e. 8000με) in Fig. 1-22g to Fig. 1-22k shows that the acoustic emission activities for hybrid composites experiences a notable increase, which is also observable from the change in the slope and is indicated between as the region between dashes lines. This escalation shows establishment of critical damages at carbon plies of hybrid composite, yet the global failure of specimen is postponed due to presence of less stiff glass fiber plies. Acoustic emission activity somewhat levels off afterwards without any associated step wise-drop-and-rise in the strain-stress curve as in the case of 1C and 13C bending specimens. This behavior indicates that although glass plies increase the strain energy necessary for complete failure in comparison to AC specimen, they do not function as a crack arrester under the tension load and damage does not develop into the material in a transverse path. The presence of significant interlaminar delamination in glass layers as already mentioned in Fig. 1-11 represents the presence of bending stresses at the interface between glass and carbon laminas. The weakness between carbon and glass plies interface was also mentioned for 2C and 3C bending laminates in Fig. 1-8g and Fig. 1-8i, for these samples damage develops toward midplane of specimen from surface and then stops as a delamination at glass and carbon plies where there is considerable interlaminar transverse shear stress as predicted by RZT model. This behavior indicates that for hybrid specimens, transverse shear stresses between glass and carbon laminas can cause delamination as a strain energy release method.

Failures at frequency range of $f_{III}$ corresponding to fiber pull out damage show higher activity under tensile loading condition which is due to existence of tension forces on fibers from the initial stages of tensile test. It is worth noting that acoustic emission activity associated

with fiber breakage in all tensile tests surpasses acoustic emission activity related to other damage types. This observation clearly shows that fibers are main load carriers under loading condition and due to their low ductility, they cannot store strain energy as in the case of more ductile matrix and thus release it faster upon breakage. So, fiber breakage failures contribute to damage propagation more than other failure modes as acoustic emission activities show.
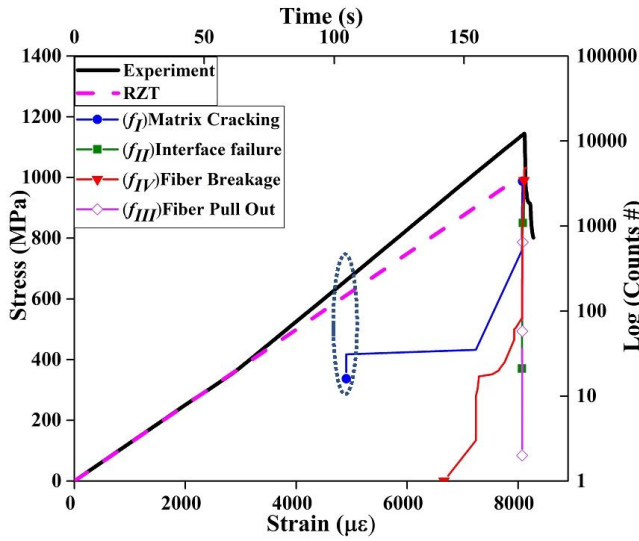


(a) AC Bending
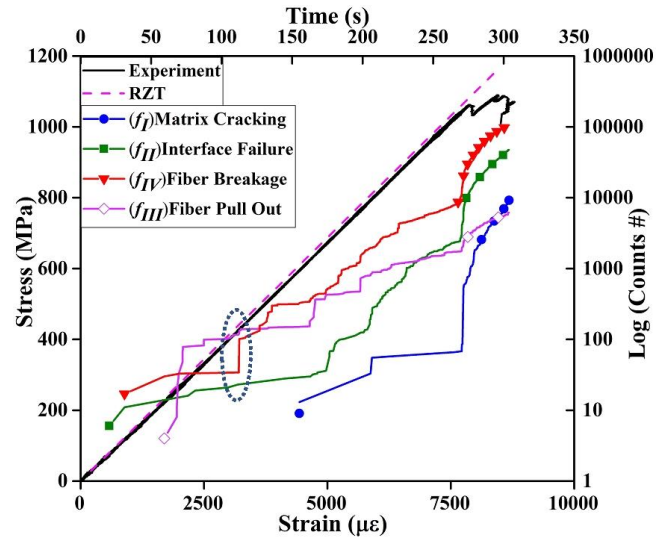


(g) AC Tensile
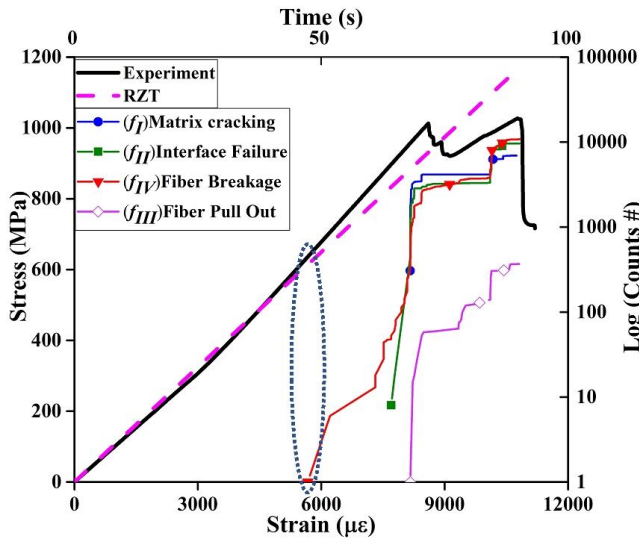


(b) 13C Bending
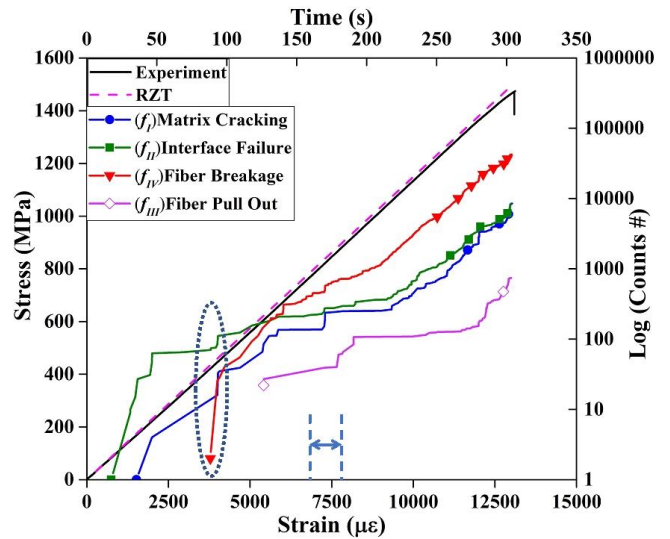


(h) 13C Tensile
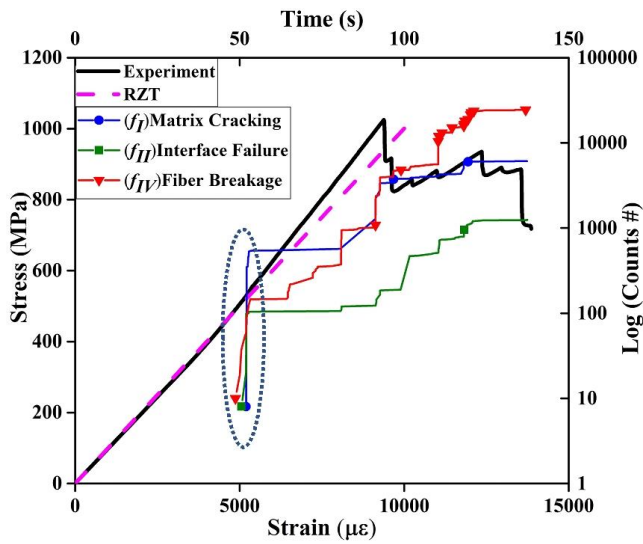
(c) 1C Bending
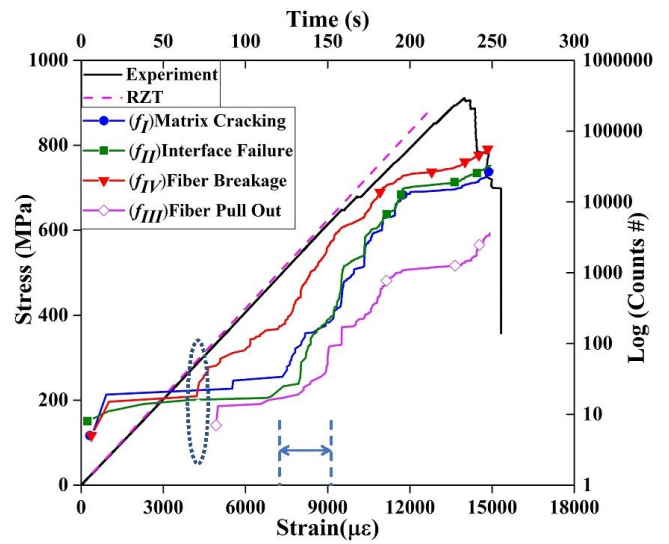


(i) 1C Tensile
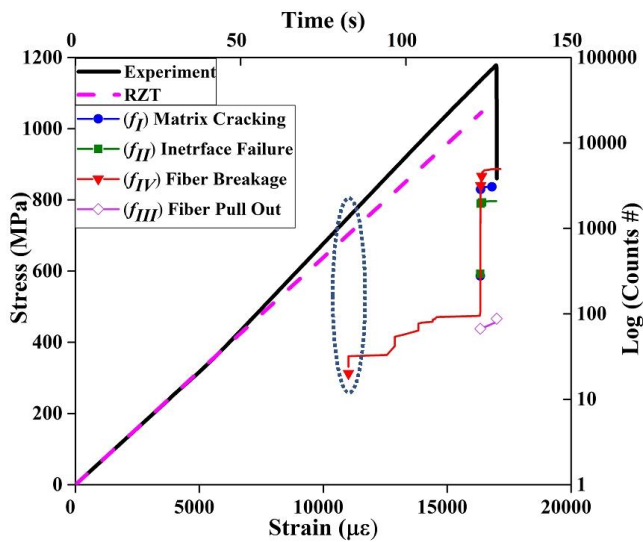


(d) 2C Bending
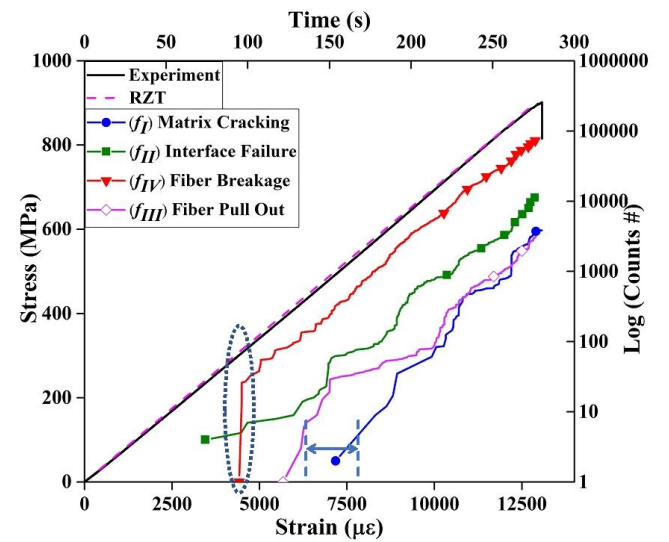


(j) 2C Tensile
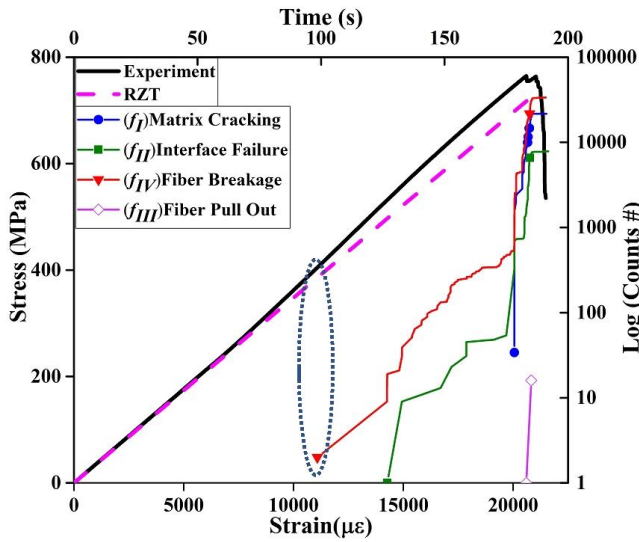
(e) 3C Bending
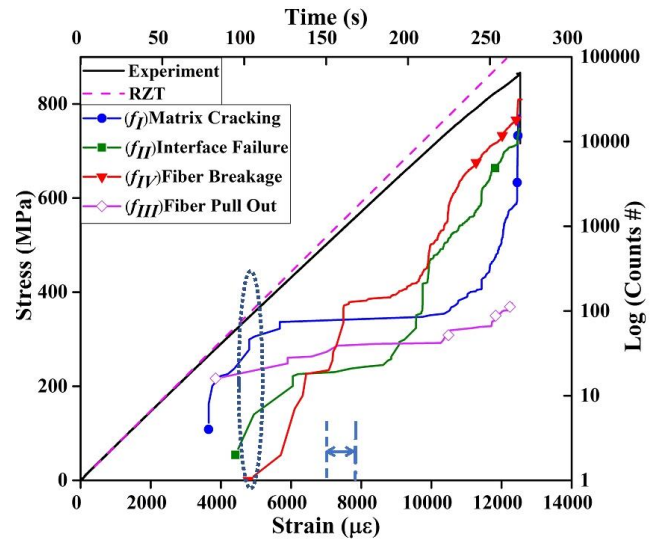

(k) 3C Tensile
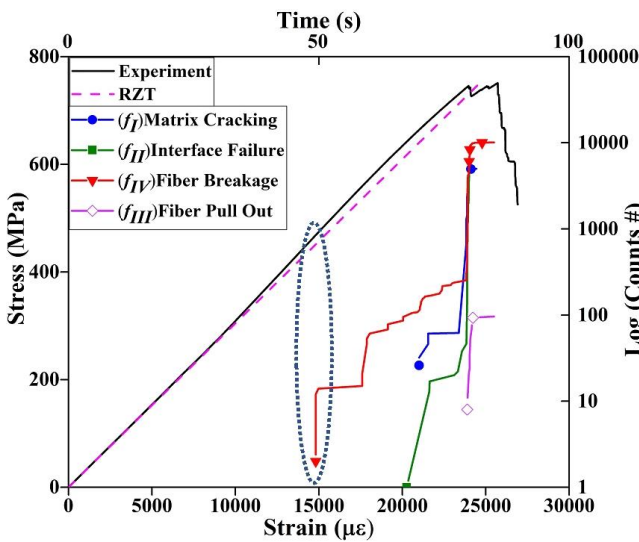

(f) AG Bending
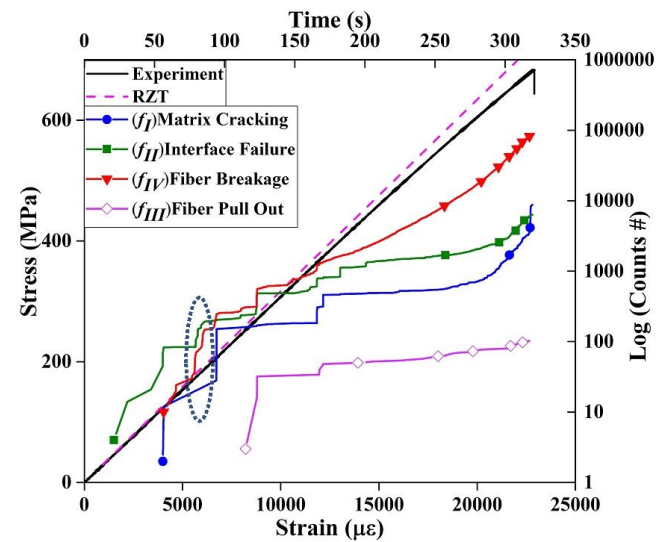

(l) AG Tensile

Fig. 1-22. Merged Plots of Stress strain and cumulative acoustic emission counts during tests for (a) AC Bending, (b) 13C Bending, (c) 1C Bending, (d) 2C Bending, (e) 3C Bending, (f) AG Bending, (g) AC Tensile, (h) 13C Tensile, (i) 1C Tensile, (j) 2C Tensile, (k) 3C Tensile, and (l) AG Tensile. (In all figures dotted oval indicate deviation points of experiment and model)

1.5 Conclusions


A combined numerical and experimental study, i.e., RZT and acoustic emission methods, is performed to investigate mechanical behavior and hybrid effect of hybrid laminates successfully. The mechanical test performed on hybrid and non-hybrid composites reveal the occurrence of hybrid effect. However,  it is seen that higher hybrid ratio does not necessarily result in higher hybrid effect values. Acoustic emission analysis of recorded data indicates that four weighted peak frequency ranges can be attributed to four different failure types happening in laminate. These failure types are matrix cracking, interface failure, fiber pull out and fiber breakage which correspond to 50-160 kHz, 150-300 kHz, 300-400 kHz and 400-600 kHz of weighted peak frequency, respectively.


The results of flexural tests for hybrid composites signify that development of damage from surface of specimen depends very much on the stiffness of layers beneath the surface. The closer the LE plies to midplane of laminate, the more hybrid effect is observed and no stepwise drop and rise of the stress in the stress-strain curve is seen. On the other hand, using LE fibers at surface of laminate with HE plies beneath leads to stepwise drop and increase of stress in the stress-strain curve. Analysis of acoustic emission signals during flexural test easily helps to interpret this difference. Acoustic emission data shows that acoustic activity levels off after first drop of stress which means halt of failure development due to high ductility of HE laminas under the surface plies. Moreover, microscopic images taken from cross section of failure area of flexural samples reveals failure advancement across midplane of laminate if LE carbon plies are at midplane region, while glass plies prevent progress of damage by delamination. Mechanical data analysis for tensile tests on the other hand reveals that volume fraction of LE and HE fibers is responsible for magnitude of hybrid effect obtained.


In addition to the acoustic analysis, a successful analogy between each laminate type and a sandwich structures is created by using RZT-FEM analysis. The RZT models are successfully validated against experimental results and utilized to predict the failure initiation of hybrid laminates under various mechanical loading. Herein, the deviation of RZT-FEM results from

experiment model indicates initiation of damages under bending loads conditions while this deviation in tensile conditions corresponds to major high frequency damages, i.e., fiber breakage. The occurrence of interlaminar delamination for hybrid composites after breakage of carbon fibers is attributed to presence of transverse shear stresses obtained through deformation analysis of RZT-FEM model. Overall, these transverse-shear stresses increase tendency for delamination as a strain energy release path for the system and prevent successful load transfer to HE glass layers.

# Paper 2.    Using DIC for In-situ Strain and Damage Monitoring in Hybrid Fiber Laminates Under In-plane Shear Loading

Utilizing resistive strain gauges for V-notch shear tests in fiber reinforced laminates is usually limited to low strain values due to technical uncertainties imposed by the measurement technique and also the progressive damage development in notched region of the composite. Therefore, this study investigates an alternative approach by using digital image correlation system and further comparison with resistive strain gauge to identify the effect of heterogenous nature of damage development on measurement results. Moreover, glass/carbon fiber hybrid and non-hybrid laminates are tested in two major direction through the same approach to determine the effect of stacking sequence in spatial micro-damage accumulation. It is shown that tailoring appropriate region of interest for full field strain measurement at various stages of loading enables proper monitoring of micro-damage accumulation and thereby delivers a precise stress-strain behavior for hybrid and non-hybrid laminates. Comparison of the strain maps for hybrid laminates tested in $0°$ direction, shows that presence of carbon plies at the surface results in uniform strain distribution between the notches of the test sample. In contrast, a non-homogeneous strain map with separate regions of high strain gradient are observed for hybrid specimens with glass plies at surface, which can cause underestimation of average shear strain by resistive strain gauges. On the other hand, it is shown that strain maps for hybrid samples tested at $90°$ configuration is analogous regardless of the stacking sequence, and damage accumulation in these samples is most likely related to relative volume fraction of various fibers in hybrid laminate.

Keywords: Nonlinear Behavior; Hybrid Fiber Laminates; Full Field Strain Measurement; Damage Accumulation; In-plane Shear Test

2.1 Introduction

Carbon fiber reinforced polymers (CFRP) are used as engineering materials due to their high specific strength. However, they are known to suffer from limited damage tolerance. To address this major issue, several approaches have been proposed through the employment of multi-scale reinforcements or interface modifications of fibers in CFRP laminates [77-81]. Despite the relative success of these methods, their industrial applicability is under question due to the complex and expensive processing procedures. Alternatively, fiber hybridization is emerged to be a simple approach with promising results regarding extending the reliability of CFRP. In this method, a part of carbon fibers in CFRP laminate is replaced by another type of fiber reinforcement with higher elongation strain. Therefore, the total failure strain of hybrid fiber laminate is increased as compared to CFRP, i.e. the hybrid effect which improves the damage tolerance of CFRPs[17]. The hybrid effect comes in an expense of a small reduction in the strength of material which might be compensated by the increase in safety factor. However, the addition of other fiber types with different behavior than carbon fibers into the CFRP structure brings about complexities to its mechanical responses. Thus, understanding the mechanical behavior of fiber hybrid laminates is an important task that deserves attention.

There are comprehensive and recent reviews about the fiber hybridization of polymer laminates in [4, 18, 82] where the mechanical and physical aspect of such laminates are discussed thoroughly. Therefore, herein, only some recent and most relevant efforts about fiber hybridization of CFRPs are reviewed briefly. Biswas et al. showed that the magnitude of load for first ply failure in glass/carbon fiber hybrid laminates under a transverse static load is more than non-hybrid glass fiber reinforced polymer (GFRP) samples [83]. Wang et al. investigated the mechanical behavior of woven fabric hybrid carbon/aramid laminates under various loading conditions and showed the importance of stacking sequence on the flexural properties of hybrid samples [84]. Authors in their previous investigation obtained similar results for the flexural loading of glass/carbon fiber hybrid laminates [85]. Moreover, they determined the source of major damage initiation by the combined usage of acoustic emission and a theoretical model based on refined zigzag theory in these laminates. Naito et al analyzed tensile behavior of

glass/carbon reinforced thermoplastic laminates at various temperatures and used a Curtin-type global load-sharing model to predict the mechanical behavior of these composites [86]. Meng et al analyzed the damage behavior of hybrid glass/carbon composites under high-velocity impact and showed that increase in the thickness of glass plies improved impact behavior [87]. Czél et al. investigated the effect of thickness of a thin-ply carbon layer in glass epoxy laminates to observe pseudo-ductility in hybrid fiber composites [73]. It is clear that there are numerous researches on analysis of glass/carbon fiber hybrid laminates under tensile, flexural, interlaminar shear and impact loads. However, in these concisely summarized investigations, the main focus has been on the abrupt global failure of composite material or its transition to the pseudo-ductile state after elastic deformation. Besides, investigators are usually concerned about the effect of fibers on the mechanical response of hybrid fiber laminates, while the details of matrix dominant response in hybrid fiber laminates are not explored yet. When loaded under in-plane shear condition, fiber reinforced laminates exhibit an initial linear behavior followed by a nonlinear response. Such a nonlinear matrix dominant behavior is usually accompanied by damage development.

One of the promising methods for in-plane shear analysis of fiber reinforced laminates is V-notch (Iosipescu) shear test whereby the shear strain, stress and modulus of the composites can be determined. The presence of almost uniform shear stress throughout the V-notch section and zero bending moment in this method allows for the determination of shear modulus under pure shear stress/strain state [88]. Depending on orthotropy of the material and the loading condition, the shear stress between the notches might be nonuniform. Therefore, the selection of a conventional resistive strain gauge with appropriate size becomes particularly important to capture the strain field accurately across the V-notch region [89]. An alternative solution to local strain measurement can be the usage of full-field strain measurement techniques such as digital image correlation (DIC), where the region of analysis can be selected in accordance with requirement of the investigation. Bru et al. used DIC for the Iosipescu test of unidirectional weave non-crimp fabric polymer reinforced laminates and showed that the measured shear strain maps were uniform between notches even after the premature failure of samples due to multiple splitting at the notched region [90]. Choi et al. used DIC technique and finite element method (FEM) together to confirm the uniformity of shear strain between the notches and defined a correction factor for the calculation of shear modulus at lower strain levels [91].

Diayan et al. used DIC and numerical simulation to assess triaxiality ratio in shear tests of polypropylene based materials and employed this ratio as a factor indicating the deviations from shear states throughout the test procedure [92]. Qin et al. utilized DIC for analysis of local nonuniformity of shear strains in 3D orthogonal woven carbon/carbon composites, and revealed the effect of zone size on the shear strain calculation and on preventing the local strain alternations [93]. So far, the investigations on the in-plane shear test of polymer materials and composite laminates specifically have been dedicated to finding out the shear strain distribution at the V-notch zone through using a DIC method. To the best of the author's knowledge, no study has been conducted for determining the effect of stacking sequence in interply glass/carbon fiber hybrid laminates on the strain distribution corresponding to nonlinear region in the shear stress-shear strain curve between the notches. Furthermore, the strain values obtained by global and local strain measurements under shear test have not been contrasted to reveal significance of full field measurement technique for reliably monitoring the damage accumulation at nonlinear region of in-plane shear tests.

In the current study, details for manufacturing and processing of hybrid and non-hybrid laminates are given. The experimental evaluation method, i.e. the DIC method used for the characterization of shear behavior, is introduced. Then, a detailed discussion for construing results is presented as follows. Initially, the comparison is provided for the in-plane shear stress-strain curves based on strain measurements made through DIC and resistive strain gauge and the selection of appropriate size for the region of interest in DIC technique is discussed. Subsequently, the effect of stacking sequence on the nonlinear shear behavior of interply hybrid fiber laminates is elucidated based on the DIC driven shear strain maps for two different test configurations. Finally, the concluding remarks about the effect of stacking sequence, monitoring damage development in the nonlinear region using full-field strain measurement are laid out concisely.

## 2.2 Experimental Procedure

### 2.2.1 Materials and manufacturing procedure

Unidirectional carbon fibers with the areal weight of 300 g/m$^2$ density of 1.78g/cm$^3$ and tensile modulus of 240 GPa, and unidirectional glass fibers with 330 g/cm$^2$ (283 g/m$^2$-1200 Tex along the 0° direction, 37 g/m$^2$-68 Tex E-Glass stitching fibers along the 90° direction and stitch

66

with 10g/m$^2$ -76 Dtex) and a tensile elastic modulus of 80 GPa were used as reinforcing fibers. Araldite LY 564 resin and Hardener XB 3403 were used as the resin for the matrix purchased from Hunstman (USA). The glass transition temperature of the matrix material was 70℃ according to the manufacturer. Fabrics were cut with the size of 600 mm ×300 mm in a way that primary reinforcing fibers were aligned in the length of the cured and cut laminates. Six different stacking configurations as seen in

Table 2-1 were prepared on the heating table, i.e. mold. By using vacuum-assisted resin transfer molding process fibers were impregnated with the mixed components of the matrix material. The curing process of the set fibers was conducted according to the manufacturer's recommendation and the details of this process can be found in [85]. Furthermore, the density and fiber volume fraction of each laminate is also determined and reported in the previous study [85]. Furthermore, the fiber volume fraction of each laminate is also determined and reported in the previous study [85] where the relative volume fraction of glass to carbon fiber is determined experimentally for 13C, 1C, 2C and 3C laminates as 0.59, 1.19, 1.22 and 1.23, respectively.

Table 2-1 Stacking sequence of laminates and their designation

| Stacking Sequence | Laminate Label | Stacking Sequence | Laminate Label |
|---|---|---|---|
| [C/C/C/C/C/C] | AC | [G/C/G/G/C/G] | 2C |
| [C/G/C/C/G/C] | 13C | [G/G/C/C/G/G] | 3C |
| [C/G/G/G/G/C] | 1C | [G/G/G/G/G/G] | AG |

Two sets of V-notched beam shear test samples were cut from the cured laminates at 0$^o$ and 90$^o$ configurations, respectively. ZÜND G3-L3200 machine was used to cut samples according to ASTM D5379 as seen in Fig. 2-1. During the machining process, no delamination occurred, and the edges of the samples were grinded using sandpapers to achieve a smooth peripheral.
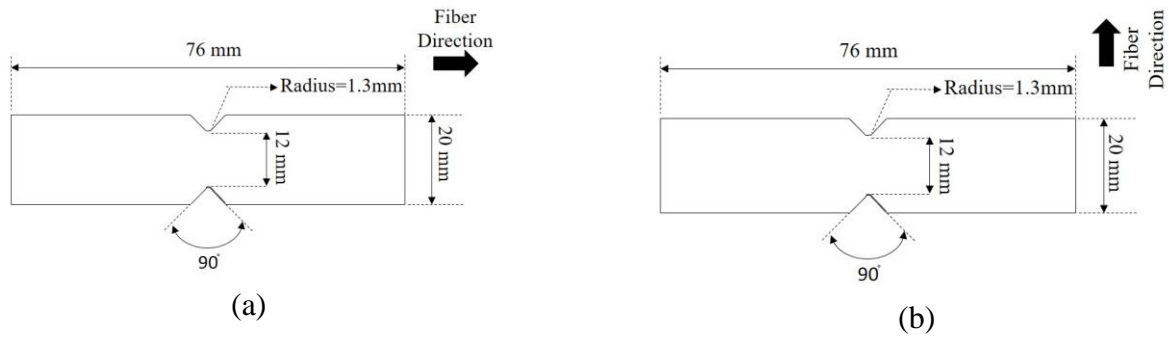
Fig. 2-1. Schematic of V-notch beam test samples in (a) 0º , (b) 90º configurations

### 2.2.2    V-notch Shear Test

To calculate the shear stress, the width ($w$) and the thickness ($h$) of the samples at the root section were measured prior to test initiation. Strain gauges with product code of C2A-XX-062LV-350 supplied from Vishay group were adhered to the back of the samples in between notches to collect the shear strain values in the middle of the specimens during shear deformation. Shear tests were conducted using INSTRON 8853 universal testing machine with a load cell of 250 kN, at a constant displacement-controlled speed of 2 mm/min. The samples were set in an Iosipescu shear fixture thus, the test load was applied through the root of the V-notched cross-section. The presence of vertically sliding parts in this fixture assured negligible friction, moreover out of plane displacements were prevented by using fastening pins. The value of the load ($P$) at each moment was transferred as an analog voltage to the full-field displacement measurement system, i.e. DIC. Therefore, the corresponding amount of load for any image taken through cameras was recorded simultaneously. The amount of the load was converted to shear stress ($\tau$) using $\tau = P / wh$ relationship.

### 2.2.3    DIC system

The local strains were acquired using a 12M digital image correlation system manufactured by GOM GmbH with 2 cameras, i.e. 3D stereo set up. To conduct the full-field displacement analysis, calibration of cameras and deformation sensor was conducted by means of a calibration panel of size 55 mm×44 mm in the single snap mode, therefore visibility of the surface of the test coupon under shear deformation was assured. The distance between cameras

was set to 436 mm and the distance between the center point of sensors and the material surface was 560 mm. The results of calibration showed a calibration deviation of 0.026 pixels and a scale deviation of 0.00 mm, which were under the limits of 0.050 pixels and 0.005 mm, respectively as indicated by the system manufacturer. A random black and white speckle pattern was applied on the surface of test materials to enable grayscale contrast, therefore each local set of pixels were distinguishable from their neighborhood pixels. A reference image of the surface of the samples was taken which indicated the undeformed state of the material for the measuring sensor. Thereafter a virtual surface element was defined for the sample in the DIC software by using the reference image. Small subsets (facets) with a certain distance (Steps) in between them were used as the identification points to define the surface element. During the deformation of the material sequence of images were taken from the surface of the material. An adaptive algorithm provided by the DIC system manufacturer was used to follow up the facets and their step to redefine the surface element for each image. Accordingly, the displacement values are calculated at each point on the surface element and converted to local strains. Three different regions of interest (ROI) , i.e. surface elements, were defined for calculation and presentation of strains for each laminate as seen in Fig. 2-2. The first region is the area between the loading tips of the test fixture. The second region of interest is the small band area between the notches of the samples and the third area has the same size as resistive strain gauge just adhered to the opposite side of the specimen.



ROI 1                     ROI 2                     ROI 3
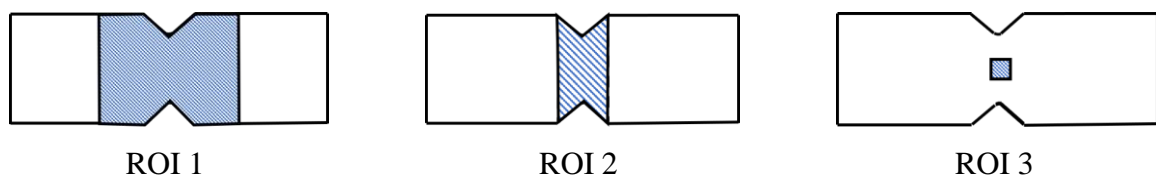
Fig. 2-2. Schematic of surface areas under investigation by DIC

2.2.4   Shear strain calculation through DIC

DIC system uses the deformation gradient tensor $F = \partial x_k / \partial X_K$ to map the material point in an undeformed state denoted by $X_K$ to the deformed state indicated by $x_k$ assuming that there is one to one correspondence between two states. Here, the subscripts $K$ and $k$

correspond to the undeformed and deformed states, respectively and take the values of 1-3 in Cartesian coordinates. The $F$ tensor can be decomposed as a polar product of a stretch tensor, $U$ and a rotation tensor $R$ as $F = RU$ where the stretch tensor can be calculated using Cauchy-Green strain tensor $C = F^T F = U^T R^T RU$. Since $R$ is an orthogonal tensor, i.e. $R^T R = I$, then Cauchy-Green strain tensor can be rewritten as $C = U^T U$. Thus, by using the materials tensor, DIC system can implement local coordinates on each point of the surface of the material to get the stretch ratios or respective strains in each point. For a pure shear stress case as seen herein for the V-notch cross section of test samples, no rotation is assumed and for each point on the surface, one can write coordinates of each deformed state as: $x_1 = X_1 + kX_2$, $x_2 = kX_1 + X_2$, $x_3 = X_3$, which leads to the deformation gradient in the form of $F = \begin{bmatrix} 1 & k & 0 \\ k & 1 & 0 \\ 0 & 0 & 1 \end{bmatrix} = RU = I \begin{bmatrix} 1 & k & 0 \\ k & 1 & 0 \\ 0 & 0 & 1 \end{bmatrix} = U$. Stretch tensor consists of the elements of stretch ratios ($Z$) which can be readily related to the engineering strain values. Thus, the stretch tensor can be rewritten in following form based on the values of strain: $U = \begin{bmatrix} 1+\varepsilon_x & \varepsilon_{xy} & 0 \\ \varepsilon_{yx} & 1+\varepsilon_y & 0 \\ 0 & 0 & 1 \end{bmatrix}$. So, DIC can easily get the strain values $\varepsilon_x$, $\varepsilon_y$, $\varepsilon_{xy}$ on the surface of the material if the stretch values of each points are known. Considering the symmetry of the tensor, $\varepsilon_{yx} = \varepsilon_{xy}$ and approximation of $\varepsilon_x \to 0$, $\varepsilon_y \to 0$ for an infinitesimally small deformation, shear strain will be given as $\gamma_{xy} = 2\varepsilon_{xy}$, which is equivalent to the term indicated in the standard ASTM D5379 for obtaining shear strain using strain gauge $\gamma_{xy} = |\varepsilon_{45°}| + |\varepsilon_{-45°}|$.

 2.3 Results and discussion

    2.3.1   Advantage of using DIC for in-plane shear characterization

   Results of shear strains measured through DIC and resistive strain gauge foil are presented in Fig. 2-3 and Fig. 2-4 for hybrid and non-hybrid samples at two different in-plane directions, i.e. 0° and 90° as demonstrated in Fig. 2-1. In each plot three different curves related to DIC measurements are given which correspond to various regions of interests as mentioned in Fig. 2-2, moreover the curves related to strain gauges are overlaid on these plots. The highest strain

values were obtained for ROI 3, while lower values were seen for ROI 2 and ROI 1, respectively at any stress level. Lower values of strain for ROI 1 was related to inclusion of areas on the surface of sample which did not experience shear deformation. At the beginning of the test these regions were under negligible shear stress due to inherent geometry of the shear sample, loading condition and consequently their location which was relatively far from the area in between the notches. As a result, the apparent slope of linear region, i.e. shear modulus, obtained using ROI 1 was higher as compared to ROI 2 and ROI 3 respectively for each sample. The results of strain collected by strain gauge in linear section of curves were perfectly matching with the values obtained by ROI 3 for all the specimens. This observation reveals that for laminates with symmetric layups, regions with the same size but in opposite sides of the sample would present analogous elastic behavior before start of the nonlinear response. Transition of the mechanical behavior from linear to nonlinear for each laminate was identified from a knee appearing in the curves. According to a previous research by the authors, start of nonlinearity at in plane shear test of the fiber reinforced laminates indicated onset of micro damage accumulation [34]. As seen in Fig. 2-3f such a transition is well presented by drawing two fitting lines at the linear and nonlinear sections of the curve and attributing the stress level of the intercept point between the two lines as the micro damage initiation stress. As seen in the inset plot of Fig. 2-3f, intercept points for all curves showed the same stress level. Hence, it was concluded that the stress level for micro damage accumulation in a laminate can be determined successfully regardless of the size of the selected measurement surface in DIC method and/or strain measurement technique. Comparison of ROI 3 with strain gauge in nonlinear region revealed that the good consistency of measured data by these systems continued up to 5% strain. For strains above 5% discrepancy in data measurements was observed which was related to reduction of data reliability for strain gauges due to their hardware limitations, i.e. 6% strain range. Moreover, due to different damage accumulation rate and microcrack initiation at various plies through the thickness of the test samples, the initial symmetrical layup was probably affected in terms of volume fraction of voids inside the specimens, therefore, the strain measurement results in opposite surfaces of sample altered. The other area of interest used for DIC measurements was ROI 2 which consisted of the surface area between notched regions of sample. This area was basically under pure shear from the beginning of the test; therefore, it could be assumed that it gave an average shear strain for the segment of the specimen under shear loading condition. Comparison of shear

failure point between various ROIs shows that ROI 2 gave a value in between ROI 1 and ROI 3, thus it provided more realistic value as compared to strain gauge and ROI 3. Also, the slope of linear region for ROI 2 had negligible difference with ROI 3 and strain gauge measurements. Therefore, two major properties of the shear behavior, namely, shear modulus and shear failure point, were best represented by ROI 2, in other words it could be concluded that ROI 2 gave better description for shear behavior for all samples up to a level where damages are mainly located in shear region of samples.

Comparison of shear behavior for 1C, 2C and 3C hybrid samples in Fig. 2-3showed that failure strains and maximum stresses in $90^o$ direction were lower than $0^o$ configuration, respectively. Early failure of samples in $90^o$ configurations as well as their lower stress values was related to rapid damage development in matrix/fiber interface under shear loading condition. On the other hand, higher failure strain for laminates in $0^o$ direction was related to gradual damage accumulation at matrix/fiber interface and growth of shear cracks [90]. It was seen that for samples tested in $90^o$ direction strain gauges showed highest failure strain while for specimens in $0^o$ direction ROI 3 presented highest failure strains. This observation was related to the disability of full field measurement system, since the DIC instrument was unable to sustain defined surface element for software measurements at regions with extreme shear strain values, in other words the. regions where matrix/fiber interfacial cracks grew instantaneously, DIC did not follow up the facets required in-plane displacement calculations. For specimens tested in $0^o$ direction shear cracks developed gradually at several locations in between the notches and also near the notch root. These shear cracks developed beyond the notched region which were not covered by strain gauge grid. Thus, ROI 2 and strain gauge were able to record shear strains up to a level where cracks were concentrated inside V notch region. Further damage growth was perfectly covered by ROI 3 and thus gave better presentation of the failure stages of samples in $0^o$ direction.

Fig. 2-4 shows the shear behavior of AG, AC and 13C samples in $0^o$ and $90^o$ directions. For AG-$0^o$ and 13C-$90^o$ samples, strain gauge failed earlier than expected in nonlinear region, therefore final failure stages were not recorded. However, based on previous statements we could assume that data obtained from ROI 3 was consistent with nonlinear region obtained with strain gauge. Therefore, it could be concluded that using DIC system is a good method for characterizing nonlinear behavior of fiber reinforced laminates as compared to resistive strain

gauges due to its capability to capture the full development of damages. Failure strain of AC-$90^{\circ}$ was very low as compared to all other non-hybrid and hybrid laminates. This low failure strain was related to big difference between elastic modulus of carbon fibers and epoxy resin matrix which contributed to easier crack development as interfacial debonding due to shear and consequent failure. When compared to AC-$90^{\circ}$ sample incorporation of glass fiber in matrix increased failure strain of 13C, 1C, 2C and 3C samples as seen in Fig. 2-3a, Fig. 2-3c, Fig. 2-3e and Fig. 2-4e, respectively, i.e. hybrid effect. Since the glass fibers were more ductile as compared to the carbon fibers, they provided less reinforcing effect, and consequently, stress concentration at their interface with matrix was lower and crack development from carbon layers to adjacent glass layers could be delayed [22]. Comparison of hybrid samples in $0^{\circ}$ direction with AC-$0^{\circ}$ specimen showed no significant hybrid effect which could be attributed to failure development as shear cracks rather sudden development of interfacial cracks aligned with loading direction. Initiation of failure in $0^{\circ}$ direction was mainly due to fiber deformation, matrix cracking and fiber/matrix interface failure [94]. The cracks originated due to these failures usually propagated in horizontal direction and were arrested due to excessive compressive forces away from v-notch region. Therefore, abrupt failure of samples in $0^{\circ}$ direction was not observed due to limited size of sample and fixture of the test. Effect of interfacial bonding becomes less significant as compared to samples tested in $90^{\circ}$ direction and hybrid effect was not seen for hybrid samples. In summary, using a bigger region of interest for monitoring the nonlinear behavior in in-plane shear test was advantageous, therefore, comparison of damage development at nonlinear region among various laminates was conducted using ROI 1 at the coming section.
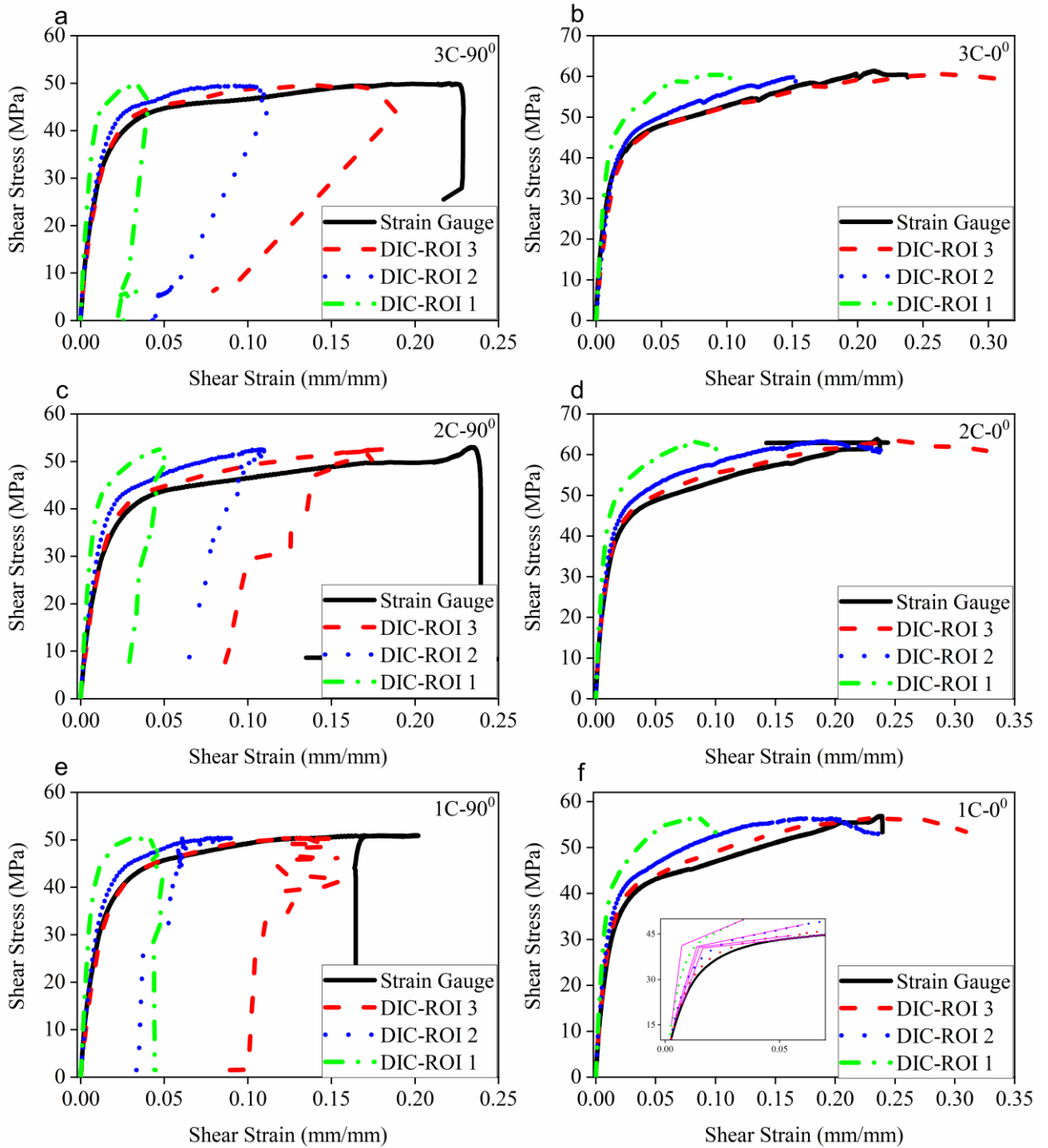
Fig. 2-3. Shear stress-strain curves obtained for various ROIs and strain gauge for (a)3C-90º , (b)3C-0º, (c)2C-90º, (d)2C-0º, (e)1C-90º, and (f)1C-0º
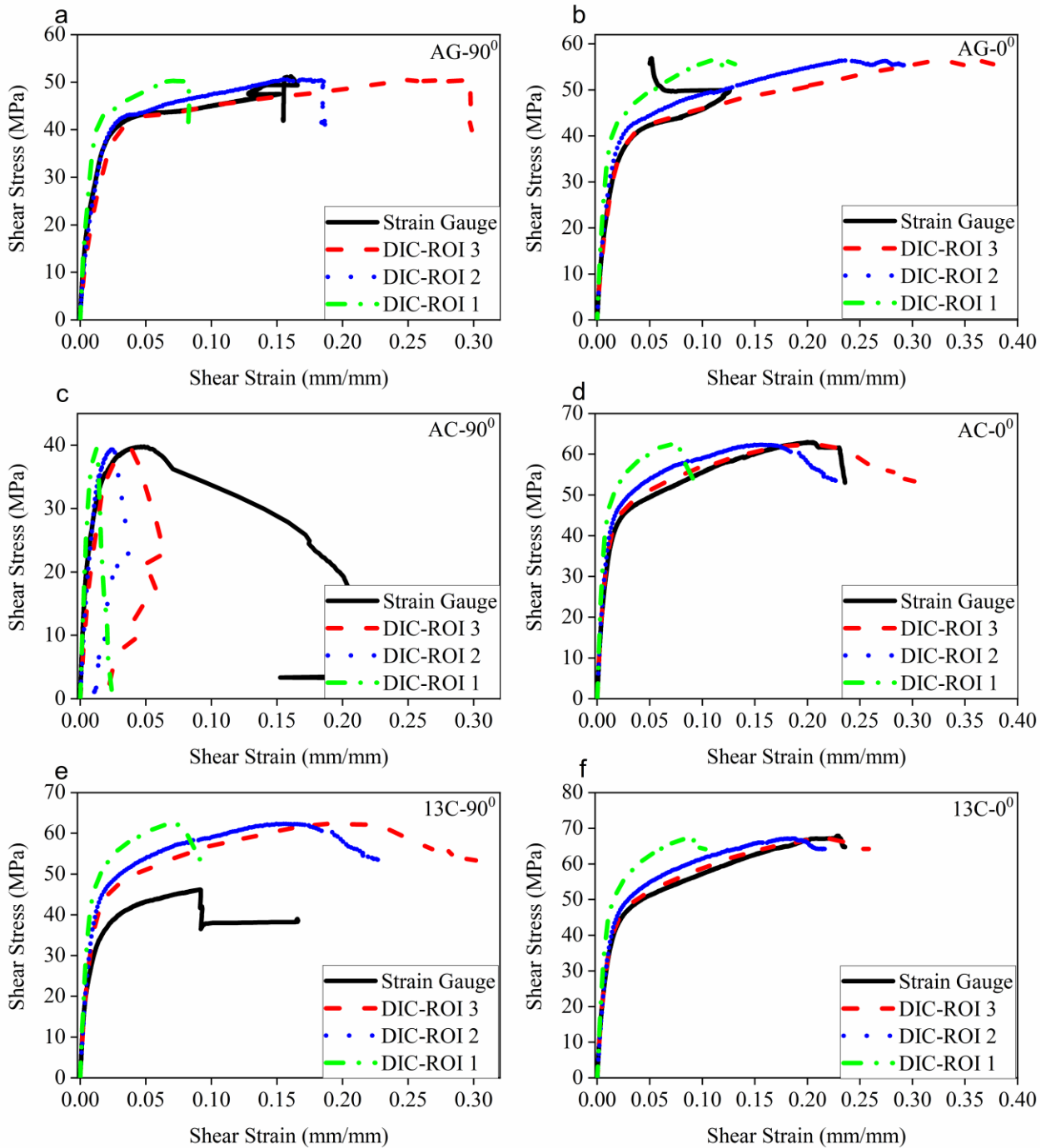
Fig. 2-4. Shear stress-strain curves obtained for various ROIs and strain gauge for (a)AG-90º, (b)AG-0º, (c)AC-90º, (d)AC-0º, (e)13C-90º, and (f)13C-0º

2.3.2    Effect of stacking sequence on development of damage at nonlinear region

Strain distribution for ROI 1 in various laminates at $0^o$ configurations was analyzed and compared using DIC-$\varepsilon_{xy}$ maps at 5% average strain and maximum load as observed under shear loading condition in Fig. 2-5. For all of the laminates a narrow band with high strain values was observed between the notches that corresponded to concentration of pure shear stress in that region. Initial nonlinearity of stress-strain behavior for all laminates appeared with creation of regions reaching $\varepsilon_{xy}$=0.02, i.e. orange color in strain color map. Considering the similarity of matrix system in all laminate, the analogous value of strain for initiation of nonlinear shear behavior could be attributed to micro damage initiation inside matrix constituent of the composite materials. Further accumulation of damage inside the laminates appeared as transverse strain gradients which developed normal to the loading direction as seen in DIC images of Fig. 2-5. Due to the orientation of fibers in $0^o$ configuration with respect to the loading direction, it was presumable that transverse advance of micro damage was mainly related to interfacial failure between fibers and matrix material. These interfacial failures later on showed up as inclined macro cracks in between the notches of the samples visible by naked eye, these type of macro cracks had also been reported for uni-weave NCF composites and glass fiber reinforced laminates [34, 90]. The damage initiation and growth had similar sequence for all laminates, however the extent of their development and consequent strain distribution appeared to be distinct, as seen in the results of Fig. 2-5. In the following paragraphs differences of shear strain maps are discussed between two groups of laminates based on the type of ply on the surface, namely carbon plies and glass plies. Moreover, the effect of stacking sequence on strain distribution is discussed for a group of laminates with similar fiber volume fractions, i.e. 1C, 2C, 3C.

In the case of samples with carbon plies at the surface, i.e. 1C, 13C and AC, initial high strain regions appeared adjacent to notch roots, this observation was consistent with previous study of the authors wherein thermal camera was used to indicate initial micro damage accumulation near notches [34]. These high strain regions near the notches promoted multiple transverse splitting as the loading increased and finally caused loss of DIC data at v-notch region as seen for maximum load images in all samples. It was interesting to note that unlike a previous report [90] these splitting events did not cause any visible stress drops in shear stress-

strain curve which could be associated with relatively smaller size of splitting in this investigation. After the formation of high strain regions near the notch roots, auxiliary high strain regions due to shear stress appeared uniformly in between the notches which indicated gradual micro damage accumulation. As mentioned earlier, transverse strain gradients were related to interfacial debonding between the fibers and matrix. The carbon fibers and resin epoxy have larger interface area and smaller interphase volume in between [95], therefore the load transfer from matrix to the fiber is more efficient as compare to that of glass fibers and matrix. Thus, better interaction of fiber and matrix resulted in homogenous failure development inside the carbon plies, and therefore, uniform strain distribution was observed at the surface of samples with carbon plies at the surface. As it is seen in Fig. 2-4a, Fig. 2-4g and Fig. 2-4i the region between the notches was more uniform for samples with carbon ply at surface as compared to their glass counterparts at 5% strain level. Such a uniformity of strain remained consistent up to the maximum stress level despite presence of higher shear strain values adjacent to the notch roots. On the other hand, DIC results for 2C, 3C and AG samples which had glass layers located at the surface showed that the damage initiation and propagation was different as compared to the previous group which had carbon plies at their surface. In these samples the transverse strain gradients did not develop uniformly but grew in discrete locations between the notches. These transverse cracks appeared due to easy growth of failures at weak fiber/matrix interfaces. On the contrary to the carbon fibers, the glass fibers had smaller interface and thicker interphase volume, which resulted in inefficient transfer of load from matrix to fibers and consequently promoted rapid growth of any interfacial failure. Therefore, for the samples with glass layers at their surface, strain distribution between the notches was nonuniform as seen in Fig. 2-5c,Fig. 2-5e and Fig. 2-5k and due to easier growth of the failure, higher strain values were observed as seen in Fig. 2-5d, Fig. 2-5f and Fig. 2-5*l* at maximum stress levels. These high strain regions later on appeared as inclined shear macro cracks which did not coalesce even up to maximum stress level. Moreover, after creation of the localized high strain regions, splitting at the notch roots occurred for these samples which caused loss of DIC data as seen in Fig. 2-5d, Fig. 2-5f and Fig. 2-5*l*. Further comparison of 1C, 2C and 3C laminates was used to show the effect of stacking sequence on strain maps observed on the surface of these sample. Since these three hybrid laminates have different stacking sequence but a similar carbon to glass fiber fraction, their damage progress under in plane loading was assumed to be analogous. As seen

in Fig. 2-5a, Fig. 2-5c and Fig. 2-5e at 5% shear strain level strain map between the notches for 1C was uniform, the same area for 3C sample showed several regions with high strain concentrations and the 2C laminate demonstrated an intermediate strain map distribution.
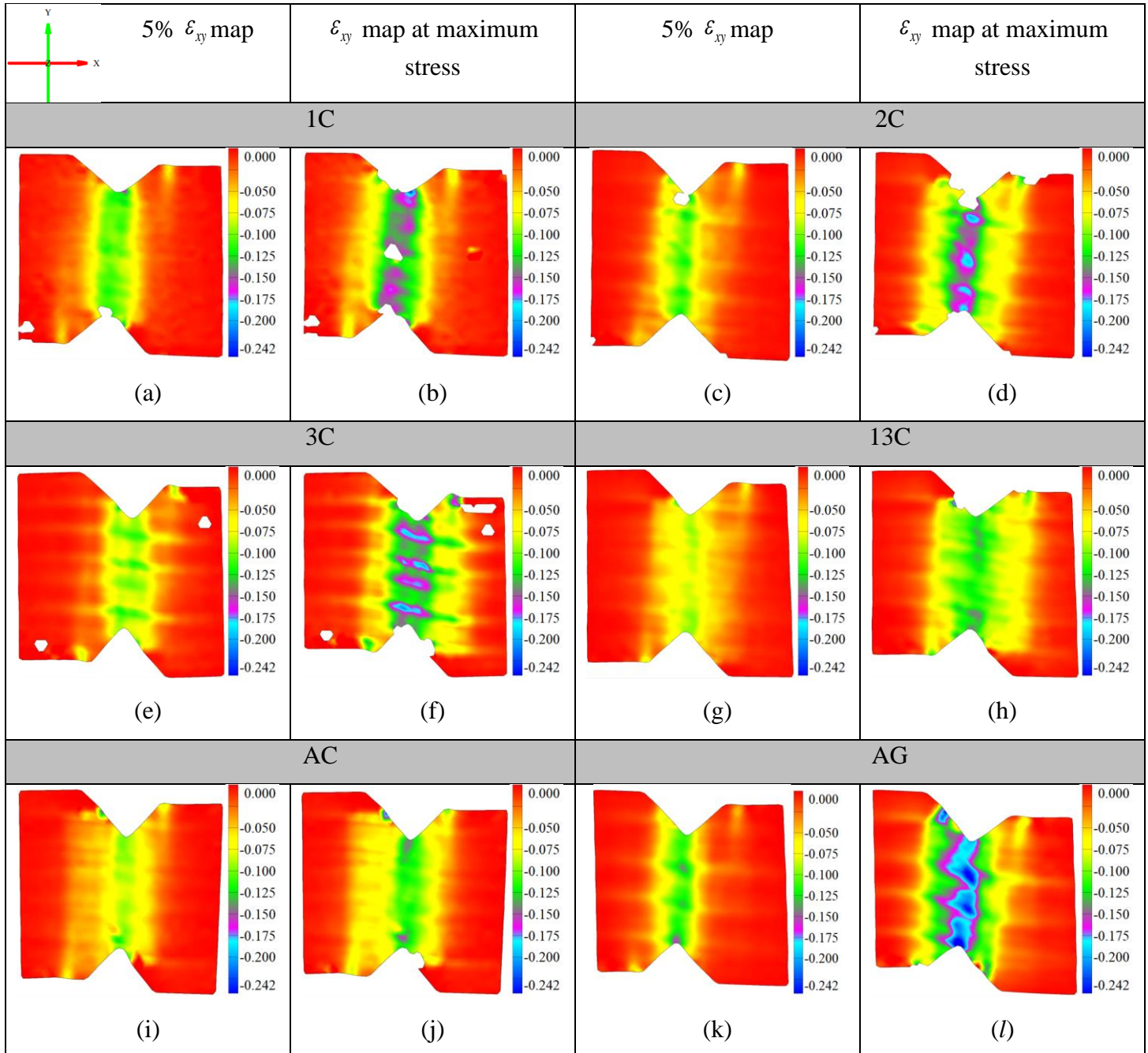


Fig. 2-5. strain maps for various laminates in $0^o$ direction at 5% $\varepsilon_{xy}$ strain and maximum load level

Since the bonding strength between the carbon fibers and the matrix material was superior as compared to the glass counterparts, it was plausible that at 5% shear strain micro damage development in transverse direction of 1C specimen was not as much of hybrid laminates with their glass plies at the surface, i.e. 2C and 3C. In other words, damage development rate was slower for 1C laminates due to better transfer of load between matrix and fibers. In short, the observations through DIC measurements indicated that stacking sequence of hybrid fiber laminates influenced the values of shear properties obtained from surface layers. Presence or absence of fibers with better interfacial property at the surface of hybrid laminate caused overestimation or underestimation of shear strain.

Fig. 2-6 shows the $\varepsilon_{xy}$ strain map for different laminates tested at 90$^o$ configurations, at maximum corresponding stress level. In all samples nonlinear behavior started as soon as the strain level at some areas in between the notches exceeded 0.02, i.e. $\gamma_{xy}$=0.04. These localized high shear strain regions started to grow in loading direction and coalesced to form a narrow shear band all between roots of the notches. It could be assumed that shear bands corresponded mainly to development of debonding between the matrix and fibers interface. As seen in Figs. 4-6a, Fig. 2-6b and Fig. 2-6c the maximum shear values reached to 0.24 between the notches for 1C, 2C and 3C laminates, respectively, and no significant difference in distribution of strain fields was observed. This result was contrary to the conclusion of shear tests in Fig. 2-5 where stacking sequence influenced the apparent distribution of shear strains between the notches. As seen in Fig.4-6d, the 13C sample presented two narrow bands with high shear strain concentration during loading which were indicated by two dashed ovals. One of the shear bands appeared earlier and developed further than the other one in length, therefore it caused global failure of sample when it reached to the roots of the notches. The reason behind second shear band seemed to be the formation of a vertical splitting at upper notch and crushing of the lower notch of the sample as indicated by dashed circles. Strain distribution of AC non-hybrid specimen in Fig. 2-6e showed a wide shear band in between notches with small shear strain values as compared to hybrid laminates, i.e. 1C, 2C and 3C. Shear strain map of this non-hybrid sample showed that shear load was distributed in bigger volume of material which could be due to higher interface strength between carbon fibers and matrix material. On the contrary, the

response of AG laminate was alike 1C, 2C and 3C samples, i.e. narrow shear band between the notches with akin strain values up to 0.3. High strain values in shear band for AG specimen could be related to lower interface strength for this sample which caused easier localization of shear stress and growth of a narrow band due to the micro damage accumulation. Overall, in plane shear response of hybrid fiber laminates in 90° configurations was mainly controlled by volume fraction of present fibers rather than stacking sequence. For 1C, 2C and 3C hybrid specimens which had higher content of the glass fiber as compared to the carbon fiber, shear response before failure was like AG laminate, i.e. narrow shear band throughout the between the notches. In contrast for 13C sample which had higher volume fraction of carbon fibers, the shear behavior was comparable to AC sample, which had wider shear strain bands and smaller strain values.
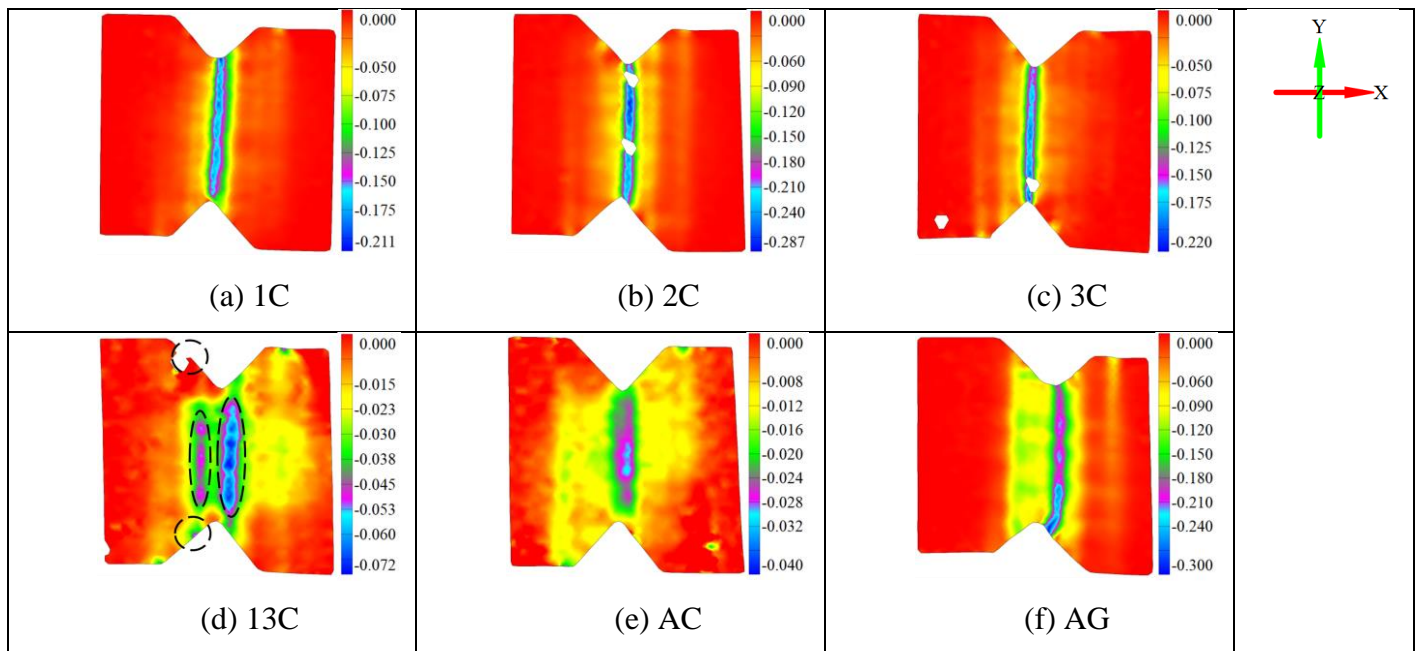


Fig. 2-6. DIC shear strain maps for 90° configurations for (a)1C, (b)2C, (c)3C, (d)13C, (e)AC, and (f)AG lamiantes

2.4 Conclusion

Nonlinear behavior of glass/carbon hybrid fiber reinforced laminates were studied under in-plane shear deformation and compared with non-hybrid laminates using V-notch shear test with

the help of DIC measurements. The effect of stacking sequence in different cases was studied and conclusions are made accordingly.

- Three different regions of interest (ROI) are defined for DIC analysis and their corresponding stress-strain curve was compared among themselves and with strain gauge data. The values of strain for ROI 3 perfectly matched with strain gauge data, however the strains obtained for ROI 1 show smaller values, respectively. This variation was correlated with inclusion of the regions with insignificant shear strain in calculation of the average shear strain which were out of notched region.

- It is suggested that ROI 2 provided better representation of shear behavior of composite material up to a point where damages were within the notched region of sample. For further development of failure beyond v-notch region, ROI 3 offered a better representation of materials behavior since it incorporated bigger sample volume in calculation. Thus, it is better to use small region of interest between the notches at the beginning of shear test in linear region, and a larger region of interest defined for nonlinear section of the stress-strain curve.

- The growth of damages in hybrid laminates tested in $0^o$ configuration showed that presence of carbon layers at the surface ply promoted a uniform strain distribution between the notches while samples with glass layer as top plies showed localized discrete sites of damage growth during shear loading. Therefore, using full field strain measurement method revealed the effect of stacking sequence on damage development pattern and enabled identification of the major damage growth locations in interply hybrid fiber laminate at any in-plane shear stress level.

- Remarkably, DIC results for samples tested in $90^o$ configuration showed that the strain maps observed during in-plane shear test of hybrid fiber laminates were dependent on the relative volume fraction of fibers rather than the stacking sequence of the layers with various stiffness. Moreover, abrupt failure of the samples in this direction revealed that highly concentrated strain regions observed in DIC strain maps were related to the sudden damage developments in fiber/matrix interface under shear stress between the notches.

**Paper 3.    Damage Growth and Failure Detection in Hybrid Composites**

**Using In-Situ Strain Measurements and Smoothing Element Analysis**

A novel damage monitoring approach is proposed for hybrid laminates by combining different strain measurement techniques with smoothing element analysis (SEA). This viable experimental procedure eliminates the effects of global/local nature of strain measurement systems on heterogenous damage accumulation and is a two-step approach. First, digital image correlation (DIC), strain gauges, FBG sensors, and infrared thermography are utilized concurrently to indicate the differences in the measured strains and monitor damage accumulation during a tensile test. This demonstrates how failure events disturb the measurement capabilities of each system, which can cause a miscalculation of hybrid effects in hybrid-fiber laminates. The second step involves the utilization of SEA algorithm for discretely measured DIC displacements to predict a realistic continuous displacement/strain map and rigorously mitigate the inherent noise of the DIC system. Remarkably, for large deformation states, SEA enables early prediction of susceptible damage zones at stress levels 30% below material strength.

Keywords: Hybrid Fiber Composites; Damage Progress Monitoring; Smoothing Element Analysis; Poisson's Ratio Reduction.

3.1 Introduction

Fiber reinforced polymeric composites are advanced structural materials with tailorable capabilities and functionalities. The anisotropic properties and higher strength to weight ratio as compared to their metallic counterparts makes fiber reinforced composites an attractive choice for many in various cutting-edge applications. Despite their intriguing nature, prediction and understanding of mechanisms involved in failure initiation, progress, and critical size of failure in fiber reinforced polymer matrix laminate is a very complex task due to presence of a multi-component material system. The difference in the mechanical properties of constituent materials result in non-uniform strain profile and localized strain gradient under different

loading conditions. The localized strain disparity and high strain gradients make fiber reinforced laminates prone to cracking in matrix or interface of matrix/fibers[96]. The growth or coalescence of these cracks would cause a global failure of fiber reinforced laminates which is usually abrupt and without any alert [97]. Therefore, monitoring strain evolution in fiber reinforced polymeric composites and hybrid material systems with higher strain gradients in their structure, bespeaks the importance of monitoring strain evolution and identifying the local and global strain gradients in composite materials.

Due to easier development of cracks under tensile loading condition, monitoring strain evolution under tensile loading is of a significant importance. The typical tools for strain measurement under tensile loading condition are mechanical extensometers which are easy to be mounted on the sample, however their accuracy and reliability can be of concern. Moreover, the mechanical extensometers are very delicate instruments and must be removed prior to global failure of the specimens. Specially in the case of fiber reinforced composites which show tense energy release at global failure point, so the extensometer shall be removed to prevent any possible damage. Another conventional strain measurement technique with higher accuracy involves usage of resistive strain gauges mounted/adhered on the surface of specimen. The resistive strain gauges are very sensitive to misalignment, weak adhesion to surface and electromagnetic noise at environment [98] which requires specific cautions in their adhesion and utilization. In addition, both mechanical extensometers and resistance strain gauges do suffer from inadequate spatial resolution and their limitations on measurement of global deformations [99].

Another method for strain measurements in fiber reinforced laminates is usage of embedded Fiber Bragg gratings (FBG) sensors inside the laminates. FBGs were introduced as results of a research by hill et al. [100] who found out that Ge doped glass fibers could preserve permanent gratings. Applying periodic grating can create a wavelength specific dielectric mirrors, which can reflect only a certain wavelength (Bragg Wavelength) out of a spectrum of light wavelengths. More over these fibers are capable of multiplexing and not vulnerable to interference of electromagnetic sources [101-104]. Considering the valuable advantages of FBGs, they have been extensively used in analysis of temperature, humidity, pressure and most importantly strain inside composite materials [105-109]. As strain is applied on composite

material, it causes an elastic deformation on embedded FBGs consequently changing Bragg wavelength of grating corresponding to the magnitude of strain. Bragg wavelength can be given as, $\lambda_B = 2n_{eff}\Lambda$ where $\Lambda$ is grating period and $n_{eff}$ is effective refractive index of fiber optic. Any change in bragg wavelength due to thermal and/or mechanical strains can be written as Eq. (1):

$$\frac{\Delta\lambda_B}{\lambda_B} = (1 - P_e)\Delta\varepsilon_{app} + (\alpha_f + \xi)\Delta T \tag{1}$$

Where $P_e$ is strain-optic coefficient of fiber, $\Delta\varepsilon_{app}$ is applied mechanical strain on fiber, $\alpha_f$ is thermal expansion coefficient of fiber, $\xi$ is thermo-optic coefficient of fiber and $\Delta T$ is the temperature variance during measurements. Since temperature does not change very significantly during conventional tensile tests, second term of above equation will be removed and change in Bragg wave length will be only a function of mechanical strain [110]. The FBG sensors provided the opportunity to embed sensors at various locations and between different layers of laminate and get an insight on strain profile through thickness of FRPCs at very localized regions. Kuang et al. [111] investigated strain values obtained from embedded FBG of various layups, their results indicated perfect correlation between strain gauge data and FBG strain in Unidirectional configuration while some incompliance was observed for angle ply specimens. Bosia et al. [112] measured the strain distribution through thickness of a cross ply laminates at customized three point bending tests. Their results showed that various span to depth ratios would cause linear to nonlinear distribution of strain specifically around load region. Emmons et al. [113] have found that high pressure exerted on specimen at grips area would result in wrong strain measurements by FBGs embedded in these locations. Wood et al. [114] have shown very good agreement between strain gauge and embedded FBG for unidirectional composite laminates except for high load values, which they have assumed to be due to compression of grips applied on specimen and fiber. Non-contact methods of strain measurement have been used in recent years since they do not interfere in mechanical response of material. These methods use optical techniques to measure surface of material during deformation and thus provide a full field monitoring capability. Among these methods the main ones are photo-elasticity, geometric moiré, moiré interferometry, holographic interferometry, speckle interferometry (ESPI), grid method and digital image correlation (DIC) [115]. DIC

technique is favored as compared to other methods since it provides measurements with least sensitivity to vibration and optics anomalies [96]. As the name implies DIC technique is based on an algorithm to correlate consecutive images taken during deformation. To do so a series of images are taken through imaging device (CCD cameras) during deformation of specimen under loading. Then a commercial software or in-house code in programming environment is used to implement the correlation algorithm on imported images from cameras. The algorithm identifies certain areas on the surface of material called subsets and follows those subsets according to a step size value for each pair of consecutive images. The results of these comparisons are compared with the image of the undeformed state of material prior to loading to indicate total displacements at each point on the surface of material. Software defines subsets through a stochastic pattern which is applied on the region of interest at the surface of the material. This stochastic pattern will create enough grayscale and contrast for software  to implement correlation algorithm accordingly [116]. While using one camera for DIC analysis gives the displacements on 2D surface, utilization of two cameras in stereo configuration would give monitoring of the out of plane displacements in spatial coordinates. Since composite materials possess anisotropic properties and contain various constituent, their deformation will not be as homogeneous as isotropic materials [7]. Using DIC method to monitor deformation of composite materials may give a very comprehensive result by indicating locations prone to damage development. Therefore, many investigators have used DIC for strain measurements of tensile composite specimen, for which some will be reported herein. Brunbauer et al. [117] performed quasi-static tensile tests on laminates of three different configurations. UD0°, UD45° and UD90°. They have found that tendency of 45° fibers to align with load direction could have caused extensometers in contact with specimen to follow fibers and thus give lower strain results compared to DIC technique. In a study conducted by Hoffman at al. [118] they used DIC measurement to show that quasi-static tests would result in bigger strain field in materials compared to high strain rate tests. In a recent study Oz et al. [119] used DIC along with acoustic emission analysis to correlate damage progress in quasi isotropic laminates with obtained acoustic emission clusters. They showed that DIC method was very successful in determining transverse crack and macro-delamination in fiber reinforced laminates. Despite all these efforts, random errors due to image noise and image contrast are inevitable for DIC system since it collects intensity data at discrete pixel subsets, [120]. These sources of noise are amplified while

obtaining the strain maps from displacement fields thereby causing inaccuracy in DIC measurement [121-123]. Therefore, Noise removal of DIC data has been conducted in several investigations by global or local algorithms such as Savitaky-Golay filters, Radial Basis Functions, Finite Element Methods, Hermit Element Methods, Spline Functions and Regularized Polynomial Smoothing Method [124-128]. Although comprehensive, the premise of these methods is merely dedicated to optical aspects of DIC, and no research uses a penalty term to enforce continuity and control curvature after implementation of smoothing algorithm. Hence, in present study smoothing element analysis (SEA), which was proposed by Tessler et al. [129] for accurate stress recovery in classical finite element analysis is utilized to remove the errors in DIC data. This method has shown potential to be combined for inverse finite element method (iFEM) [130-132] and structural health monitoring [62, 133] in composite structures. However, the ability of SEA to reconstruct full-field continuous strain maps from discretely collected displacement data for damaged structures has not been explored yet. Thus, for the first time the advantages of using SEA for smoothing DIC data is investigated besides damage analysis of fiber reinforced composites. This approach will include both nonhybrid and hybrid fiber reinforced laminates.

Hybrid fiber reinforced composites are laminates employing advantages of several fibers in a single matrix material. The basic advantage of hybrid fiber laminates is called hybrid effect which is directly related to strains measured under loading conditions, specifically significant in tension. Hybrid effect is the amount of increase in strain at failure (first stress drop at stress-strain curve) for a low elongation laminate (LE), such as carbon fiber reinforced laminate, which is obtained through substitution of some of its plies with high elongation (HE) fiber plies such as glass fiber reinforced lamina. [4, 134]. So, a hybrid laminate of glass/carbon fiber reinforced polymer under tensile loading will show initial stress drop at a higher strain as compared to a carbon fiber reinforced laminate. Since hybrid effect is a strain dependent parameter, using multi-instrument strain measurement methods for hybrid fiber laminates will be very advantageous in determining the validity of hybrid effect values. On the other hand, using multi-instrument strain measurement and structural health monitoring techniques (e.g. thermography) will provide details about failure progress in local and global scale for hybrid laminates. In a recent study Khan et al. [11] have used thermography besides strain measurement techniques to comprehensively analyze the failure progress in multi-directional

carbon fiber reinforced laminates. Alkhateab et al. [135] have highlighted the complementary effect of using thermal maps in enhancing the capability of failure detection and damage accumulation in laminated structures. Progressive failure in composite laminates can be evaluated through damage index parameters such as Poisson's ratio degradation[136-138]. Yilmaz et al [31] have shown that reduction in Poisson's ratio is directly related to stiffness reduction in composite materials and depends on number off axis plies in laminated composite materials. They have stated that increase in density of transverse cracks reduces transfer of axial loading to lateral direction, thus reducing Poisson's Ratio. Van Paepae et al. [139] showed that initial failure of $90°$ plies in $[0/90]_{2s}$ laminates was responsible for decrease of Poisson's ratio of orthotropic laminates under cyclic loadings. In an investigation conducted by Akay et al. [98] two embedded FBG sensors in axial and transverse direction in a composite laminate were used besides biaxial strain gauges. Poisson's ratio degradation during fatigue test was recorded which indicated weaker performance of resistive strain gauges in cyclic loading tests due to their breakage and loss of data over time as compared to embedded FBGs. Therefore, due to disadvantages of strain gauges, simultaneous usage of other strain measurement techniques such as Fiber bragg gratings and DIC will help to surpass mentioned problems and characterize progressive failure of composite laminates. Moreover, the Poisson's ratio degradation studies report results based on Biaxial or woven laminates in which transverse cracking is the common damage mode, thus very little data is available for unidirectional laminates. This can be attributed to the fact that transverse cracking is a better indicator of Poisson's ratio reduction and this type of failure occurs easily in biaxial and multiaxial laminated structures. So far, no study has been conducted to investigate variations in hybrid effect values stemmed from measurement technique of hybrid fiber laminates. Moreover, to the best of authors' knowledge no investigation has been conducted to analyze failure progress in unidirectional hybrid laminates with simultaneous usage of thermography, DIC and FBG sensors accompanied by monitoring the Poisson's ratio degradation obtained from full field strain measurements.

Considering the missing aspects in previous investigations discussed earlier about hybrid fiber laminates, current study is structured as follows. In the first part, details of materials and manufacturing procedure are presented followed by provision of specifications and preparation of strain and thermal measurement techniques, i.e. FBG data collection, strain gauge adhesion, thermal camera usage and DIC system calibration. To improve the results of DIC method, SEA

methodology utilized by authors is described in detail. In the second part, comparison of strains measured through different techniques under tensile loading condition is given and failure progress is analyzed with the help of full field strain and thermal maps. The advantages of SEA in damage analysis under tensile loading conditions is demonstrated. Then, the Poisson's ratio evolution is shown for each tested sample using data collected from DIC and strain gauge systems and the reasons for their difference is discussed. Finally, the concluding marks are given and the advantages of using multi-instrument approaches are briefed.

## 3.2 Materials and Experimental Procedure

### 3.2.1 Composite manufacturing

Unidirectional hybrid laminates of epoxy matrix composites were prepared in a symmetric configuration using 6 plies . Unidirectional glass fabric with aerial weight of $330g/cm^2$ (283 $g/m^2$-1200 Tex along the [0°] direction, 37 $g/m^2$-68 Tex E-Glass stitching fibers along the [90°] direction and stitch with $10g/m^2$ -76Dtex) and trade name of L300 E10B-0 were supplied from Metyx-Turkey. Unidirectional  carbon fabrics with aerial weight of $300g/cm^2$, density of $1.78g/cm^3$ and Tensile modulus of 240GPa were provided by Dowaksa -Turkey. Matrix material consisted of Araldite LY 564 resin and XB3403 Hardener purchased from Huntsman (USA) with mix ratio of 100g and 36g, respectively. The Tg of cured matrix was 70C. Two non-hybrid composites plates of carbon and glass fibers with [C/C/C]$_s$, [G/G/G]$_s$ configurations respectively and four glass/carbon fiber hybrid laminates, [C/G/C]$_s$, [C/G/G]$_s$, [G/C/G]$_s$, [G/G/C]$_s$ were prepared with size of 60×30 cm through vacuum assisted resin transfer molding (VARTM). The curing process was performed for 48 hours at $80°C$. The cured laminates with nominal thickness of about 1.8mm were cooled down slowly to prevent any possible deflection during demolding process. For easier reference, the nomenclature given at Fig. 5-1 was used for each stacking sequence of laminates.

### 3.2.2 Fiber Bragg grating placement and data collection

Due to their capability of non-invasive internal measurements, two single mode fiber optic gratings purchased from Technica were used with Bragg wavelengths of $\lambda_B$=1550nm and $\lambda_B$=1540nm. The gauge length for FBGs was 1mm with polyimide coating and strain optic coefficient of $p_e = 0.1667$. Grating position on the manufactured plate was marked before

impregnation of resin/epoxy to enable placement of sensors exactly at the middle of tensile specimen's gauge length. The FBG sensors were sew through stitches of dry fabrics to ensure their positional stability during resin epoxy impregnation. The plies which had FBG stitched to them were placed as 2nd and 3rd plies from surface as seen in Fig. 3-1. Response of FBG sensors was obtained through Micron Optics SM230 model interrogator with a sampling frequency of 1000 Hz and saved by Micron Optics Enlight Software.



| Layer Number | Orientation | AC | 13C | 1C | 2C | 3C | AG |
|---|---|---|---|---|---|---|---|
| 1 | 0° | Carbon | Carbon | Carbon | Glass | Glass | Glass |
| 2 | 0° | Carbon | Glass | Glass | Carbon | Glass | Glass |
| 3 | 0° | Carbon | Carbon | Glass | Glass | Carbon | Glass |
| 4 | 0° | Carbon | Carbon | Glass | Glass | Carbon | Glass |
| 5 | 0° | Carbon | Glass | Glass | Carbon | Glass | Glass |
| 6 | 0° | Carbon | Carbon | Carbon | Glass | Glass | Glass |
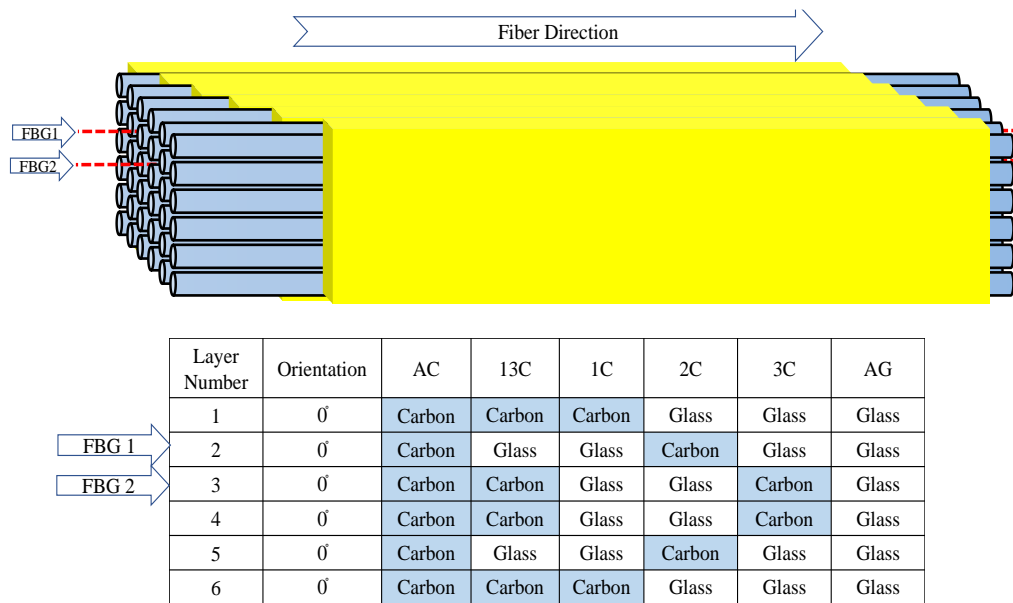
Fig. 3-1. Schematic of FBG positions and stacking sequence of various composites

3.2.3   Specimen preparation and strain gauges attachment

Tensile specimen were cut according to ASTM D3039, however as already devised by authors [110], an L-shaped specimen was prepared to enable the ingress of FBG sensors into the laminated specimen. Specimens were cut precisely to ensure that the position of  FBG sensors was just at the midpoint of the gauge area. Aluminum tabs plates were used to tab the specimens according to ASTM D3039 standard recommendation. The middle of gauge area which is consistent with the position of FBG sensors was marked and cleaned to adhere biaxial strain gauges on the surface of sample. Strain gauges were supplied from Vishay Group with nominal gauge factor of 2.16±1%. All tensile tests were conducted using Zwick Z100 universal testing machine and the test was set to 2mm/min speed in displacement control mode. The data

for strain gauges was collected through National Instruments NI SCXI1000 main chassis with a NI SCXI-1520 card at a sampling frequency of 100 Hz. To find out the repeatability of results, 4 other tensile samples from each laminate were cut according to ASTM D3039 and prepared. The results of these extra samples are given at previous work by authors [2].

### 3.2.4    Full Field measurements

Digital image correlation analysis 12M sensor system by GOM (Braunschweig-Germany) was used. Speckle pattern throughout the gauge length of specimen was created by black and white sprays as seen in Fig. 3-2. Speckle pattern was applied on the opposite surface of specimen where strain gauges were not mounted and DIC Sensors were calibrated in snap mode according to manufacturer's instruction based on a 250×200mm calibration object. The calibration results showed 0.023 pixels deviation for calibration and 0.001 mm for scale deviation which both were under maximum limits recommended by manufacturer of the system. To make sure that alignment of unidirectional specimens was in loading direction, reference measurements were taken by DIC in single image mode to check any displacement in through thickness (z) direction. This procedure avoided any bending or twisting of specimen and immature failure. Also, the speckle pattern quality was inspected by ARAMIS software before test initiation to ensure perfect surface contrast all over the gauge length. During the test camera had a working distance of 1250mm and angle between the cameras was 25 °. For post processing the recorded images through cameras subset size of 25×25 pixels with step size of 19×19 pixels were. GOM Inspect professional software was used to calculate the displacement fields along the gauge length and obtain longitudinal ($\varepsilon_{yy}$), transverse ($\varepsilon_{xx}$) and shear $\varepsilon_{xy}$ strain maps. For thermal monitoring of the samples under loading condition FLIR X6580sc camera was used with 50mm lens, Indium antimonide photon detector, thermal sensitivity of <25mK and radiometry range up to 300 ℃. Thermal data was collected at 10Hz frame rate and then processed by DisplayImg 6 software provided by edevis Gmbh. The schematic of multi-instrument test setup is depicted in Fig. 3-2.
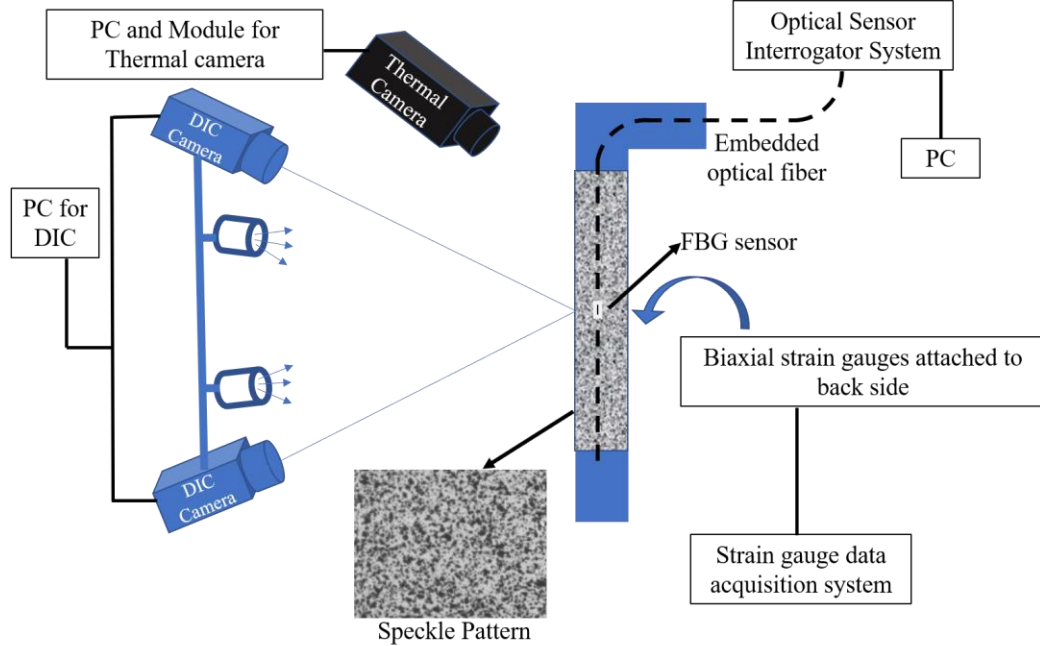
Fig. 3-2. Schematic of test set up for multi-instrument monitoring using DIC, Thermal Camera, Strain Gauge and embedded FBGs

### 3.2.5 Smoothing element analysis (SEA) for extrapolation of experimental DIC displacement and strain measurements

In a two-dimensional plane geometry, the discrete form of displacement data points obtained from DIC can be given as $\mathbf{u}_i \equiv \begin{bmatrix} (u_x)_i & (u_y)_i \end{bmatrix}^T$, where the subscript $i = 1, 2, ..., n$ indicates the transverse ($u_x$) and longitudinal ($u_y$) displacements measured at $n$ different locations. Here, the transverse and longitudinal directions are chosen as perpendicular and normal to the tensile loading direction, namely, aligned along the $x$ and $y$ axes of the tensile specimen, respectively. SEA can be implemented on these discrete displacement values to obtain a continuous experimental displacement distribution over the gauge length of tensile samples and calculate their associated derivates ($\frac{\partial u_x}{\partial x}, \frac{\partial u_y}{\partial y}$), representing the strains throughout the surface of material. The procedure of SEA generates $C^1$-continuous functions of the discrete experimental data which means that the first order derivatives of the displacements will be $C^0$-continuous. Therefore, such a computation through SEA can minimize the relative error of the strain reconstruction from the DIC displacements. Hence, the individually measured

91

displacements/strains over spatial coordinates can be shown as continuous functions which are well-defined everywhere over the gauge length of tensile specimens. Let's use $u_i^h$ symbol for discrete data points of experimentally obtained longitudinal or transverse displacements from DIC, e.g., $u_i^h \equiv (u_y)_i$ or $u_i^h \equiv (u_x)_i$ ($i = 1, 2, 3, ..., n$), whereas their continuous form predicted by using SEA can be shown as $u_i^h \rightarrow u(\mathbf{x}) \equiv u$ with $\mathbf{x} \equiv (x, y)$. For a single smoothing element, the penalized-discrete-least-squares error functional can be written as [129]:

$$
\Phi = \frac{1}{n} \sum_{i=1}^{n} \left( u(\mathbf{x}_i) - u_i^h \right)^2 + \alpha \int_S \left( \left( \frac{\partial u}{\partial x} - \varepsilon_1 \right)^2 + \left( \frac{\partial u}{\partial y} - \varepsilon_2 \right)^2 \right) dS
$$
$$
+ \beta S \int_S \left( \left( \frac{\partial \varepsilon_1}{\partial x} \right)^2 + \left( \frac{\partial \varepsilon_2}{\partial y} \right)^2 + \frac{1}{2} \left( \frac{\partial \varepsilon_1}{\partial y} + \frac{\partial \varepsilon_2}{\partial x} \right)^2 \right) dS
$$

(2)

where for point $\mathbf{x}_i$ the analytical counterpart of $u_i^h$ is shown by symbol $u(\mathbf{x}_i)$ and the area of the smoothing element is shown by the term $S$. The $\varepsilon_1 \equiv \varepsilon_1(\mathbf{x})$ and $\varepsilon_2 \equiv \varepsilon_2(\mathbf{x})$ are the analytical counterparts of the first-order derivatives of DIC strain data with respect to the in-plane coordinates of $x$ and $y$, respectively. The first term in Eq. (2) is the discrete least-squares functional that matches the smoothed displacement field and experimental displacement data. The second part of the Eq. (2) approximates the derivatives of the $u(\mathbf{x})$ displacement field to the relative analytical derivatives, $\varepsilon_1(\mathbf{x})$ and $\varepsilon_2(\mathbf{x})$. The errors of the spatial distribution for experimental displacement-derivatives (i.e., strains) are filtered by a curvature-control constraint as given in third term of the Eq. (2). The constraints level in the second and third terms of the Eq. (2) are enforced by two dimensionless parameters, namely, $\alpha$ and $\beta$. By proper selection of the $\alpha$ and $\beta$ parameters [129], the $C^1$-continiuty of the $u(\mathbf{x})$ distribution with $C^0$-continuous derivatives, $\varepsilon_i(\mathbf{x})$, can be readily achieved over the SEA domain. During the SEA simulations performed herein, these values are set to $\alpha = 1$ and $\beta = 10^{-4}$ for enforcing a rigorous smoothing condition.
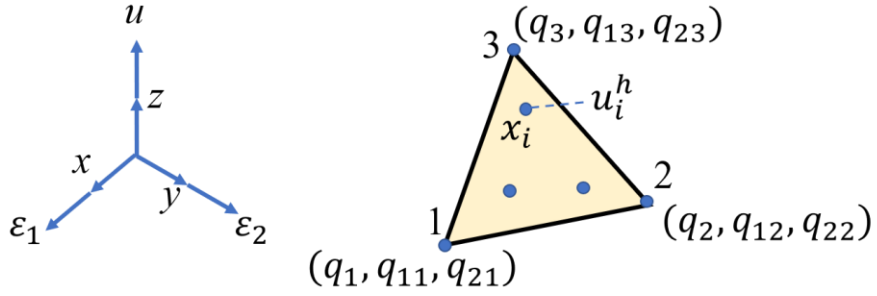
Fig. 3-3. A three-node triangular smoothing element depicted with its nodal DOF

Finite element interpolations are performed using a three-node triangular smoothing element as previously introduced in [129] to approximate the smoothed displacement data $u(\mathbf{x})$ and its respective analytical derivatives $\varepsilon_i(\mathbf{x})$, representing analytical strains. Hereafter the smoothed variables are defined as:

$$u(\mathbf{x}) = \sum_{i=1}^{3} \left( \xi_i(\mathbf{x})q_i + \zeta_{1i}(\mathbf{x})q_{1i} + \zeta_{2i}(\mathbf{x})q_{2i} \right) = \mathbf{N}\mathbf{q}^e \tag{3a}$$

$$\varepsilon_j(\mathbf{x}) = \sum_{i=1}^{3} \xi_i(\mathbf{x})q_{ji} \quad (j=1,2) \tag{3b}$$

where

$$\mathbf{q}^e = \begin{bmatrix} \mathbf{q}_1 & \mathbf{q}_2 & \mathbf{q}_3 \end{bmatrix}^{\mathrm{T}} \text{ and } \mathbf{q}_i = \begin{bmatrix} q_i & q_{1i} & q_{2i} \end{bmatrix} \ (i=1,2,3) \tag{3c}$$

$$\mathbf{N} = \begin{bmatrix} \mathbf{N}_1 & \mathbf{N}_2 & \mathbf{N}_3 \end{bmatrix}^{\mathrm{T}} \text{ and } \mathbf{N}_i = \begin{bmatrix} \xi_i & \zeta_{1i} & \zeta_{2i} \end{bmatrix} \ (i=1,2,3) \tag{3d}$$

where for each node depicted in Fig. 3-3 the vector $\mathbf{q}_i$ shows nodal degrees-of-freedom (DOF) for the smoothed displacements and their derivatives, and the linear and quadratic functions of the local coordinates of the element are given as vector $\mathbf{N}_i$. The $\mathrm{C}^0$-continuous area-parametric coordinates of a triangle are shown as $\xi_i$ functions defined explicitly as:

$$\xi_i = \frac{b_i\, x_1 + a_i\, x_2 + c_i}{2S} \quad (i=1,2,3) \tag{4a}$$

with auxiliary terms given as:

$$a_i = x_{1k} - x_{1j}, \ b_i = x_{2j} - x_{2k}, \ c_i = x_{1j}x_{2k} - x_{1k}x_{2j} \quad (i = 1,2,3; \ j = 2,3,1; \ k = 3,1,2) \tag{4b}$$

and the area of the triangular element calculated as:

$$S = \frac{1}{2}(a_3 b_2 - a_2 b_3) \tag{4c}$$

On the other hand, the $C^1$-continuous anisoparametric shape functions namely $\zeta_{1i}$ and $\zeta_{2i}$, are originally obtained for triangular element, MIN3 [140]. By applying area-parametric coordinates, the anisoparametric shape functions are defined as:

$$\zeta_{1i} = \frac{\xi_i}{2}\left(a_k \xi_j - a_j \xi_k\right) \text{ and } \zeta_{2i} = \frac{\xi_i}{2}(b_j \xi_k - b_k \xi_j) \quad (i = 1,2,3; \ j = 2,3,1; \ k = 3,1,2) \tag{5}$$

By substituting Eq. (3) into Eq. (2) and minimizing with respect to the unknown nodal DOF of the smoothing element, $\mathbf{q}^e$, final equations will be obtained as:

$$\frac{\partial \Phi(\mathbf{q}^e)}{\mathbf{q}^e} = 0 \Rightarrow \mathbf{A}^e \mathbf{q}^e = \mathbf{H}^e \tag{6}$$

where the vector $\mathbf{H}^e$ is a function of DIC displacement data as:

$$\mathbf{H}^e = \frac{1}{n}\sum_{i=1}^{n}\left[\left(\mathbf{N}(\mathbf{x}_i)\right)^{\mathrm{T}} u_i^h\right] \tag{7}$$

where the matrix $\mathbf{H}^e$ contains the squared terms of shape functions calculated at experimentally obtained strain positions, $\mathbf{x}_i$, and it also includes the squared first order derivatives of the shape functions as:

$$\mathbf{A}^e = \frac{1}{n}\sum_{i=1}^{n}\left[\left(\mathbf{N}(\mathbf{x}_i)\right)^{\mathrm{T}} \mathbf{N}(\mathbf{x}_i)\right] + \alpha \int_S \mathbf{B}_\alpha^{\mathrm{T}} \mathbf{B}_\alpha dS + \beta S \int_S \mathbf{B}_\beta^{\mathrm{T}} \mathbf{D}_\beta \mathbf{B}_\beta dS \tag{8a}$$

with

$$\mathbf{D}_\beta = \begin{bmatrix} 1 & 0 & 0 \\ 0 & 1 & 0 \\ 0 & 0 & 0.5 \end{bmatrix} \text{ and } \mathbf{B}_\chi = \begin{bmatrix} \mathbf{B}_\chi^1 & \mathbf{B}_\chi^2 & \mathbf{B}_\chi^3 \end{bmatrix}^{\mathrm{T}} \ (\chi = \alpha, \beta) \tag{8b}$$

and

$$\mathbf{B}^i_\alpha = \begin{bmatrix} \xi_{i,1} & \zeta_{1i,1} - \xi_i & \zeta_{2i,1} \\ \xi_{i,2} & \zeta_{1i,2} & \zeta_{2i,2} - \xi_i \end{bmatrix}, \quad \mathbf{B}^i_\beta = \begin{bmatrix} 0 & \xi_{i,1} & 0 \\ 0 & 0 & \xi_{i,2} \\ 0 & \xi_{i,2} & \xi_{i,1} \end{bmatrix} \quad (i = 1, 2, 3) \tag{8c}$$

The $\mathbf{A}^e$ matrix is not ill-posed for non-zero positive values of dimensionless parameter and it is a symmetrically banded square matrix. Hence, the solution of Eq. (6) can be readily obtained for an individual smoothing element. Since several smoothing elements are used to discretize the domain of a plate, a global matrix-vector form exploiting the connectivity of the elements must be created to contain the system of the equations of each single element. This system of global equations is solved by inverting the left-hand-side of the equation followed by multiplication of the inverse matrix with the right-hand-side vector, thereby resulting in the solution of the all unknown nodal DOF for the smoothing discretization. Once the nodal DOFs are predicted, they can be substituted in Eq. (3a) to compute smooth displacements. Besides, they can be used in Eq. (3b) for computing smooth strains. For instance, if the longitudinal displacements obtained from DIC ($u_i^h \equiv (u_y)_i$ ) are smoothed through SEA, then the analytical terms $u(\mathbf{x})$ and $\varepsilon_2(\mathbf{x})$ will correspond to the smooth longitudinal displacements and strains, $u_y(\mathbf{x})$ and $\frac{\partial u_y}{\partial y} \equiv \varepsilon_{yy}$, in the given order. Overall, one can exactly reconstruct the smooth strains from DIC displacements by implementing the SEA mathematical formulation provided in this section, thereby attaining a more accurate spatial variability of the DIC strains.

## 3.3 Results and discussion

### 3.3.1 Dependence of hybrid effect on measurement technique

The failure strain (final major stress drop in stress-strain curve) of each laminate is given based on used strain measurement techniques in Table 3-1. Since the glass fibers have higher elongation as compared to carbon counterparts, the highest average value for failure strain is related to AG sample whereas the lowest average failure strain is corresponding to AC specimen. Unfortunately, the outer FBG sensors in AC and 2C laminated configurations failed prior to test initiation, which is believed to be related to an early damage occurrence at ingress

95

region of optical fiber under exerted pressure by the grips of tensile machine. In this regard, Emmons et. al. [113] have also shown that exposure to high compressive stresses can hinder performance of FBG strain sensors. A preliminary comparison of failure strains obtained from various techniques reveals the discrepancy of failure points for each laminate, e.g. there is a difference up to 4000με for AG laminate, which indicates requirement for a quantitative method to better understand the disparity of data for each laminate. A valuable tool to achieve this goal is calculating the *Relative standard deviation (RSD)* which according to its definition specifies whether the standard deviation of a measured data is small or large as compared to absolute average value of the same data set. As seen in Table 3-1 the RSD for AG laminate is 12.31%, which indicates high discrepancy in failure points measured by various methods for this composite material. On the other hand, Due to abrupt failure development in AC laminate the RSD value drops to 4.83% indicating a smaller data scatter for this non-hybrid laminate. Comparison of average failure strains and RSD values for hybrid samples, i.e. 1C, 2C, 3C and 13C, reveals that the last configuration has the lowest average failure strain despite possessing the highest scatter in data among hybrid specimens. Such a high scatter in data for 13C sample, which has the highest volume fraction of carbon fibers among hybrid fiber composites and is expected to have lowest hybrid effect value as compared to the rest of hybrid composites, might actually possess higher hybrid effect value due to high variation in measured failure strain data. Therefore, providing a true hybrid effect value becomes even more challenging task, and as already signified in [3], accurate determination of baseline failure for carbon layers and its thickness are essential for calculation of hybrid effect in hybrid laminates. Hence, the failure strain results given in Table 3-1 suggest that the exact calculation of hybrid effect based on Eq. 2, will depend on the used strain measurement technique. In hybrid effect calculation according to Eq. 2, the term $\varepsilon_{f-HC}$ is the strain corresponding to the earliest stress drop in the stress-strain curve of hybrid composite and $\varepsilon_{f-LEL}$ is the ultimate failure strain of low elongation laminate (AC sample in this study).

$$\% \, \text{Hybrid Effect} = 100 \times \left( \varepsilon_{f-HC} - \varepsilon_{f-LEL} \right) / \varepsilon_{f-LEL} \tag{9}$$

Since several measurement techniques are involved in current investigation three paths can be taken to obtain the hybrid effect, which are either through consideration of a particular strain

measurement technique or averaging all methods. The first approach would be to utilize the average failure strain of the AC laminate as the baseline value, i.e. $\varepsilon_{f-LEL} = \mathrm{mean}(\varepsilon_{f-AC}^{\mathrm{DIC}} + \varepsilon_{f-AC}^{\mathrm{FBG}} + \varepsilon_{f-AC}^{\mathrm{Strain\ gauge}}) = 9400\mu\varepsilon$ and then use it with the obtained failure strains for hybrid laminates according to different measurement techniques. In the second method, the failure strains acquired only through a single measurement technique are utilized to determine the value of hybrid effect, e.g. to calculate hybrid effect of 13C laminate through DIC, $\varepsilon_{f-13C}^{\mathrm{DIC}}$ and $\varepsilon_{f-AC}^{\mathrm{DIC}}$ are employed in Eq.9. For the third calculation scheme, the average values of failure strain for AC and hybrid laminate are used directly in Eq.2 regardless of the strain measurement technique. The results of these calculations are presented in Table 3-2.

Table 3-1 Failure Strains of each laminate measured by different methods

| Laminate | | AC | AG | 13C | 1C | 2C | 3C |
|---|---|---|---|---|---|---|---|
| Failure Strain (με) | DIC | 9300 | 20400 | 13100 | 14000 | 13800 | 12800 |
| | Outer FBG | N/A | 16000 | 14100 | 15200 | N/A | 13600 |
| | Inner FBG | 10000 | 15100 | 14100 | 14000 | 14300 | 5400 |
| | Strain Gauge | 8900 | 19100 | 11300 | 14000 | 13000 | 12500 |
| Average(με) | | 9400 | 17650 | 13150 | 14300 | 13700 | 12967 |
| Relative standard deviation (%) | | 4.83 | 12.31 | 8.69 | 3.63 | 3.91 | 3.58 |

Table 3-2. Hybrid effect value calculated for various laminates

| Hybrid effect calculation method | (1) Average failure strain of AC laminate | | | (2) Strain measurement technique | | | (3) Average of each laminate |
|---|---|---|---|---|---|---|---|
| Laminate | DIC | Inner FBG | Strain Gauge | DIC | Inner FBG | Strain Gauge | |
| 13C | 39.36 | 50 | 20.21 | 40.86 | 41 | 26.97 | 39.89 |
| 1C | 48.94 | 61.7 | 48.94 | 50.54 | 52 | 57.30 | 52.13 |
| 2C | 46.81 | 52.13 | 38.30 | 48.39 | 43 | 46.07 | 45.74 |
| 3C | 36.17 | -42.55 | 32.98 | 37.63 | -46 | 40.45 | 37.95 |

The negative hybrid effect of inner FBG for 3C specimen is related to the early failure of the fiber optic during tensile test which causes usage of a very low value for failure strain of hybrid laminate. Comparison of the results in Table 3-2 reveals that the hybrid effect decreases for 1C, 2C and 3C specimens, respectively, regardless of the hybrid effect calculation method. Higher hybrid effect value of 1C sample as compared to 3C laminate reveals that unlike recent investigations [3, 141, 142] which are focused on hybrid effect analysis of laminates with LE plies placed in between HE layers, it is possible to achieve similar positive hybrid effects with inverse stacking configuration. Besides, a significant difference between hybrid effect values obtained through strain gauge and other methods is observed for 13C laminate, thereby implying the underestimation of the mechanical response for hybrid laminate. In other words when the strain gauges are the only method for calculation of the hybrid effect of 13C specimen, the values of hybrid effect are undervalued despite presence of a higher value according to other strain measurement technique. Thus, one can deduce that usage of multiple strain measurement techniques has prevented miscalculation of hybrid effect. The maximum values of hybrid effect obtained through various calculation methods for each laminate is underlined in Table 3-2. Remarkably, the maximum values based on first calculation method are obtained when inner FBG is used to get the failure strain of a hybrid sample. This result is predictable since according to Table1 highest values of failure strain are related to FBG measurements. However, using second method of hybrid effect calculation shows that maximum values are no more attributed to inner FBG and other methods can also correspond to highest hybrid effect for each laminate. This uncertainty in true value of hybrid effect is directly related to damage development inside the laminate and its effect on strain measurement technique, thereby requiring a comprehensive analysis of stress-strain curve using global strain measurement method and non-destructive evaluation techniques such as thermal imaging.

### 3.3.2 Damage induced change in the slope of stress-strain curves

Fig. 3-4a to Fig. 3-4f present the tensile stress-strain curves of each laminate separately based on different strain measurement techniques, i.e. DIC, FBGs and resistive strain gauges. Correlating the variation of strain in each curve with full field measurements of DIC and thermal maps can elucidate the reason for uncertainties in the calculation of hybrid effects as per previous section, and also give information about the failure progress in each laminate. As seen

98

in Fig. 3-4a for non-hybrid samples, i.e. AC, stress-strain curves obtained from different strain measurement techniques display consistency in the slope of the curves up to about 3000με. However, at higher stress levels the slopes of various curves for this non-hybrid laminate become significantly different and inconsistency reaches to maximum level at failure point. Remarkably, such a difference for slopes of stress-strain curves begin to diverge at very small stress levels for other samples, e.g. the slopes of curves based on strain gauge for 13C and 1C specimen show vivid difference as compared to those of FGBs and DIC from the early stages of the test. Variation of slope in stress-strain curve is related to damage accumulation and consequent stiffness reduction inside the laminate [10, 135], and depending on the size of the damage inside the composite its influence zone will vary. According to global load sharing model [143] at locations far enough from the failure region (break influence zone) stress levels will be equal to the nominal level of stress in the test specimen, thereby it can be said that local strain measurements might not be influenced by damages occurring far away from them. Hence, various slopes of stress-strain curve seen in Fig. 3-4can be attributed to the fact that damage accumulation development at each layer is different and their influence zone is not large enough so that its effect can be captured through all measurement systems. Having said that, comparison of full field strain and thermal maps must reveal development of failure at some point which do not show any anomalies in local strain measurement techniques, i.e. FBG and strain gauges. Therefore, in the coming paragraphs stress strain curves of each laminate will be correlated with their full field strain and thermal maps to determine the failure progress and verify the complementary effect of using several structural health monitoring systems in miscalculation of hybrid effect.

As seen in Fig. 3-4a, regardless of the strain measurement technique the stress strain curves for AC laminate are very similar, and difference emerges at final stages of the test prior to failure point. At stress level equal to 1130 MPa which corresponds to about 8000 με, an instability is observed in the measurements of DIC method, which has been depicted as an inset figure in Fig. 3-4a. Despite presence of this hasty variation in DIC strains, no significant disparity in other strain measurement techniques, i.e. Inner FBG and Strain gauge is observed. This observation verifies above-mentioned statement regarding influence size of the failure which does not affect the relatively far regions inside the laminate and is not sensed by local strain measurement systems . To find the source of this discrepancy, DIC images of the sample

just before and after creation of this behavior are presented in Fig. 3-5a and Fig. 3-5b, respectively. Axial strain ($\varepsilon_{yy}$) maps throughout the gauge length at this specific moment of the test reveal a small area with high strain gradient at right edge encircled in dashed line. This region is correlated with high stress concentration which results in initiation of catastrophic edge splitting of the specimen i.e. shear failure of the matrix. It should be noted that, this failure is not considered as a premature lateral failure since it does not develop to tabbed region of the tensile sample [144]. As seen in thermal map of AC sample in Fig. 3-5c, at the same moment temperature rises at failure region due to release of energy. It must be noted that despite significant size of the failure region, embedded FBG and mounted strain gauge at the opposite surface of the laminate are not able to reveal this failure as shown at inset figure of Fig. 3-4a. This observation implies that using failure strain of sample according to DIC or correlated thermal image can provide actual value of $\varepsilon_{f-AC}$ for hybrid effect calculation of interply hybrid fiber laminates.

(a) AC

(b) 13C

(c) 1C

(d) 2C

(e) 3C                                              (f) AG
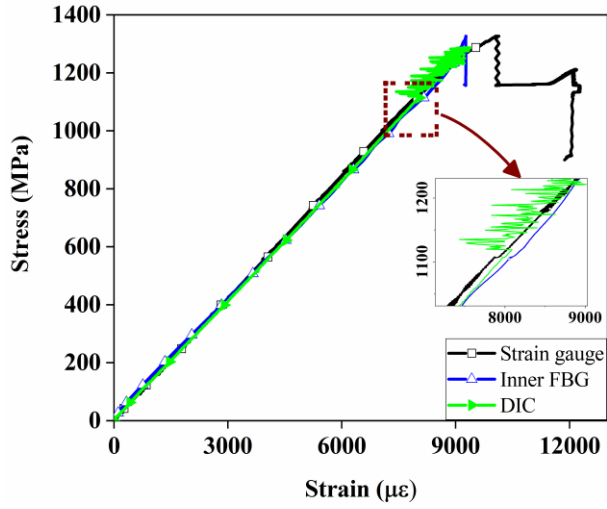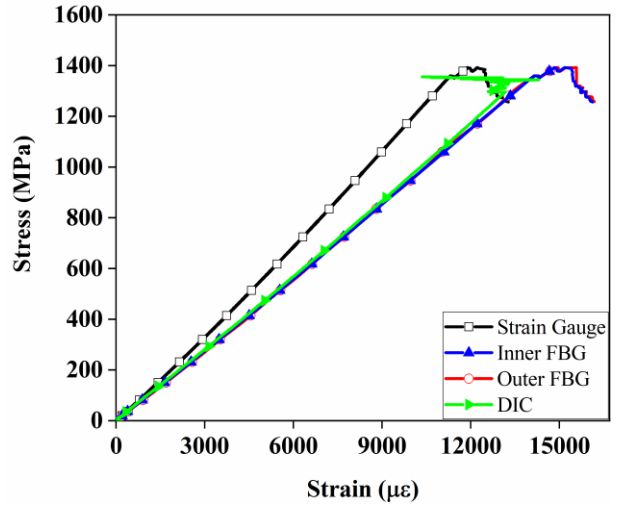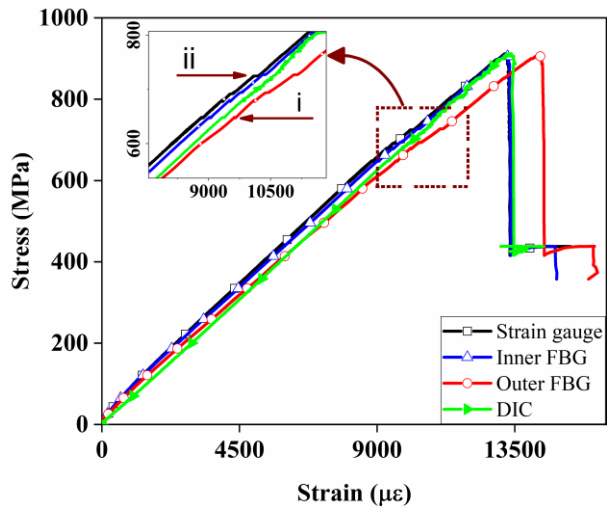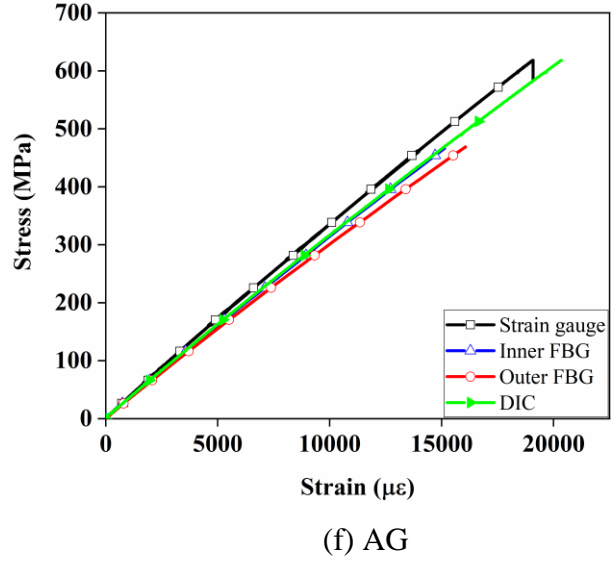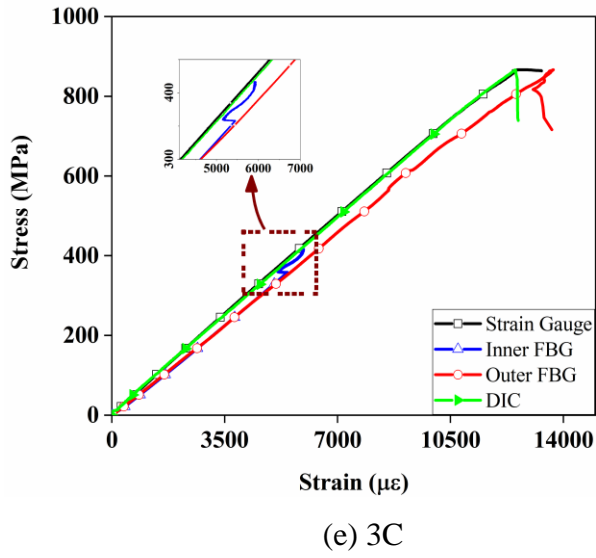
Fig. 3-4. Stress-strain curves for (a) AC, (b) 13C, (c)1C, (d)2C, (e)3C and (f)AG samples



(a) 1118 MPa   (b) 1120 MPa                    (c) 1120 MPa

Fig. 3-5. Axial Strain field for AC specimen at (a) 1118 and (b)1120 MPa; (c) Thermal map prior to failure at 1120 MPa
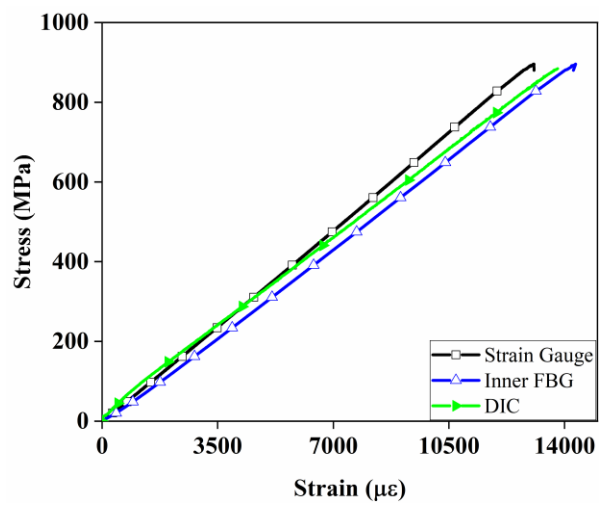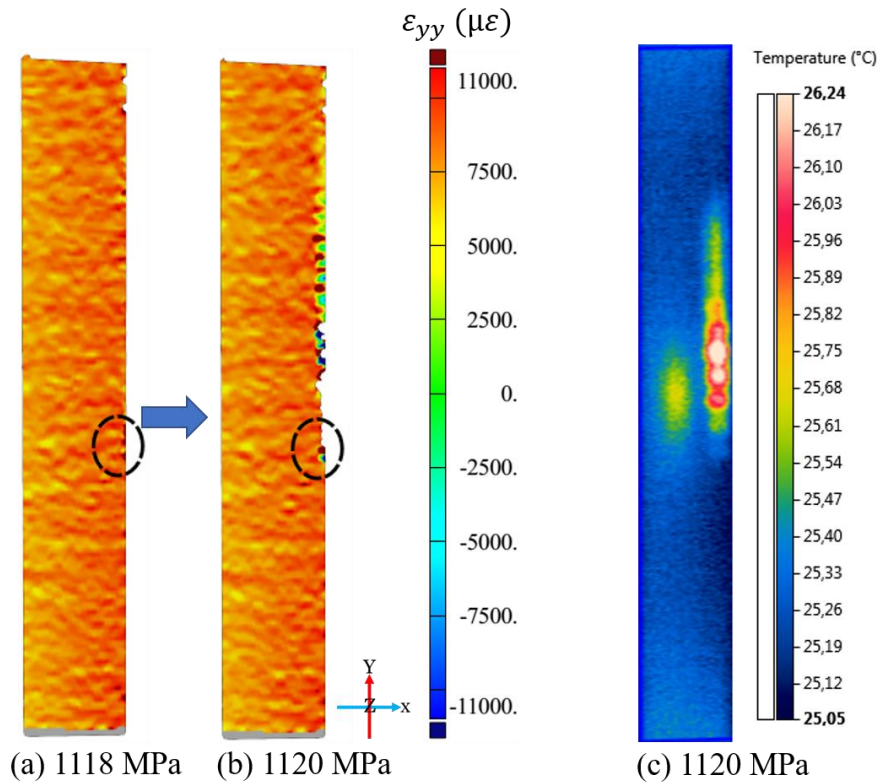
Fig. 3-4b presents the stress-strain curves for 13C sample, where a significant difference of about 2800με is seen between the failure points measured by strain gauges and FBGs. The reason for very low strains measured by strain gauges as compared to other methods can be attributed to technical, test setup and/or failure mechanisms. First reason might be the misalignment between strain gauge and loading direction. However, this conjecture is improbable due the correct placement and adhesion of strain gauge to specimen surfaces. The second speculation is misalignment between unidirectional fibers in laminate and loading direction which according to Ajovalasit et al. causes anomalies in nondimensional elastic constants such as $\vartheta_{12}$ [145]. As will be demonstrated in the coming section 13C laminate does not show any aberrant value of Poisson's ratio, therefore the effect of off-axis fibers is discerned. On the other hand, a possible reason for deviation of stress strain curves can be the independent development of failures at surface and inner plies of the laminate. To illustrate this issue, DIC and thermal maps for 13C specimen are compared at first major failure development in Fig. 3-6. As seen in Fig. 5-5a, at stress level of 1130MPa a small high strain gradient appears at left edge of the sample which indicates possibility of major failure development from this location. However, the thermal map at this stress level does not show any significant increase of temperature corresponding to the same location. Remarkably at about 1300MPa sudden damage develops at opposite edge of the specimen and splitting at right edge is clearly detected by DIC Map of Fig. 3-6b and thermal image of Fig. 3-6c. This failure instant is corresponding to start of hasty variation in strains recorded by DIC as observed in Fig. 3b, however, the FBG sensors and the strain gauge do not log any strain anomalies till development of the failure at left edge as shown in Fig. 3-6d. Hence it is seen that despite major failure development in Fig. 3-6b, strain gauge is not affected. Similarly, it can be said that gradual accumulation of micro damages inside the laminate causes reduction of stiffness according to FBG sensors and DIC measurements whereas strain gauge is not detecting damage accumulation effectively.

Fig. 3-4c demonstrates the strain measurements for 1C hybrid laminate, good consistency between the strain values obtained through different methods is observed up to 650 MPa. As shown in the inset Figure of Fig. 3-4c at 650 MPa a small step indicated as (i) is observed in the measurements. Unlike previous specimens this sudden variation of strain does not reveal any significant region with high gradient of axial strain ($\varepsilon_{yy}$) in the relevant full field map. On

the contrary, a high shear strain ($\varepsilon_{xy}$) gradient region appears at the left edge of the laminate as encircled in Fig. 5-6a and results in consequent edge splitting. The edge splitting is also recorded simultaneously in the pertinent thermal map of Fig. 3-7b and it is clear that thermal map gives a better intuition about the actual size of this failure. The other small step in strain values is observed at 720 MPa, which is indicated as (ii) in the inset Figure of Fig. 3-4c. Remarkably, this jump of strain does not reveal any significant strain gradient observable in full field strain maps, and only a small region with thermal activity as encircled in Fig. 3-7c is observed. This thermal activity is most likely associated with development of an internal damage at inner glass layers of the 1C laminate which does not affect the surface ply of the specimen significantly. On the contrary this damage influences the measurements of outer FBG and changes the slope of stress strain curve related with this measurement system. Thus, it can be concluded that failure development from HE plies to LE layers in hybrid specimens might be constrained.



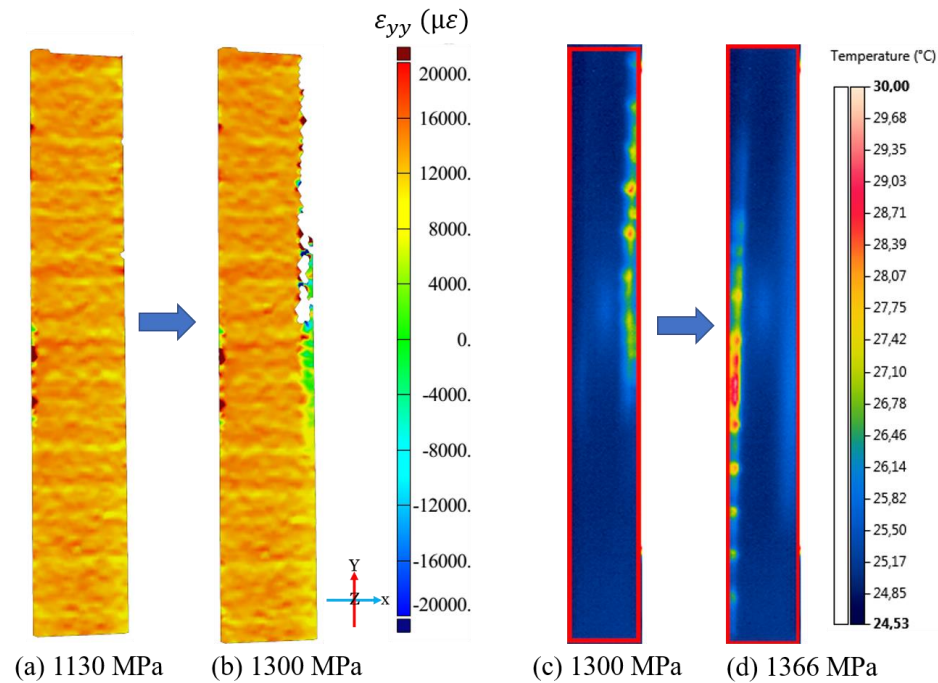(a) 1130 MPa    (b) 1300 MPa          (c) 1300 MPa    (d) 1366 MPa

Fig. 3-6. Axial strain maps for 13C sample at (a) 1130, and (b) 1300 MPa; Thermal maps corresponding to (c) 1300, and (d) 1366 MPa
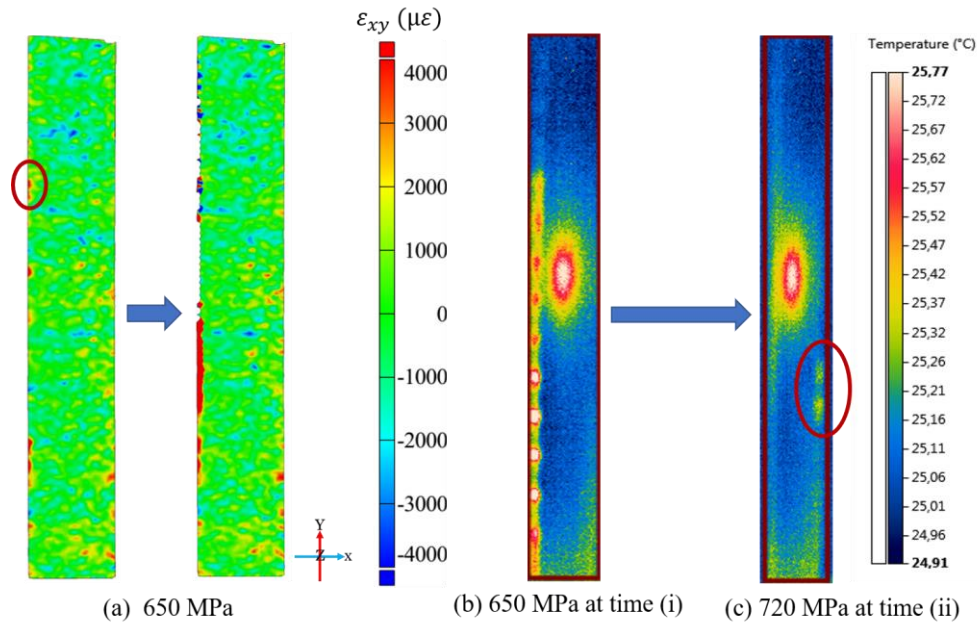
Fig. 3-7. (a) Axial strain maps for 1C sample at 650 MPa; Thermal maps corresponding to (b) 650, and (c) 720 MPa

Fig. 3-4d corresponds to strain measurements of 2C specimen. No data has been acquired through outer FBG sensor which indicates that its optical fiber has been damaged prior to initiation of the mechanical loading due to pressure exerted by jaws of the UTM instrument, similar to AC laminate. From the low stress levels discrepancy in the strain values obtained through various methods is observed. The difference becomes larger as the applied load on the laminated sample increases and reaches to its maximum at failure point, 896 MPa. Since carbon plies of the hybrid laminate possess higher elastic modulus as compared to their glass counter parts, major stress is carried by them and they transfer the load to glass plies after failure either through pseudo-ductility or catastrophic interlaminar delamination[4]. According to previous investigation by authors[2] interlaminar delamination is observed in broken 2C hybrid samples. Axial strain map of DIC measurements for the same laminate prior to catastrophic failure are given in Fig. 3-8a, where a high gradient strain field at top left edge of the specimen is observed. Despite presence of this susceptible failure area, no edge splitting occurs at that region and as seen in thermal image of Fig. 3-8b damage develops from the top middle location test coupon. This failure results in severe interlaminar delamination and fiber breakage as seen in Fig. 3-8b. Since the damage development in thermal map does not affect the surface ply which is

monitored by DIC, it can be implied that failure initiates from inner carbon layers and then develops to surface plies. This statement is also reinforced by the fact that strain values of the surface for 2C sample prior to catastrophic failure are between 8000με and 13000με. This range is well below the failure strain of AG laminates as shown in Table 3-1, and at the same time above the failure strain range for AC laminate as seen in Fig. 3-5a.
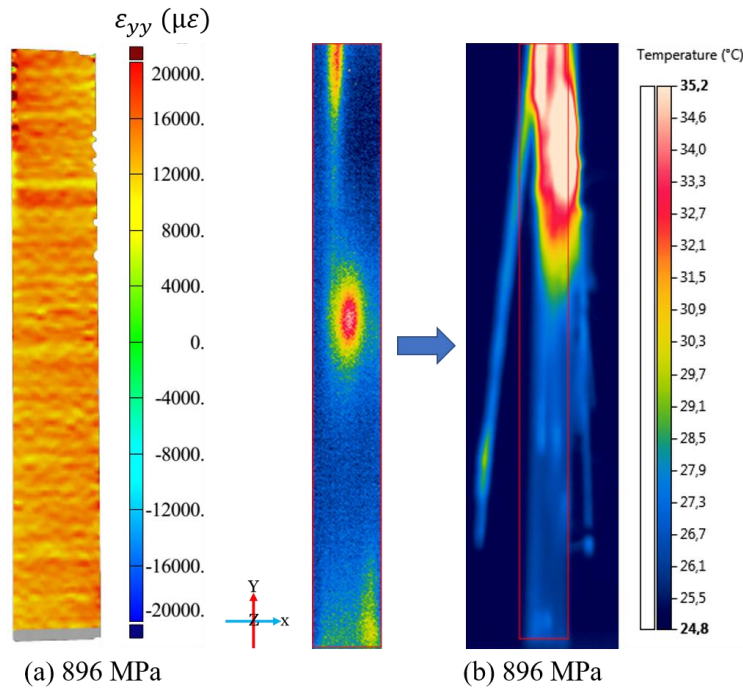


(a) 896 MPa      (b) 896 MPa

Fig. 3-8. (a) Axial strain map for 2C sample at 896 MPa; (b) Thermal maps at failure point corresponding to 896 MPa

Fig. 3-4e represents the stress-strain measurements for 3C hybrid laminate. As seen from the early stages of the test, strain values collected from surface layers are slightly less than those of embedded FBG sensors. This difference in the strain values becomes larger at higher stress levels and reaches to its maximum at failure point. As seen in Fig. 3-4e, the inner FBG sensor located between carbon plies of 3C laminate shows signal loss at stress level of 416MPa corresponding to strain of 5900με. This level of stress is below the failure stresses of both glass and carbon laminates, moreover, the thermal and DIC maps corresponding to this stress level do not show any anomaly to imply a major damage throughout the gauge length of tensile

sample. Thus, the failure of inner FBG is related to possible breakage of embedded fiber optic under the pressure exerted by UTM jaws at tabbed region of the tensile sample. The first major failure in 3C specimen occurs at 760MPa as seen in the thermal map of Fig. 3-9a. Microscopic analysis of the edge of sample reveals that this failure is interlaminar delamination as seen in Fig. 3-10, and no major failure at carbon plies has occurred. As shown in axial strain map of Fig. 3-9b for 866MPa, the interlaminar delamination (region I) has developed towards lower tab and there is a sudden change in strain gradient at lower left region of the sample indicated as Region II. Microscopic analysis of the edge of broken 3C laminate at region II, shows that the interlaminar delamination has shifted to inner carbon plies and caused failure in these layers. Damage of inner carbon plies is followed by global failure of the sample as depicted in thermal image of Fig. 3-9c. Therefore, full field monitoring of this sample accompanied by microscopic analysis reveals that failure of 3C hybrid laminate initiates by interlaminar delamination rather than breakage of carbon layers as seen in 2C hybrid specimen.



(a) 760 MPa          (b) 866 MPa          (c) 866 MPa
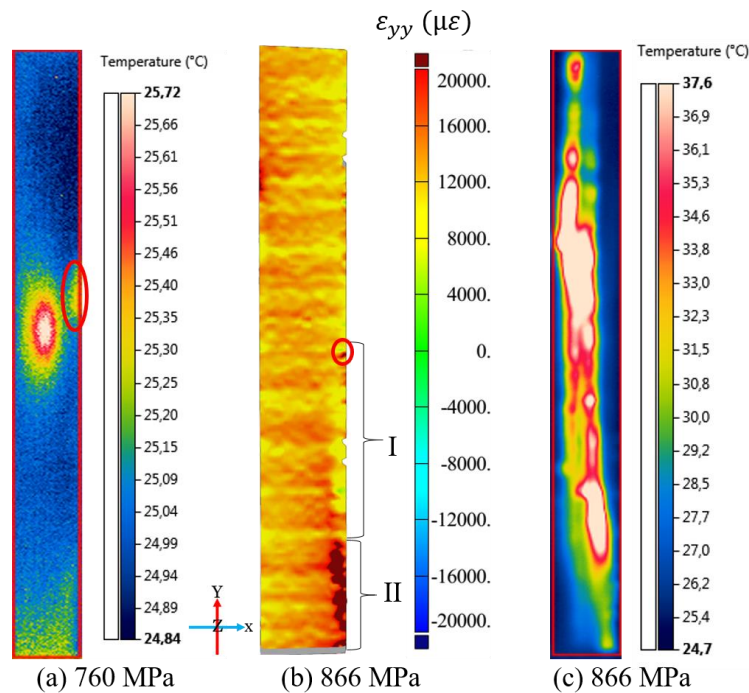
Fig. 3-9. (a)Thermal map corresponding to 760 MPa; (b)Axial strain map at 866MPa, and (c) thermal maps at 866MPa, for 3C laminate

Fig. 3-4f shows the stress strain curves for AG laminate obtained from different strain measurement techniques. Although a apparent consistency between the strain values is observed at early stages of loading, deviation between stress strain behavior becomes visible at high stress levels and reaches to maximum at global failure point of the sample. FBG sensors fail at 465 MPa of stress level which is below the global failure strength of specimen. The corresponding thermal and strain maps for this moment did not show any anomaly corresponding to major failure inside the AG laminate, therefore it implies that fiber optics have broken independent from material behavior. The axial strain map of Fig. 3-11a, does not show any high strain gradient regions prior to failure stress. On the contrary, transverse strain map reveals high strain gradients at left edge of the specimen as seen in Fig. 3-11b which later on results in sudden failure of sample as shown in Fig. 3-11c. Unlike AC laminate, damage accumulation inside nonhybrid AG sample appears to be very different at various regions of gauge length which results in different slopes of stress strain curves and even recording early failure points for some of the methods as compared to other strain measurement techniques. Variation of damage accumulation inside composite laminates can be analyzed through monitoring evolution of Poisson's ratio as a damage indicator index[98].



Fig. 3-10. Transfer of zone of interlaminar crack between carbon and glass plies in to the middle carbon layers as seen in 3C laminate

$\varepsilon_{yy}$ (με)   $\varepsilon_{xx}$ (με)   Temperature (°C)

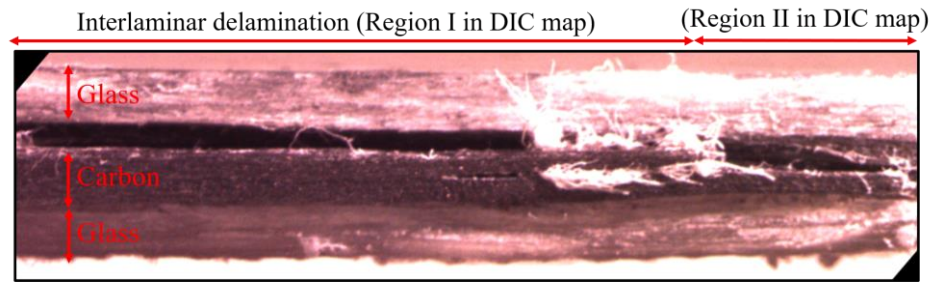(a) 617 MPa   (b) 617 MPa   (c) 618 MPa
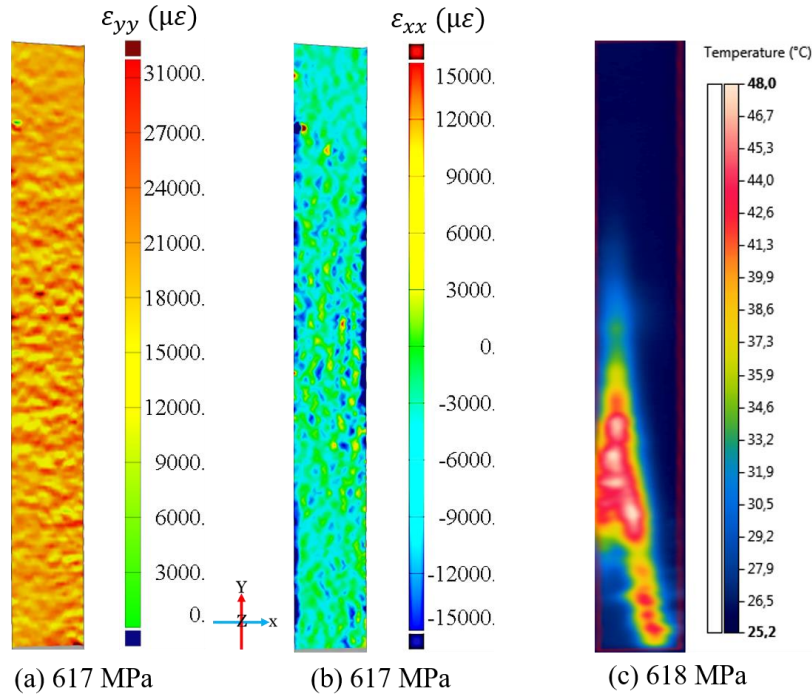
Fig. 3-11. (a)Axial strain map at 617 MPa, (b) Transverse strain map at 617 MPa, and (c) Thermal map at 618Mpa, for AG specimen

### 3.3.3   Resolve noise at early staged of full filed measurement by SEA method

The stress-strain curves at very low stress levels are shown for AG and 2C specimens in Fig. 3-12a and Fig. 3-12b. It is seen that all experimental strain measurement methods namely, FBGs and strain gauges show a clear slope and trend in data from the beginning while average strain values obtained from DIC present fluctuation in the collected data. Monitoring the full field strain maps for longitudinal strain throughout these stages reveals that these variations are related to sudden appearance of high strain gradient points on the surface. For example, at 5$^{th}$ second of tensile loading there appears a high strain gradient point at top left portion of AG laminates as seen in Fig. 3-12c. This anomaly creates an error in measured average strain by DIC and results in a jump at stress-strain curve, as if the strain values remain constant for a certain period of time despite the increase in applied stress, as presented in Fig. 3-12a.  As seen in Fig. 3-12e, similar source of error is seen for 2C sample, where several high strain gradient regions appear at the surface of gauge length. As a consequent, the stress-strain curve for 2C sample in Fig. 3-12b shows a constant strain period at the beginning of the loading stages unlike other strain measurement techniques. Implementation of SEA on strain values obtained through DIC results in consistency between full field strain values and locally collected ones through

109

FBGs and strain gauges as seen in Fig. 3-12a and Fig. 3-12b for AG and 2C specimens, respectively. The smoothing procedure results in a continuous strain map as seen in Fig. 3-12d and Fig. 3-12f and provides a realistic presentation of the strain map throughout the gauge length of specimens.
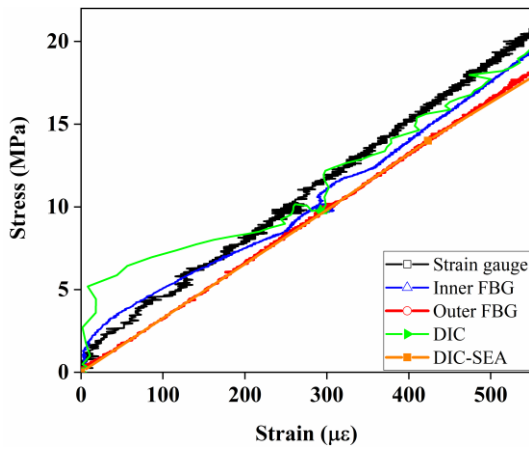


(a) AG
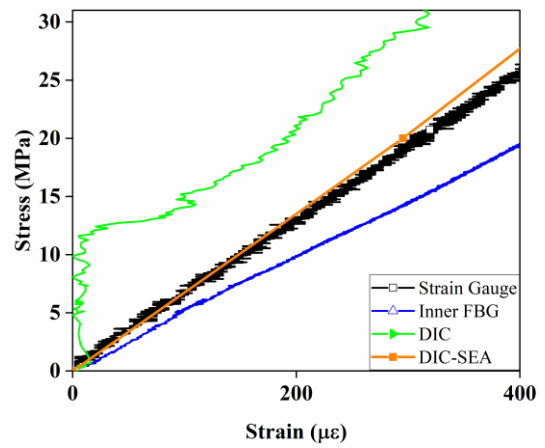
(b) 2C
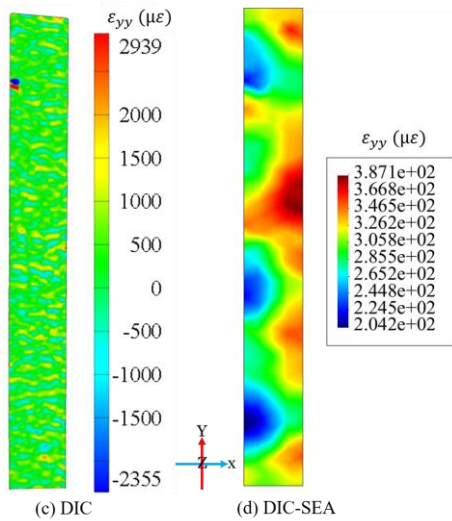


(c) DIC

(d) DIC-SEA
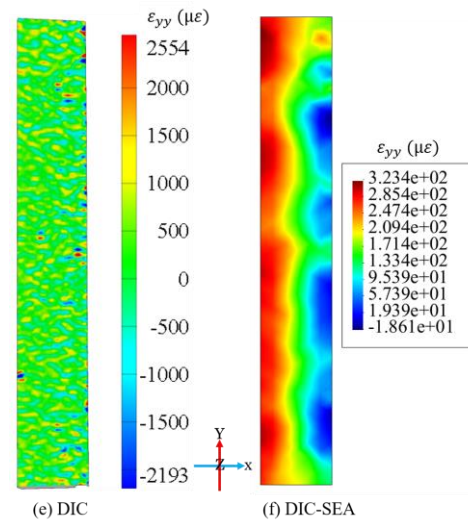
(e) DIC

(f) DIC-SEA

Fig. 3-12. Presence of data fluctuation at early stages of loading for (a) AG and (b) 2C samples; Full field longitudinal strain maps for AG sample obtained by (c) DIC and (d) DIC-SEA; Full field longitudinal strain maps for 2C sample obtained by (e) DIC and (f) DIC-SEA.

110

### 3.3.4    SEA-DIC approach as a tool for damage analysis

Fig. 3-13a shows the longitudinal strain map obtained by DIC for AG laminate immediately after the moment of failure. Presence of heterogenous strain map beyond the damage zone implies that the material is still under stress due to pressure exerted by grips, however due to deterioration of the speckle pattern and partial failure at lower half of the sample, DIC system is unable to capture the strain values at failure region. As seen in Fig. 3-13b, usage of SEA to extrapolate the DIC strain data in damage zone reveals that strains as high as 12390 $\mu\varepsilon$ can be experienced at this damaged region only due to the pressure exerted by the grip of testing machine. Therefore, it is possible for damages to develop further after failure due to mechanical pressure exerted from Tabbed region.

Fig. 3-13c shows the strain distribution for 3C specimen at stress level of 805MPa which is about 10% below the strength of this laminate. The longitudinal strain map throughout the gauge length is heterogeneous and it is not possible to certainly allocate possible failure points at higher stress levels. Despite that fact that no sign of damage development is observed either through other strain measurement techniques or thermal maps at 805 MPa. As seen in Fig. 3-13d implementation of SEA to obtain a continuous strain map reveals that high strain region has already appeared at lower right edge of the sample. As already shown in Fig. 3-10 this area develops as delamination at 866 MPa and causes final failure of the laminate. Thus, it is evident that smoothing of experimentally measured DIC results can reveal regions of the structure with high susceptibility for damage development and provide certain predictability for damage zones. A similar approach is taken for 13C sample at 982MPa which is 30% below the strength of this material, as seen in Fig. 3-13e and Fig. 3-13f. Presence of a high strain region at top left region of the gauge length shows the susceptibility of failure at that region as later on it is confirmed at 1366 MPa.
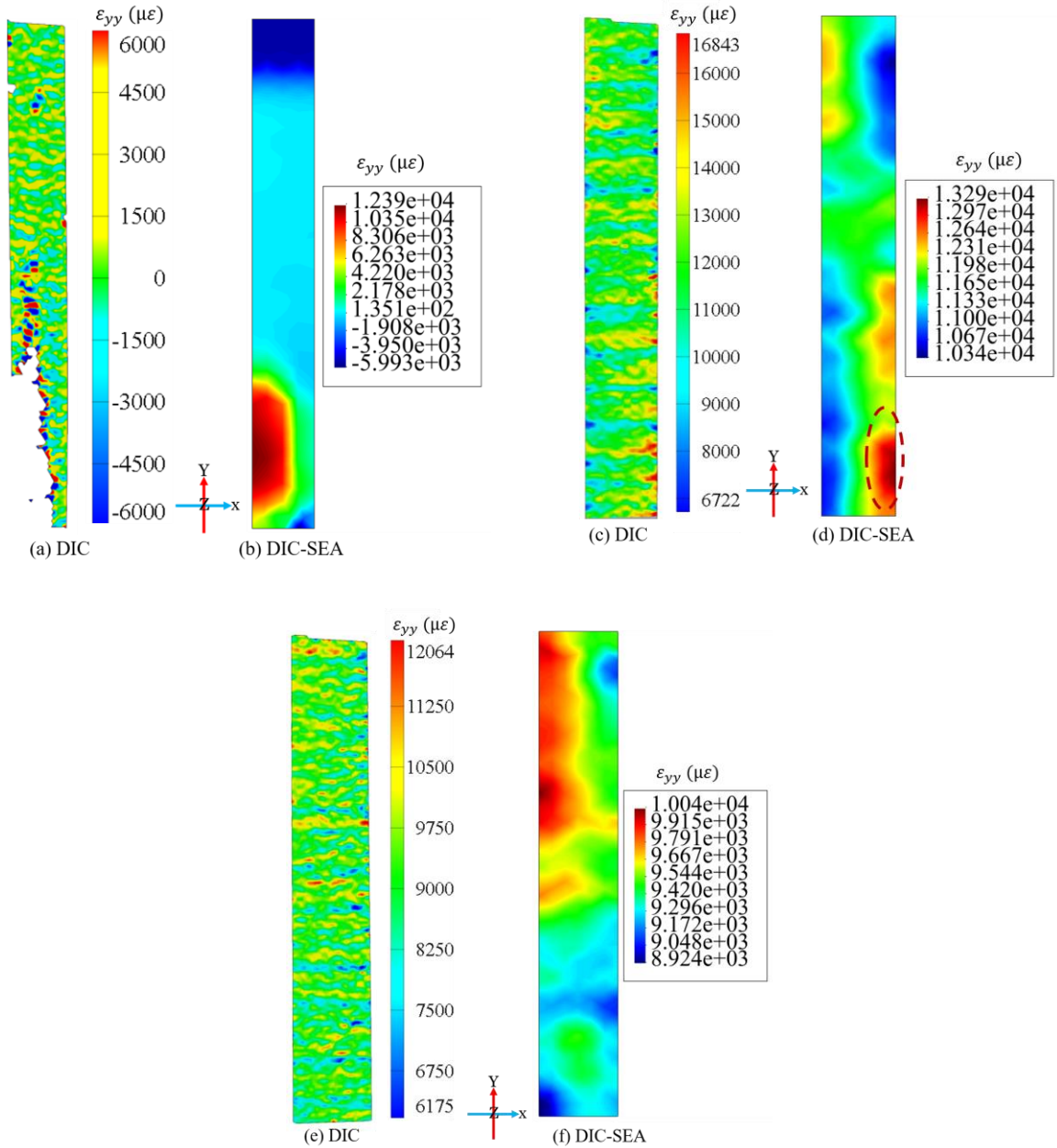
Fig. 3-13 Longitudinal strain maps obtained from DIC and DIC-SEA for a & b)AG; c & d)3C; e & f)13C laminates

### 3.3.5    Poisson Ratio as a Failure Development Indicator

Poisson's ratio evolution has been plotted against axial strain for each specimen as shown in Fig. 3-14. Herein, Poisson's ratio is obtained through two different strain measurement methods, namely, DIC and strain gauge, and the corresponding results are compared. As seen

in Fig. 3-14a to Fig. 3-14f, Poisson's ratio decreases due to accumulation of damage in composite laminate throughout the test. Therefore the rate of decrease in Poisson's ratio is in direct relationship with pace of the development of damages such as transverse matrix cracks in the laminate [137], and slope of plots in in Fig. 3-14 will provide a notion about the rate of failure progress. DIC and strain gauges give biaxial strain measurements from opposite surfaces of the laminate, thus the difference in the evolution of Poisson's ratio at two sides of the sample will reveal whether the damage progress is identically noted. To calculate the slope of plots in in Fig. 3-14, a simple linear regression is performed for all samples between 3000-8000 με, which corresponds to apparent starting point of stable evolution of Poisson's ratio up to first major failure in AC laminate. The slope values of fitting lines are presented in Table 3-3, where results based on strain gauge imply sharper damage development as compared to DIC counterparts. The distinction in variation of Poisson's ratio based on strain gauges and DIC can be attributed to strain measurement scale, i.e. global measurement through DIC and local measurement by strain gauge. In other words, since full field measurement are non-contact and global techniques, they are not influenced significantly by local changes of transverse cracks within the laminate and provide average of strain within the gauge length. On the other hand, surface mounted biaxial strain gauges are directly affected by damage incidents inside the material due to their contact interface. In order to further substantiate this conclusion, the evolution of transverse strains for two representative specimens, AC and 3C has been depicted in Fig. 3-11g and Fig. 3-11h. The values of axial strains measured through DIC and strain gauges were very close for each of these samples, however variation of transverse strains reveal that strain gauges have recorded more reduction as compared to DIC. This observation indicates that DIC measurement is less sensitive to transverse cracks due to its non-contact measurement nature. Thus, one can conclude that using surface mounted strain gauges to assess damage evolution inside the laminate is more meticulous.

(a) AC

(b) 13C

(c) 1C

(d) 2C

(e) 3C

(f) AG

(g) AC           (h)3C
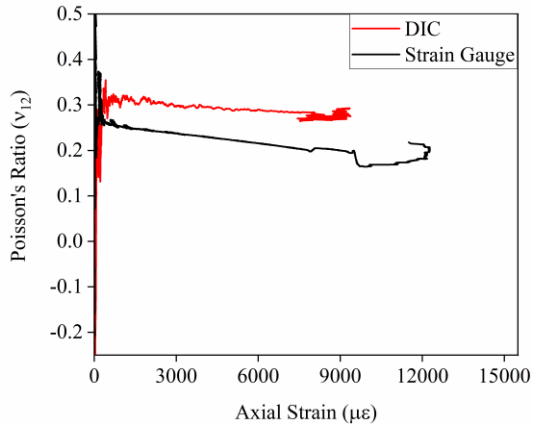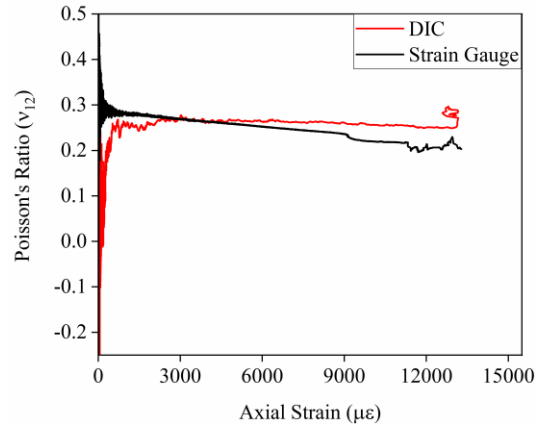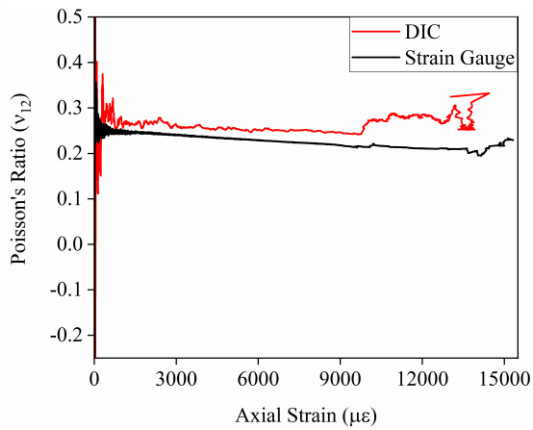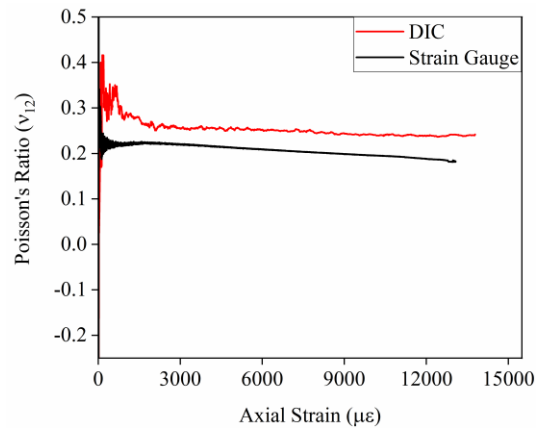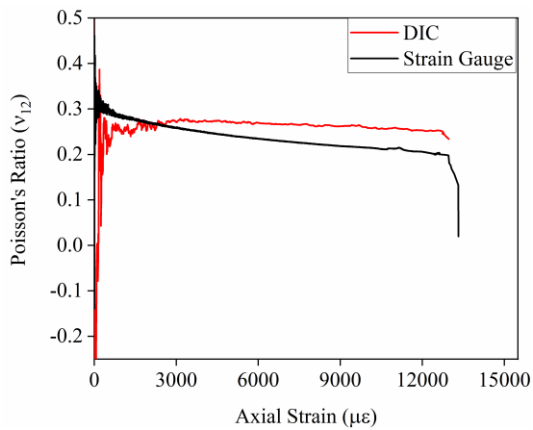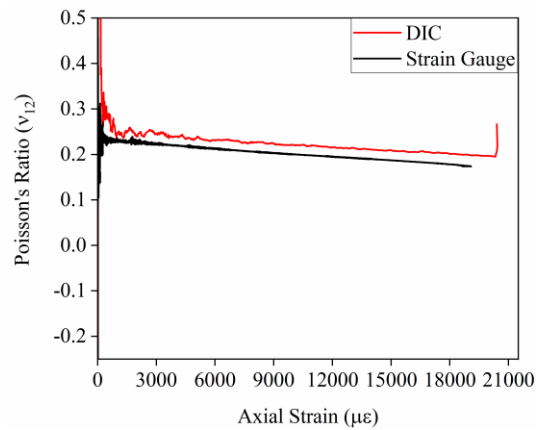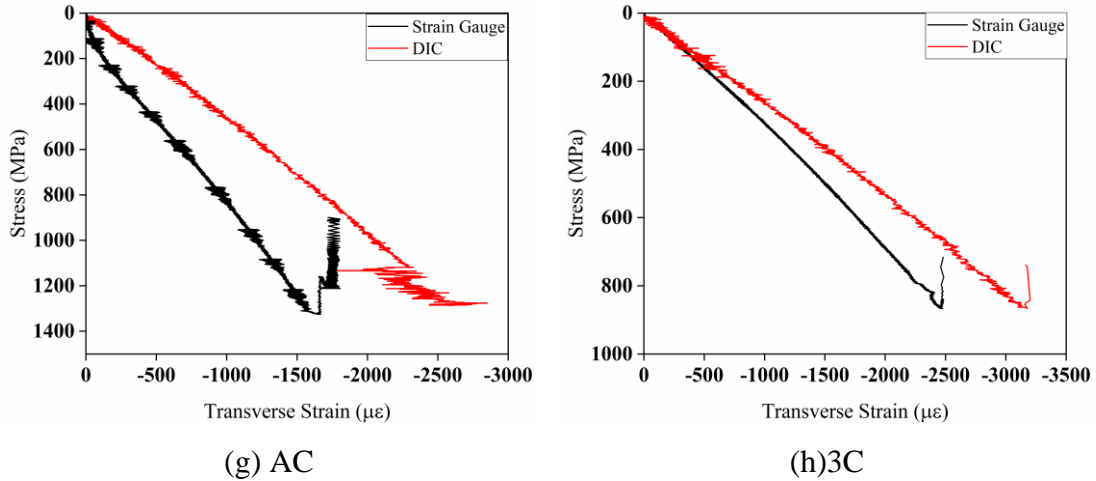
Fig. 3-14.  Poisson's ratio evolution vs axial strain for (a) AC, (b) 13C, (c) 1C, (d)2C, (e) 3C and (f) AG, laminates; Transverse strain reduction during tests for (g) AC and (h) 3C specimens.

Table 3-3. Poisson's Ratio Decrease Rate

| Specimen | AC | 13C | 1C | 2C | 3C | AG |
|---|---|---|---|---|---|---|
| $\vartheta_{12}$ Decrease Rate ($\mu\varepsilon^{-1}$) -DIC | -3.92 | -1.08 | -1.89 | -1.65 | -2.15 | -3.75 |
| $\vartheta_{12}$ Decrease Rate ($\mu\varepsilon^{-1}$) -Strain Gauges | -7.53 | -5.44 | -3.74 | -3.66 | -6.99 | -3.49 |

3.4 Conclusion

In this study the failure progress of nonhybrid and fiber hybrid laminates under tensile loading condition were monitored simultaneously by two embedded FGB sensors, DIC and strain gauges. Using local and global strain measurement techniques revealed that the obtained failure strains of a laminate might vary significantly based on the measurement technique, therefore RSD values were calculated for each laminate to show the statistical scatter in the failure strain respectively and enable comparison of data among the laminates. The comparison indicated that non-hybrid laminates namely AC and AG had the lowest and highest scatter in

115

data, while hybrid samples showed RSD levels in between the nonhybrid specimens. Comparison of failure strain results among hybrid samples with similar fiber volume fractions, namely, 1C, 2C, 3C, revealed that RSD values for these samples was close and change in stacking sequence did not make significant variation in failure strain values measured using different techniques. On the other hand, the RSD value for 13C laminate was highest among the hybrid laminates. Thereby it was suggested that using higher fraction of carbon fibers as compared to glass fibers in hybrid laminates promoted uncertainties in strain measurements and therefore miscalculation of hybrid effect value. Consequently, three different approaches were utilized to calculate hybrid effect and correlated with strain and thermal maps obtained through DIC and thermal maps during failure progress. Such a multi-instrument approach revealed that the variation of hybrid effect was correlated with damage size and its location. In other words, comparison of full field strain and thermal maps at various location of stress-strain curve for each laminate showed that some major failure events seen through global strain measurement techniques or thermal maps do not influence local strain measurement methods. Hence deviation in the slope of stress-strain curves occurs and consequently results in differentiation of hybrid effect values.

Implementation of SEA to obtain continuous strain maps from collected displacement data of DIC helped to reduce the noise at low stress levels and provided a reliable strain variation which was comparable to other strain measurement methods. Therefore, the inherent errors seen at low deformations was mitigated effectively. The other successful achievement through utilization of SEA was early detection of damage susceptible regions under tensile loading condition, as compared to untreated DIC strain and infrared thermal maps. Usage of SEA to reconstruct strain maps enabled detection of failure prone region at stress levels up to 30% below the actual failure strength of laminate. Monitoring Poisson's ratio throughout the test period for all laminates indicated that revealed that stiffness reduction as a consequence of damage accumulation inside the material is seen more effectively through biaxial strain gauge as compared to DIC. It is suggested that higher sensitivity of strain gauge can be related to its contact with material which affects it performance.

**Part III**

# Conclusions

In this study the mechanical response and damage accumulation in glass/carbon fiber hybrid laminates is analyzed in three different sections. The results of these conducted investigations can be summarized as follows:

(i)     Usage of acoustic emission for damage analysis of hybrid fiber laminates and comparing experimental and numerical results.

In this part a combination of numerical and experimental approach is used to correlate damage accumulation under flexural and tensile loading conditions with acoustic emission hits. The acoustic emission hits collected through piezoelectric sensors are clustered based on weighted peak frequency and partial power1 parameters using Kmeans algorithm. Four clusters are correlated with four failure types, namely, matrix cracking, interface failure, fiber pull out and fiber breakage at 50-160 kHz, 150-300 kHz, 300-400 kHz and 400-600 kHz of weighted peak frequency ranges, respectively. The flexural test results indicate stacking sequence can affect the hybrid effect in hybrid fiber laminates. Microscopic analysis reveals that crack growth rate under flexural load is reduced by initiation of interlaminar delamination between glass and carbon plies. Stepwise flexural behavior seen for hybrid fiber laminates with carbon plies at surface and glass plies beneath them is related to transfer of load from surface carbon plies to middle glass plies. Remarkably, it is shown that despite transfer of load after breakage of carbon plies to glass layers, the overall hybrid effect is controlled  by stacking sequence rather than volume fraction ratio of carbon to glass fibers. Successful correlation between RZT-FEM analysis and experimental data is obtained at elastic region for tensile and flexural samples. The deviation of numerical model from experimental results is corresponding to initiation of damages as per data of acoustic emission. The results of RZT analysis reveal that transverse-shear stresses increase tendency for delamination as a strain energy release path for the system and prevent successful load transfer to glass layer after breakage of carbon plies.

(ii)     Full field analysis of in-plane shear behavior of hybrid fiber laminates.

Three different sizes ROIs  are selected for DIC analysis and corresponding strain evolution throughout the v-notch shear test are compared with those of strain gauge. The results show that usage of large ROIs at the beginning of the test can cause miscalculation of average strain

values. This behavior is attributed to inclusion of regions with very low shear strain values which has not been affected by shear loading at the initial stages of the test. DIC measurements show that strain maps observed during in-plane shear test of hybrid fiber laminates with 90$^o$ fiber direction were dependent on the relative volume fraction of fibers rather than the stacking sequence of the glass and carbon layers. On the contrary stacking sequence of interply hybrid fiber laminates had a significant effect on resultant strain observed in notched region of tested samples.

(iii)     Multi-instrument approach to find uncertainties in hybrid effect and compare failure strains.

The tensile behavior of hybrid and nonhybrid samples are compared using various strain measurement techniques namely, DIC, Embedded FBG and strain gauges.  The tests are also accompanied by passive thermography approach to better understand the failure progress are different stress levels. Statistical comparison of failure strain through RSD calculation revealed that presence of higher volume fraction of carbon plies in hybrid laminates resulted in higher disparity in obtained failure strains. Comparison of hybrid effect values for each laminate obtained through various strain measurement techniques reveals that ability of full field monitoring techniques can prevent miscalculations in hybrid effect value. Hence it is shown experimentally that utilization of multi-instrument approach prevents mistakes associated with major damage initiation inside laminates structures. Utilizing SEA approach is introduced as a viable method for removal of inherent noise associated with DIC measurements at small deformations and it is shown that DIC-SEA can be used to predict the failure region inside laminates even before identification of damage susceptible regions through full field displacement measurements. The Poisson's ration evolution is calculated both for hybrid and nonhybrid samples using DIC and biaxial strain gauges. It is revealed that DIC indicates a slower damage accumulation inside the material due to their non-contact measurement approach.

# References

1.  Monfared Zanjani, J.S., et al., Repeated self-healing of nano and micro scale cracks in epoxy based composites by tri-axial electrospun fibers including different healing agents. RSC Advances, 2015. **5**(89): p. 73133-73145.

2.  Tabrizi, I.E., et al., Experimental and numerical investigation on fracture behavior of glass/carbon fiber hybrid composites using acoustic emission method and refined zigzag theory. Composite Structures, 2019.

3.  Wisnom, M.R., et al., Hybrid effects in thin ply carbon/glass unidirectional laminates: Accurate experimental determination and prediction. Composites Part A: Applied Science and Manufacturing, 2016. **88**: p. 131-139.

4.  Swolfs, Y., L. Gorbatikh, and I. Verpoest, Fibre hybridisation in polymer composites: A review. Composites Part a-Applied Science and Manufacturing, 2014. **67**: p. 181-200.

5.  Beylergil, B., et al., Experimental failure analysis and mechanical performance evaluation of fiber-metal sandwich laminates interleaved with polyamide-6,6 interlayers through the combined usage of acoustic emission, thermography and microscopy techniques. Journal of Sandwich Structures & Materials. **0**(0): p. 1099636220924654.

6.  Romhány, G., et al., Fracture behavior and damage development in self-reinforced PET composites assessed by located acoustic emission and thermography: Effects of flame retardant and recycled PET. Composites Science and Technology, 2016. **132**: p. 76-83.

7.  Flament, C., et al., Local strain and damage measurements on a composite with digital image correlation and acoustic emission. Journal of Composite Materials, 2016. **50**(14): p. 1989-1996.

8.  Nag-Chowdhury, S., et al., Crossed investigation of damage in composites with embedded quantum resistive strain sensors (sQRS), acoustic emission (AE) and digital image correlation (DIC). Composites Science and Technology, 2018. **160**: p. 79-85.

9.  Ali, H.Q., et al., Experimental study on dynamic behavior of woven carbon fabric laminates using in-house piezoelectric sensors. Smart Materials and Structures, 2019. **28**(10).

10. Tabrizi, I.E., et al., Determining tab material for tensile test of CFRP laminates with combined usage of digital image correlation and acoustic emission techniques. Composites Part A: Applied Science and Manufacturing, 2019. **127**: p. 105623.

11.    Khan, R.M.A., et al., Investigation on interlaminar delamination tendency of multidirectional carbon fiber composites. Polymer Testing, 2020. **90**: p. 106653.

12.    AlKhateab, B., et al., Damage mechanisms in CFRP/HNT laminates under flexural and in-plane shear loadings using experimental and numerical methods. Composites Part A: Applied Science and Manufacturing, 2020. **136**: p. 105962.

13.    Kocaman, E.S., et al., Monitoring the Damage State of Fiber Reinforced Composites Using an FBG Network for Failure Prediction. Materials, 2017. **10**(1): p. 32.

14.    Ali, H.Q., et al., Microscopic analysis of failure in woven carbon fabric laminates coupled with digital image correlation and acoustic emission. Composite Structures, 2019. **230**: p. 111515.

15.    Mandal, S.K.Z., Jamal. S. M; Yildiz, M, Damage detection in honeycomb sandwich panels by active thermography, in ICCM 2019. 2019, Engineers Australia: Melbourne- Australia.

16.    Zalameda, J. and W. Winfree, Detection and Characterization of Damage in Quasi-Static Loaded Composite Structures using Passive Thermography. Sensors (Basel, Switzerland), 2018. **18**(10): p. 3562.

17.    Hayashi, T. On the improvement of mechanical properties of composites by hybrid composition. in Proc. 8th Intl. Reinforced Plastics Conf. 1972.

18.    Kretsis, G., A Review of the Tensile, Compressive, Flexural and Shear Properties of Hybrid Fiber-Reinforced Plastics. Composites, 1987. **18**(1): p. 13-23.

19.    Fukuda, H., An Advanced Theory of the Strength of Hybrid Composites. Journal of Materials Science, 1984. **19**(3): p. 974-982.

20.    Fukunaga, H., T.-W. Chou, and H. Fukuda, Strength of Intermingled Hybrid Composites. Journal of Reinforced Plastics and Composites, 1984. **3**(2): p. 145-160.

21.    Zweben, C., Tensile strength of hybrid composites. Journal of Materials Science, 1977. **12**(7): p. 1325-1337.

22.    Swolfs, Y., et al., The effect of fibre dispersion on initial failure strain and cluster development in unidirectional carbon/glass hybrid composites. Composites Part A: Applied Science and Manufacturing, 2015. **69**: p. 279-287.

23.    Petrucci, R., et al., Mechanical characterisation of hybrid composite laminates based on basalt fibres in combination with flax, hemp and glass fibres manufactured by vacuum infusion. Materials & Design, 2013. **49**: p. 728-735.

24.     Dong, C.S. and I.J. Davies, Flexural and tensile moduli of unidirectional hybrid epoxy composites reinforced by S-2 glass and T700S carbon fibres. Materials & Design, 2014. **54**: p. 893-899.

25.     Giancaspro, J.W., C.G. Papakonstantinou, and P.N. Balaguru, Flexural Response of Inorganic Hybrid Composites With E-Glass and Carbon Fibers. Journal of Engineering Materials and Technology-Transactions of the Asme, 2010. **132**(2).

26.     Baker, C., et al., Transverse Cracking in Carbon Fiber Reinforced Polymer Composites: Modal Acoustic Emission and Peak Frequency Analysis. Composites Science and Technology, 2015. **116**.

27.     Sause, M.G.R., S. Schmitt, and S. Kalafat, Failure load prediction for fiber-reinforced composites based on acoustic emission. Composites Science and Technology, 2018. **164**: p. 24-33.

28.     Aggelis, A.S.P.a.D.G., Damage Assessment in Fibrous Composites Using Acoustic Emission, in Acoustic Emission, W. Sikorski, Editor. 2012, InTech. p. 279-294.

29.     Dahmene, F., S. Yaacoubi, and M.E. Mountassir, Acoustic Emission of Composites Structures: Story, Success, and Challenges. Physics Procedia, 2015. **70**: p. 599-603.

30.     Sause, M.G.R., et al., Pattern recognition approach to identify natural clusters of acoustic emission signals. Pattern Recognition Letters, 2012. **33**(1): p. 17-23.

31.     Yilmaz, C. and M. Yildiz, A study on correlating reduction in Poisson's ratio with transverse crack and delamination through acoustic emission signals. Polymer Testing, 2017. **63**: p. 47-53.

32.     Fotouhi, M. and M.A. Najafabadi, Acoustic emission-based study to characterize the initiation of delamination in composite materials. Journal of Thermoplastic Composite Materials, 2016. **29**(4): p. 519-537.

33.     Gutkin, R., et al., On acoustic emission for failure investigation in CFRP: Pattern recognition and peak frequency analyses. Mechanical Systems and Signal Processing, 2011. **25**(4): p. 1393-1407.

34.     Yilmaz, C., et al., A hybrid damage assessment for E-and S-glass reinforced laminated composite structures under in-plane shear loading. Composite Structures, 2018. **186**: p. 347-354.

35. Kempf, M., O. Skrabala, and V. Altstadt, Acoustic emission analysis for characterisation of damage mechanisms in fibre reinforced thermosetting polyurethane and epoxy (Reprinted from Composites Part B, vol 56, pg 477). Composites Part B-Engineering, 2014. **65**: p. 117-123.

36. Saidane, E.H., et al., Damage mechanisms assessment of hybrid flax-glass fibre composites using acoustic emission. Composite Structures, 2017. **174**: p. 1-11.

37. Fotouhi, M., et al., Detection of fibre fracture and ply fragmentation in thin-ply UD carbon/glass hybrid laminates using acoustic emission. Composites Part A: Applied Science and Manufacturing, 2016. **86**: p. 66-76.

38. Alfano, G. and M.A. Crisfield, Finite element interface models for the delamination analysis of laminated composites: mechanical and computational issues. International Journal for Numerical Methods in Engineering, 2001. **50**(7): p. 1701-1736.

39. Tessler, A., M. Di Sciuva, and M. Gherlone, A Refined Zigzag Beam Theory for Composite and Sandwich Beams. Journal of Composite Materials, 2009. **43**(9): p. 1051-1081.

40. Tessler, A., M. Di Sciuva, and M. Gherlone, A consistent refinement of first-order shear deformation theory for laminated composite and sandwich plates using improved zigzag kinematics. Journal of Mechanics of Materials and Structures, 2010. **5**: p. 341-367.

41. Averill, R.C., Static and dynamic response of moderately thick laminated beams with damage. Composites Engineering, 1994. **4**(4): p. 381-395.

42. Di Sciuva, M., Development of an anisotropic, multilayered, shear-deformable rectangular plate element. Computers & Structures, 1985. **21**(4): p. 789-796.

43. Murakami, H., Laminated Composite Plate Theory With Improved In-Plane Responses. Journal of Applied Mechanics, 1986. **53**(3): p. 661-666.

44. Di Sciuva, M. A refinement of the transverse shear deformation theory for multilayered orthotropic plates. . 1983. also in L'aerotecnica missili e spazio; 1984.

45. Tessler, A., M. Di Sciuva, and M. Gherlone, A homogeneous limit methodology and refinements of computationally efficient zigzag theory for homogeneous, laminated composite, and sandwich plates. Numerical Methods for Partial Differential Equations, 2011. **27**(1): p. 208-229.

46. Barut, A., E. Madenci, and A. Tessler, C0-continuous triangular plate element for laminated composite and sandwich plates using the {2,2} – Refined Zigzag Theory. Composite Structures, 2013. **106**: p. 835-853.

47. Gherlone, M., A. Tessler, and M. Di Sciuva, C 0 beam elements based on the Refined Zigzag Theory for multilayered composite and sandwich laminates. Composite Structures 2011. **93**.

48. Iurlaro, L., et al., Refined Zigzag Theory for laminated composite and sandwich plates derived from Reissner's Mixed Variational Theorem. Composite Structures, 2015.

49. Tessler, A., Refined zigzag theory for homogeneous, laminated composite, and sandwich beams derived from Reissner's mixed variational principle. Meccanica, 2015. **50**(10): p. 2621-2648.

50. Wimmer, H. and M. Gherlone, Explicit matrices for a composite beam-column with refined zigzag kinematics. Acta Mechanica, 2017. **228**(6): p. 2107-2117.

51. Wimmer, H. and K. Nachbagauer, Exact transfer- and stiffness matrix for the composite beam-column with Refined Zigzag kinematics. Composite Structures, 2018. **189**: p. 700-706.

52. Di Sciuva, M., et al., A class of higher-order C0 composite and sandwich beam elements based on the Refined Zigzag Theory. Composite Structures, 2015. **132**: p. 784-803.

53. Eijo, A., E. Oñate, and S. Oller, A four-noded quadrilateral element for composite laminated plates/shells using the refined zigzag theory. International Journal for Numerical Methods in Engineering, 2013. **95**(8): p. 631-660.

54. Hasim, K.A., Isogeometric static analysis of laminated composite plane beams by using refined zigzag theory. Composite Structures, 2018. **186**: p. 365-374.

55. Iurlaro, L., M. Gherlone, and M. Di Sciuva, The (3,2)-Mixed Refined Zigzag Theory for generally laminated beams: Theoretical development and C0 finite element formulation. International Journal of Solids and Structures, 2015. **73-74**: p. 1-19.

56. Kefal, A., K.A. Hasim, and M. Yildiz, A novel isogeometric beam element based on mixed form of refined zigzag theory for thick sandwich and multilayered composite beams. Composites Part B Engineering, 2018. **167**: p. 100-121.

57. Versino, D., et al., C0 triangular elements based on the Refined Zigzag Theory for multilayer composite and sandwich plates. Composites Part B: Engineering, 2013. **44**: p. 218–230.

58. Iurlaro, L., et al., Assessment of the Refined Zigzag Theory for bending, vibration, and buckling of sandwich plates: A comparative study of different theories. Composite Structures, 2013. **106**: p. 777-792.

59. Treviso, A., D. Mundo, and M. Tournour, A C0-continuous RZT beam element for the damped response of laminated structures. Composite Structures, 2015. **131**: p. 987-994.

60. Iurlaro, L., et al., Free vibration analysis of sandwich beams using the Refined Zigzag Theory: an experimental assessment. Meccanica, 2015.

61. Iurlaro, L., et al., Experimental assessment of the Refined Zigzag Theory for the static bending analysis of sandwich beams. Journal of Sandwich Structures & Materials, 2018. **20**(1): p. 86-105.

62. Kefal, A., A. Tessler, and E. Oterkus, An enhanced inverse finite element method for displacement and stress monitoring of multilayered composite and sandwich structures. Composite Structures, 2017. **179**: p. 514-540.

63. Kefal, A., A. Tessler, and E. Oterkus, An Efficient Inverse Finite Element Method for Shape and Stress Sensing of Laminated Composite and Sandwich Plates and Shells. 2018.

64. Kefal, A. and M. Yildiz, Modeling of Sensor Placement Strategy for Shape Sensing and Structural Health Monitoring of a Wing-Shaped Sandwich Panel Using Inverse Finite Element Method. Sensors, 2017. **17**(12): p. 2775.

65. Zanjani, J.S.M., et al., Design and fabrication of multi-walled hollow nanofibers by triaxial electrospinning as reinforcing agents in nanocomposites. Journal of Reinforced Plastics and Composites, 2015. **34**(16): p. 1273-1286.

66. Sause, M.G.R., et al., Quantification of failure mechanisms in mode-I loading of fiber reinforced plastics utilizing acoustic emission analysis. Composites Science and Technology, 2012. **72**(2): p. 167-174.

67. Tessler, A. and S.B. Dong, On a hierarchy of conforming timoshenko beam elements. Computers & Structures, 1981. **14**(3): p. 335-344.

68. Hull, D. and T.W. Clyne, An Introduction to Composite Materials. 2 ed. Cambridge Solid State Science Series. 1996, Cambridge: Cambridge University Press.

69.     Dong, C.S. and I.J. Davies, Optimal design for the flexural behaviour of glass and carbon fibre reinforced polymer hybrid composites. Materials & Design, 2012. **37**: p. 450-457.

70.     Pinho, S.T., et al., On longitudinal compressive failure of carbon-fibre-reinforced polymer: from unidirectional to woven, and from virgin to recycled. Philosophical Transactions of the Royal Society a-Mathematical Physical and Engineering Sciences, 2012. **370**(1965): p. 1871-1895.

71.     Chellappa, V. and B.Z. Jang, Crack growth and fracture behavior of fabric reinforced polymer composites. Polymer Composites, 1996. **17**(3): p. 443-450.

72.     Seyyed Monfared Zanjani, J., A.S. Al-Nadhari, and M. Yildiz, Manufacturing of electroactive morphing carbon fiber/glass fiber/epoxy composite: Process and structural monitoring by FBG sensors. Thin-Walled Structures, 2018. **130**: p. 458-466.

73.     Czél G, E.J., Bond IP, Wisnom MR. Development and characterisation of pseudo-ductile hybrid carbon/glass–epoxy composites made of thin spread carbon tows. in European Conference on Composite Materials 15. 2012. Venice.

74.     Czél, G. and M.R. Wisnom, Demonstration of pseudo-ductility in high performance glass/epoxy composites by hybridisation with thin-ply carbon prepreg. Composites Part A: Applied Science and Manufacturing, 2013. **52**: p. 23-30.

75.     Hedgepeth, J.M., Stress Concentrations in Filamentary Structures. 1961. p. 36.

76.     Gherlone, M., On the Use of Zigzag Functions in Equivalent Single Layer Theories for Laminated Composite and Sandwich Beams: A Comparative Study and Some Observations on External Weak Layers. Vol. 80. 2013. 061004.

77.     Kanu, N.J., et al., Self-healing composites: A state-of-the-art review. Composites Part A: Applied Science and Manufacturing, 2019. **121**: p. 474-486.

78.     Liu, L., et al., Interfacial characterization, control and modification of carbon fiber reinforced polymer composites. Composites Science and Technology, 2015. **121**: p. 56-72.

79.     Quan, D., et al., Interlaminar fracture toughness of aerospace-grade carbon fibre reinforced plastics interleaved with thermoplastic veils. Composites Part A: Applied Science and Manufacturing, 2019: p. 105642.

80.     Seyyed Monfared Zanjani, J., et al., Tailoring viscoelastic response, self-heating and deicing properties of carbon-fiber reinforced epoxy composites by graphene modification. Composites Part A: Applied Science and Manufacturing, 2018. **106**: p. 1-10.

81. Zakaria, M.R., et al., Hybrid carbon fiber-carbon nanotubes reinforced polymer composites: A review. Composites Part B: Engineering, 2019. **176**: p. 107313.

82. Ahmad, F., N. Yuvaraj, and P.K. Bajpai, Effect of reinforcement architecture on the macroscopic mechanical properties of fiberous polymer composites: A review. Polymer Composites, 2020. **41**(6): p. 2518-2534.

83. Biswas, D. and C. Ray, Effect of hybridisation in laminated composites on the first ply failure behaviour: Experimental and numerical studies. International Journal of Mechanical Sciences, 2019. **161-162**: p. 105057.

84. Wang, T., et al., Influence of the hybrid ratio and stacking sequence on mechanical and damping properties of hybrid composites. Polymer Composites, 2019. **40**(6): p. 2368-2380.

85. Tabrizi, I.E., et al., Experimental and numerical investigation on fracture behavior of glass/carbon fiber hybrid composites using acoustic emission method and refined zigzag theory. Composite Structures, 2019. **223**: p. 110971.

86. Naito, K., H. Oguma, and C. Nagai, Temperature-dependent tensile properties of hybrid carbon/glass thermoplastic composite rods. Polymer Composites, 2020. **41**(10): p. 3985-3995.

87. Meng, Q. and Z. Wang, Modeling analysis of fiber hybridization in hybrid glass/carbon composites under high-velocity impact. Polymer Composites, 2017. **38**(11): p. 2536-2543.

88. Stojcevski, F., T. Hilditch, and L.C. Henderson, A modern account of Iosipescu testing. Composites Part A: Applied Science and Manufacturing, 2018. **107**: p. 545-554.

89. ASTM D5379 / D5379M-12, Standard Test Method for Shear Properties of Composite Materials by the V-Notched Beam Method. 2012, ASTM International: West Conshohocken, PA.

90. Bru, T., et al., Use of the Iosipescu test for the identification of shear damage evolution laws of an orthotropic composite. Composite Structures, 2017. **174**: p. 319-328.

91. Choi, J.-H., et al., Determination of the in-plane shear modulus of unidirectional carbon fiber-reinforced plastics using digital image correlation and finite-element analysis. Composite Structures, 2019. **229**: p. 111392.

92. Daiyan, H., et al., Shear Testing of Polypropylene Materials Analysed by Digital Image Correlation and Numerical Simulations. Experimental Mechanics, 2012. **52**(9): p. 1355-1369.

93.     Qin, L., et al., Full-field analysis of shear test on 3D orthogonal woven C/C composites. Composites Part A: Applied Science and Manufacturing, 2012. **43**(2): p. 310-316.

94.     Bandaru, A.K., et al., Influence of hybridization on in-plane shear properties of 2D & 3D thermoplastic composites reinforced with Kevlar/basalt fabrics. Polymer Testing, 2017. **61**: p. 396-403.

95.     Gu, Y., et al., Characterization of the interphase in carbon fiber/polymer composites using a nanoscale dynamic mechanical imaging technique. Carbon, 2010. **48**(11): p. 3229-3235.

96.     Caminero, M.A., et al., Damage monitoring and analysis of composite laminates with an open hole and adhesively bonded repairs using digital image correlation. Composites Part B: Engineering, 2013. **53**: p. 76-91.

97.     Zeng, Q.-D., L. Ling, and Z.-L. Wang, Statistical strength of unidirectional composites and the effect of the interfacial shear strength. Composites Science and Technology, 1996. **56**(10): p. 1191-1200.

98.     Akay, E., et al., Monitoring Poisson's Ratio Degradation of FRP Composites under Fatigue Loading Using Biaxially Embedded FBG Sensors. Materials, 2016. **9**(9): p. 781.

99.     Orell, O., et al., Characterization of elastic constants of anisotropic composites in compression using digital image correlation. Composite Structures, 2018. **185**: p. 176-185.

100.    Hill, K.O., et al., Photosensitivity in optical fiber waveguides: Application to reflection filter fabrication. Applied Physics Letters, 1978. **32**(10): p. 647-649.

101.    Botsis, J., et al., Embedded fiber Bragg grating sensor for internal strain measurements in polymeric materials. Optics and Lasers in Engineering, 2005. **43**(3-5): p. 491-510.

102.    Gebremichael, Y.M., et al., Integration and assessment of fibre Bragg grating sensors in an all-fibre reinforced polymer composite road bridge. Sensors and Actuators A: Physical, 2005. **118**(1): p. 78-85.

103.    Mulle, M., et al., Response of fiber Bragg gratings bonded on a glass/epoxy laminate subjected to static loadings. Composite Structures, 2015. **130**: p. 75-84.

104.    Yildiz, M., et al., An Experimental Study on the Process Monitoring of Resin Transfer Molded Composite Structures Using Fiber Optic Sensors. Journal of Manufacturing Science and Engineering, 2012. **134**(4): p. 044502-044502-6.

105.    Majumder, M., et al., Fibre Bragg gratings in structural health monitoring—Present status and applications. Sensors and Actuators A: Physical, 2008. **147**(1): p. 150-164.

106.    Mulle, M., et al., Assessment of cure residual strains through the thickness of carbon–epoxy laminates using FBGs, Part I: Elementary specimen. Composites Part A: Applied Science and Manufacturing, 2009. **40**(1): p. 94-104.

107.    Parlevliet, P.P., H.E.N. Bersee, and A. Beukers, Measurement of (post-)curing strain development with fibre Bragg gratings. Polymer Testing, 2010. **29**(3): p. 291-301.

108.    Ramezani-Dana, H., et al., Hygroscopic strain measurement by fibre Bragg gratings sensors in organic matrix composites – Application to monitoring of a composite structure. Composites Part B: Engineering, 2014. **58**: p. 76-82.

109.    Yan, C., et al., Development of flexible pressure sensing polymer foils based on embedded fibre Bragg grating sensors. Procedia Engineering, 2010. **5**: p. 272-275.

110.    Yilmaz, C., et al., Monitoring Poisson's ratio of glass fiber reinforced composites as damage index using biaxial Fiber Bragg Grating sensors. Polymer Testing, 2016. **53**: p. 98-107.

111.    Kuang, K.S.C., et al., Embedded fibre Bragg grating sensors in advanced composite materials. Composites Science and Technology, 2001. **61**(10): p. 1379-1387.

112.    Bosia, F., et al., Through-the-thickness distribution of strains in laminated composite plates subjected to bending. Composites Science and Technology, 2004. **64**(1): p. 71-82.

113.    Emmons, M.C., et al., Strain Measurement Validation of Embedded Fiber Bragg Gratings. International Journal of Optomechatronics, 2010. **4**(1): p. 22-33.

114.    Karen, W., et al., Fiber optic sensors for health monitoring of morphing airframes: I. Bragg grating strain and temperature sensor. Smart Materials and Structures, 2000. **9**(2): p. 163.

115.    Ubaid, J., M. Kashfuddoja, and M. Ramji, Strength prediction and progressive failure analysis of carbon fiber reinforced polymer laminate with multiple interacting holes involving three dimensional finite element analysis and digital image correlation. International Journal of Damage Mechanics, 2014. **23**(5): p. 609-635.

116.    Kashfuddoja, M., R.G.R. Prasath, and M. Ramji, Study on experimental characterization of carbon fiber reinforced polymer panel using digital image correlation: A sensitivity analysis. Optics and Lasers in Engineering, 2014. **62**: p. 17-30.

117.    Brunbauer, J. and G. Pinter, On the strain measurement and stiffness calculation of carbon fibre reinforced composites under quasi-static tensile and tension-tension fatigue loads. Polymer Testing, 2014. **40**: p. 256-264.

118. Hoffmann, J., H. Cui, and N. Petrinic, Determination of the strain-energy release rate of a composite laminate under high-rate tensile deformation in fibre direction. Composites Science and Technology, 2018. **164**: p. 110-119.

119. Oz, F.E., et al., Multi-instrument in-situ damage monitoring in quasi-isotropic CFRP laminates under tension. Composite Structures, 2018. **196**: p. 163-180.

120. Périé, J.N., et al., Digital image correlation and biaxial test on composite material for anisotropic damage law identification. International Journal of Solids and Structures, 2009. **46**(11): p. 2388-2396.

121. Liu, Y., et al., The mechanism of strain influence on interpolation induced systematic errors in digital image correlation method. Optics and Lasers in Engineering, 2019. **121**: p. 323-333.

122. Rossi, M., et al., Effect of DIC Spatial Resolution, Noise and Interpolation Error on Identification Results with the VFM. Strain, 2015. **51**(3): p. 206-222.

123. Zhu, H., et al., Influence of imaging configurations on the accuracy of digital image correlation measurement. Measurement Science and Technology, 2018. **29**(3): p. 035205.

124. Pan, B., et al., Displacement Smoothing and Strain Estimation Using Savitaky-Golay Filters in Digital Image Correlation. Key Engineering Materials, 2006. **326-328**: p. 135-138.

125. Yoneyama, S., Smoothing Measured Displacements and Computing Strains Utilising Finite Element Method. Strain, 2011. **47**(s2): p. 258-266.

126. Dai, X., et al., Strain field estimation based on digital image correlation and radial basis function. Optics and Lasers in Engineering, 2015. **65**: p. 64-72.

127. Li, X., et al., A practical and effective regularized polynomial smoothing (RPS) method for high-gradient strain field measurement in digital image correlation. Optics and Lasers in Engineering, 2019. **121**: p. 215-226.

128. Li, X., et al., Local Hermite (LH) Method: An accurate and robust smooth technique for high-gradient strain reconstruction in digital image correlation. Optics and Lasers in Engineering, 2019. **112**: p. 26-38.

129. Tessler, A., et al., An improved variational method for finite element stress recovery and a posteriori error estimation. Computer Methods in Applied Mechanics and Engineering, 1998. **155**(1): p. 15-30.

130. Kefal, A. and E. Oterkus, Displacement and stress monitoring of a chemical tanker based on inverse finite element method. Ocean Engineering, 2016. **112**: p. 33-46.

131. Kefal, A. and E. Oterkus, Displacement and stress monitoring of a Panamax containership using inverse finite element method. Ocean Engineering, 2016. **119**: p. 16-29.

132. Kefal, A., A. Tessler, and E. Oterkus, An Efficient Inverse Finite Element Method for Shape and Stress Sensing of Laminated Composite and Sandwich Plates and Shells. NASA/TP-2018-220079. 2018.

133. Kefal, A. and E. Oterkus, Structural health monitoring of marine structures by using inverse finite element method, in Analysis and Design of Marine Structures - Proceedings of the 5th International Conference on Marine Structures, MARSTRUCT 2015. 2015. p. 341-350.

134. Swolfs, Y., I. Verpoest, and L. Gorbatikh. Tensile failure of hybrid composites: Measuring, predicting and understanding. in IOP Conference Series: Materials Science and Engineering. 2016.

135. AlKhateab, B., et al., Damage mechanisms in CFRP/HNT laminates under flexural and in-plane shear loadings using experimental and numerical methods. Composites Part a-Applied Science and Manufacturing, 2020. **136**.

136. Surgeon, M., et al., Transverse cracking and Poisson's ratio reduction in cross-ply carbon fibre-reinforced polymers. Journal of Materials Science, 1999. **34**(22): p. 5513-5517.

137. Gao, F., et al., Damage accumulation in woven-fabric CFRP laminates under tensile loading: Part 1. Observations of damage accumulation. Composites Science and Technology, 1999. **59**: p. 123-136.

138. Smith, P.A. and J.R. Wood, Poisson's ratio as a damage parameter in the static tensile loading of simple crossply laminates. Composites Science and Technology, 1990. **38**(1): p. 85-93.

139. Van Paepegem, W., et al., Monitoring quasi-static and cyclic fatigue damage in fibre-reinforced plastics by Poisson's ratio evolution. International Journal of Fatigue, 2010. **32**(1): p. 184-196.

140. Tessler, A. and T.J.R. Hughes, A three-node mindlin plate element with improved transverse shear. Computer Methods in Applied Mechanics and Engineering, 1985. **50**(1): p. 71-101.

141.   Czél, G., et al., Design and characterisation of high performance, pseudo-ductile all-carbon/epoxy unidirectional hybrid composites. Composites Part B: Engineering, 2017. **111**: p. 348-356.

142.   Sapozhnikov, S.B., Y. Swolfs, and S.V. Lomov, Pseudo-ductile unidirectional high modulus/high strength carbon fibre hybrids using conventional ply thickness prepregs. Composites Part B: Engineering, 2020. **198**: p. 108213.

143.   Swolfs, Y., et al., Global load-sharing model for unidirectional hybrid fibre-reinforced composites. Journal of the Mechanics and Physics of Solids, 2015. **84**: p. 380-394.

144.   Pagano, F., et al., Numerical and experimental approach for improving quasi-static and fatigue testing of a unidirectional CFRP composite laminate. Procedia Engineering, 2018. **213**: p. 804-815.

145.   Ajovalasit, A. and G. Pitarresi, Strain Measurement on Composites: Effects due to Strain Gauge Misalignment. Strain, 2011. **47**: p. E84-E92.

## List of Publications and Presentations

1. Determining Tab Material for Tensile Test of CFRP Laminates with Combined Usage of Digital Image Correlation and Acoustic Emission Techniques
Composites Part A: Applied Science and Manufacturing, 2019
I. Emami Tabrizi, R.M. Awais Khan, E. Massarwa, J.S.M. Zanjani, H. Qasim Ali, E. Demir, M. Yildiz,

2. Experimental and Numerical Investigation on Fracture Behavior of Glass/Carbon Fiber Hybrid Composites Using Acoustic Emission Method and Refined Zigzag Theory,
Composite structures, 2019
I. Emami Tabrizi, A. Kefal, J.S.M. Zanjani, C. Akalin, M. Yildiz,

3. Experimental study On Dynamic Behavior of woven carbon fabric laminates using in-house piezoelectric sensors,
Smart materials and structures, 2019
H. Qasim Ali, I. Emami Tabrizi, R.M. Awais Khan, J.S.M. Zanjani, Cagatay Yilmaz, L.H. Poudeh, M. Yildiz,

4. Microscopic Analysis of Failure in Woven Carbon Fabric Laminates Coupled with Digital Image Correlation and Acoustic Emission,
Composite Structures, 2019
H. Qasim Ali, I. Emami Tabrizi, R.M. Awais Khan, A. Tufani, M. Yildiz,

5. Non-Destructive Determination of the Stiffness Matrix of a Laminated Composite Structure with Lamb Wave,
Composite Structures, 2020
C. Yilmaz, S. Topal, H. Qasim Ali, I. Emami Tabrizi, A. Suleman, M. Yildiz,

6. Thermo-Responsive and Shape-Morphing CF/GF Composite skin: Full-Field Experimental Measurement, Theoretical Prediction, and Finite Element Modelling
Thin Walled Structures, 2020
J.S.M Zanjani, P. Yousefi Louyeh, I. Emami Tabrizi; A.S. Al-Nadhari; M. Yildiz,

7. Mechanical properties and acoustic emission characteristics of fiber metal laminates with polyamide-6,6 (PA 66) nonwoven fabric interlayers,
Journal of Sandwich Structures and Materials, 2020
B. Beylergil, I. Emami Tabrizi, J.S.M Zanjani, S. Saeidiharzand; L.H. Poudeh; M. Yildiz,

8. Damage Mechanisms in CFRP/HNT Laminates Under Flexural and In-Plane Shear loadings Using Experimental and Numerical Methods
Composites Part A: Applied Science and Manufacturing, 2020
Baidaa AlKhateab, I. Emami Tabrizi, J.S.M Zanjani, M. N. Rahimi, L.H.Poudeh, A.Kefal, M.Yildiz,

9. Investigation on Interlaminar Delamination Tendency of Multidirectional Carbon Fiber Composites
   Polymer Testing, 2020
   R.M. Awais Khan; I. Emami Tabrizi; H. Qasim Ali, E. Demir, M.Yildiz,

10. Using DIC for In-situ Strain and Damage Monitoring in Hybrid Fiber Laminates Under In-plane Shear Loading
    Polymer Composites (Under Review 2021)
    I. Emami Tabrizi, B. Alkhateab, J.S.M Zanjani, M. Yildiz,

11. Damage Growth and Failure Detection in Hybrid Composites Using In-Situ Strain Measurements and Smoothing Element Analysis
    Composites Part A: Applied Science and Manufacturing, (Under Review 2021)
    I. Emami Tabrizi, A. Kefal, J.S.M. Zanjani, M. Yildiz

12. Development of Smoothed iFEM Approach for Shape Sensing Applications and its Experimental Validation on Composite Structures.
    Mechanical Systems and Signal processing, 2021
    A. Kefal, I. Emami Tabrizi, M.Yildiz, A. Tessler,

13. Numerical Prediction and Experimental Validation of the Mechanical Response and Failure Behavior of Glass/Carbon Fiber Hybrid Composites
    Composite Structures, (Under Review 2021)
    E. Massarwa, I. Emami Tabrizi, M. Yildiz,

14. Effect of Internal Feature on Microstructure and Mechanical Properties of Direct Metal Laser Sintering-Built Inconel 718.
    Additive Manufacturing, (Revision 2021)
    M. Isik, I. Emami Tabrizi, R.M. Awais Khan, E. Aydogan, M.Yildiz, B. Koç,

15. An Experimental implementation of Inverse Finite Element Method for Real-Time Shape and Strain Sensing of Composite and Sandwich Structures.
    Composite Structures, 2021
    A. Kefal, I. Emami Tabrizi, M. Tansan, E. Kisa, M.Yildiz,

16. Spatially Variable Identification of Thermoelastic Models in Composite Structures Using Full-Field Strain and Temperature Measurements
    NDT & E, (Prepared 2021)
    F.S´. Rodrigues, R. Marques, I. Emami Tabrizi, A. Kefal, H. Qasim Ali, M. Yildiz, A. Suleman,

CONFERENCES
1. Investigation of Damage Accumulation in Glass/Carbon Fiber Hybrid Composites through Acoustic Emission Method,
   International conference on composite materials (ICCM22), 2019, Melbourne-Australia.
   I. Emami Tabrizi, J.S.M Zanjani, Mehmet Yildiz,

2. Acoustic Emission Monitoring of Glass/Carbon Hybrid Fiber/Epoxy Composites Under Flexural and Tensile Loading Conditions,
5th International Conference on Mechanics of Composites (MECHCOMP), 2019, Lisbon-Portugal
I. Emami Tabrizi, J.S.M Zanjani, Cagdas Akalin, Mehmet Yildiz,